Universidade Federal
do Rio de Janeiro
Escola Politécnica

MANUFACTURING AND EFFICIENCY EVALUATION OF PEROVSKITE MULTI-CATION SOLAR CELLS (CsMAFA) WITH DIFFERENT ELECTRON TRANSPORT LAYERS

Lucas Galhardo Pimenta Tienne

Graduation Project presented to the Materials Engineering Course at Escola Politécnica, Federal University of Rio de Janeiro, as part of the requirements for obtaining the title of Engineer.

Advisor: Renata Antoun Simão

Co- Advisor: Ana Flávia Nogueira
Francineide Lopes de Araújo
Maria de Fátima Vieira Marques

Rio de Janeiro
August 2022

MANUFACTURING AND EFFICIENCY EVALUATION OF PEROVSKITE MULTI-CATION SOLAR CELLS (CsMAFA) WITH DIFFERENT ELECTRON TRANSPORT LAYERS

Lucas Galhardo Pimenta Tienne

GRADUATION PROJECT SUBMITTED TO THE FACULTY OF THE MATERIALS ENGINEERING COURSE OF THE POLYTECHNICAL SCHOOL OF THE FEDERAL UNIVERSITY OF RIO DE JANEIRO AS PART OF THE REQUIREMENTS NECESSARY TO OBTAIN THE DEGREE OF MATERIALS ENGINEER.

Examined by:

Renata Antoun Simão, D. Sc.
PEMM-COPPE/UFRJ

Maria de Fátima Vieira Marques, D. Sc.
IMA/UFRJ

Ana Flávia Nogueira, D. Sc.
IQ/UNICAMP

Francineide Lopes de Araújo, D. Sc.
IQ/UNICAMP

Adriana da Cunha Rocha, D. Sc.
PEMM-COPPE/UFRJ

Jilian Nei de Freitas, D. Sc.
CTI Renato Archer

RIO DE JANEIRO, RJ - BRASIL
AUGUST 2022

Tienne, Lucas Galhardo Pimenta

Manufacturing and efficiency evaluation of perovskite multi-cation solar cells (CsMAFA) with different electron transport layers/ Lucas Galhardo Pimenta Tienne – Rio de Janeiro:

UFRJ/ Escola Politécnica, 2012.

XV, 122 p.: il; 29,7 cm.

Orientadora: Renata Antoun Simão.

Coorientadora: Ana Flávia Nogueira, Francineide Lopes de Araújo e Maria de Fátima Vieira Marques.

Projeto de graduação – UFRJ/Escola Politécnica/ Curso de Engenharia de Materiais, 2022.

Referências Bibliográficas: p. 101-122.

1. Perovskite Solar Cells. 2. Electron Transport Layer. 3. Graphene. 4. Titanium Dioxide.I. Simão, Renata Antoun. II. Universidade Federal do Rio de Janeiro, Escola Politécnica, Curso de Engenharia de Materiais. III. Manufacturing and efficiency evaluation of perovskite multi-cation solar cells (CsMAFA) with different electron transport layers.

“The true sign of intelligence

is not knowledge but imagination."

Einstein, Albert.

Acknowledgments

First, I would like to thank God for supporting me even in moments when I did not realize it; I thank my parents, Odair and Valzilea, for believing in me and encouraging me on this journey. They always worked and fought for me to have a good education and be a good person. I thank my brothers, Luana and Gustavo, for all the support along my journey. To my nephews João Victor, Enzo, and Ana Clara for having the ability to make me happy with a simple smile. Ana Paula, Wellington, and my aunts, uncles, cousins, and grandparents, who were also essential for my maturation.

I thank my second parents that life gave me: Sandra, Paulo, Simone, and Leandro, who welcomed me into their lives. To my friends of all time, Mariana, Milu, Thiago, Júlia, and Luiza, who were with me day and night. To the entire Kale, Figueiró, and Gomes families, I have great affection for and consider them part of me. To all my friends from the Undergraduate Program in Nanotechnology and Materials Engineering who were not with me in subjects but also as support and motivation. Special thanks for the companionship of Marina Bernardes, Igor Guida, and Igor Candido throughout this journey.

I thank all my friends and colleagues from the Instituto de Macromolecules Professor Eloisa Mano, who were with me day after day, making the workplace always more cheerful and cozy. Thanks to Taihana, Vinicius, Bruno, Gustavo, Bárbara, Fernanda, Ludmila, Bruno Cancela, Douglas, Kelly, Flávio, Elen, Karen. Elisa, who was with me in several professional and personal challenges and was an incredible friend. Daniela for her companionship during the TCC work and incredible friendship. I thank my colleagues at LNES who welcomed me so well. I thank Bruno and JP for their friendship. I also especially thank Francineide and Deinha for their great friendship and for being day-to-day companions. I thank Samuel for the friendships made in Campinas, who proved to be an incredible person in such a short time.

I am immensely grateful to my advisor Renata who has always shown me that I can go further and always encouraged me. I am immensely grateful to the professor and my advisor Maria de Fátima for welcoming me since my first scientific internship and for all the teaching, trust, affection, opportunity, infrastructure, and encouragement. Ana Flávia, who made all her laboratories available and provided essential support for this project. Francineide, who taught me the basics of device manufacturing and always asked a lot. Without you, none of this would be possible. To all technicians, employees, and professors at UFRJ, IQ/UNICAMP, especially those at IMA, who always strive to improve the condition of education and science in Brazil. I would also like to thank the companies "Nacional de Grafite" and "MG Grafeno" for making their materials available. To CNPq, CAPES, FAPERJ, CINE, MCTI, and FAPERSP for financial support and infrastructure.

Resumo do Projeto de Graduação apresentado à Escola Politécnica/ UFRJ como parte dos requisitos necessários para obtenção do grau de Engenheira de Materiais.

FABRICAÇÃO E AVALIAÇÃO DE EFICIÊNCIA DE CÉLULAS SOLARES DE PEROVSKITA MULTI-CÁTION (CsMAFA) COM DIFERENTES CAMADAS DE TRANSPORTE DE ELÉTRONS

Lucas Galhardo Pimenta Tienne

Agosto/2022

Orientadora: Renata Antoun Simão.

Coorientadoras: Ana Flávia Nogueira, Francineide Lopes de Araújo e Maria de Fátima Vieira Marques.

Curso: Engenharia de Materiais

Células solares de perovskita têm tido grande destaque no cenário mundial para a produção de energia elétrica. Em dez anos esse dispositivo já atingiram eficiências de conversão de energia (PCE) maiores que 25%, similares aos das células de silício utilizadas atualmente no mercado. Entretanto, essa tecnologia apresenta problemas associados a estabilidade e reprodutibilidade. Os estudos recentes demonstram que as camadas adjacentes, responsáveis por extrair as cargas de maneira eficiente dos materiais de perovskita, ainda limitam o desempenho dessa tecnologia. Dessa forma, a camada transportadora de elétrons (ETL) é o foco de diversos estudos a fim de melhorar a sua performance para obter dispositivos de alta eficiência de conversão de energia. O presente trabalho realizou diferentes modificações na camada ETL baseada em SnO_2 em células solares de perovskita multi-cátion (CsMAFA) de alta performance. Foram fabricados e avaliados dispositivos fotovoltaicos sendo utilizado como camadas transportadores de elétrons variando os nanocompósitos de SnO_2 contendo diferentes tipos de grafeno ou dióxido de titânio em diversas concentrações. Também foi avaliado a influencia do precursor do dióxido de estanho para preparação dos filmes. Foi avaliada também a preparação da dupla camada de ETL como uma solução para melhorar a eficiência dos dispositivos por conta da inserção de nanoplaquetas de grafeno. Os resultados demonstraram que a inserção de grafeno de poucas camadas, óxido de grafeno e dióxido de titânio anatase geraram dispositivos solares de alta eficiência com maior densidade de corrente e efeito de histerese reduzido.

Palavras-chave: Células solares de perovskita, camada de transporte de elétrons Grafeno, dióxido de titânio.

Abstract of Undergraduate Project presented to POLI/UFRJ as a partial fulfillment of the requirements for the degree of Materials Engineer.

MANUFACTURING AND EFFICIENCY EVALUATION OF PEROVSKITE MULTI-CATION SOLAR CELLS (CsMAFA) WITH DIFFERENT ELECTRON TRANSPORT LAYERS

Lucas Galhardo Pimenta Tienne

Agosto/2022

Advisor: Renata Antoun Simão

Co-advisors: Ana Flávia Nogueira, Francineide Lopes de Araújo e Maria de Fátima Vieira Marques.

Course: Materials Engineering

Perovskite solar cells have been prominent on the world stage for electricity production. In ten years, they have reached energy conversion efficiencies (PCE) greater than 25%, higher than the silicon cells currently used on the market. However, this technology has problems associated with stability and reproducibility. The most promising studies show that such a barrier is mainly related to the limitation of the adjacent layers responsible for efficiently extracting the charges from the perovskite materials. Thus, several studies focus on the electron transport layer (ETL) to improve its performance to obtain devices with high energy conversion efficiency. The present work performed different modifications on the SnO_2-based ETL layer in high-performance multi-cation perovskite (CsMAFA) solar cells. Photovoltaic devices containing different types of graphene or titanium dioxide in different concentrations were manufactured and evaluated. And also was avalueted the influency of the tin dioxide precursor solutions on device performance. In addition, the preparation of the double layer of ETL was also evaluated as a solution to improve the efficiency of devices due to the insertion of graphene nanoplatelets. The results demonstrated that the insertion of thin-layer graphene, graphene oxide, and anatase titanium dioxide generated high-efficiency solar devices with higher current density and reduced hysteresis effect.

Keywords: Perovskite Solar Cells, Electron Transport Layer Graphene, Titanium Dioxide.

SUMMARY

LIST OF FIGURES

LIST OF TABLES

LIST OF ABBREVIATIONS

Institutions

COPPE – Instituto Alberto Luiz Coimbra de Pós-Graduação e Pesquisa em Engenharia;

CTI Renato Archer – Centro de Tecnologia da Informação Renato Archer

IMA – *Instituto de Macromolécula Professora Eloisa Mano;*

IQ – Instituto De Química

LNES – Laboratório Nanotecnologia e Energia Solar

UFRJ – Universidade Federal Do Rio De Janeiro

UNICAMP – Universidade Estadual de Campinas

Concepts

B – Backward

F – Forward

FA – Formamidium

GQD – Graphene Quantum Dot

HI – Hysteresis Index

IPA - Isopropanol

J_{sc} – Short-Circuit Current Density

MA – Methyl Ammonium

OPV – Organic Solar Cell;

PCE – Power Conversion Efficiency

PSC – Perovskite Solar Cells;

V_{oc} – Open-Circuit Voltage

1. INTRODUCTION

The energy sector is one of the branches of engineering that can be considered fundamental for maintaining human life. Its influence ranges from producing food, pharmaceuticals, water treatment, lighting, operation of electronic devices, computers, cell phones, means of transport, and even the health sector as essential equipment in surgeries. Still, the accelerated process of globalization, the advent of new technologies, and population growth make it even more urgent to develop solutions to meet this growing global energy demand. Another concern is the rapid depletion of conventional energy sources, such as fossils and petroleum. The environmental concern and preservation of the planet is also essential item to be evaluated. Therefore, it is crucial to invest in research related to the development of new technologies responsible for the production of energy in a more efficient, lasting way that at the same time does not have so much environmental impact.

The production of energy from reusing sunlight is one of the most promising ways for the world's energy supply. Photovoltaic cells can be subdivided into different technologies based on the specificity and combination of materials used. The first generation is based on silicon and gallium arsenide devices. The second generation introduced the use of thin films, along with architectural control, the use of more economical materials, and introducing molecules of the selenide (SiGs) and telluride (CdTe) groups.

The main objectives of third-generation solar cells are to increase efficiency, stability, flexibility, and productivity on an industrial scale while tending to reduce the cost of manufacturing the devices. Thus, its ramifications emerged from different types of third-generation devices due to the differentiation of the materials used, the architecture, and the working principle of solar cells. The most important classes of this third generation are dye-sensitized solar cells (DSSCs), organic photovoltaic cells (OPV), quantum dot solar cells (QDSC), multiple junction solar cells (MJSC), and perovskite solar cells (PSC). Finally, the fourth generation of solar cells combines the low cost and flexibility of thin polymer films with the excellent stability of nanomaterials such as metallic oxide nanoparticles, carbon nanotubes, graphene, and derivatives (LUCEÑO-SÁNCHEZ; DÍEZ-PASCUAL; CAPILLA, 2019). Among the emerging solar cells mentioned above, perovskite devices have gained much prominence in recent years because, in such a short time, they have reached energy conversion efficiency values comparable to and even higher than the most common commercial silicon-based solar panels (EPERON; HÖRANTNER; SNAITH, 2017).

The photovoltaic effect is based on creating a voltage or electric current due to light absorption. In semiconductors like perovskite, the electron in the highest occupied molecular orbital (HOMO) must be excited by a specific quantum of energy to reach the lowest unoccupied molecular orbital (LUMO). When this electron makes the energy jump from HOMO to LUMO, overcoming this energy difference defined as bandgap energy, it forms electron-hole pair (exciton) (ZENKER *et al.*, 2012). Then, this quasiparticle can undergo an efficient dissociation generating free charges, the positively charged ones being known as a hole, due to the representation of the absence of the electron in the HOMO, and the negative being the electron itself. This is due to the electrostatic forces and affinity of the adjacent layers arranged in a stack, forming the device circuit. In this way, both the positive and negative charges, after being efficiently separated, are conducted through the circuit in opposite directions, generating the electric current. The transport of charges takes place through their interaction with the materials that constitute the adjacent layers of the solar cell (LICHTENEGGER *et al.*, 2022).

It is worth mentioning that the appropriate combination of the energy levels of the molecular orbitals of each layer, the quality of the interface between the nanofilms, and the compatibility of the materials are as important as the quality and efficiency of the material responsible for the photovoltaic effect for the good performance of the device. The electron transport layer (ETL), located adjacent to the perovskite film, is responsible for the efficient extraction and conduction of electrons to the cathode. One of mthe biggest challenges of PSC are related to the improvement of these adjacent layers, mainly in the mobility of electrons and their interfaces with the adjacent films (MAHAPATRA *et al.*, 2022; RONG *et al.*, 2015).

Therefore, the present work aims to study the preparation of different combinations of materials in ETL in perovskite solar cells. Thus, the present study is focused on the fabrication and evaluation of the functioning of perovskite photovoltaic devices proposing different modifications in the ETL based on SnO_2. The main modifications are incorporating titanium dioxide and different types of graphene in various proportions, preparation of SnO_2 nanofilms in distinct methodologies, and even evaluating double layers of composites in ETL.

2. LITERATURE REVIEW

2.1 BACKGROUND AND RELEVANCE OF THE TOPIC

The main sources of renewable energy are hydro, wind, biomass, geothermal, ocean, and solar. However, even these energy matrices have an environmental impact, but in a much smaller proportion than fossil fuels (RAHMAN; FARROK; HAQUE, 2022).

Hydroelectric plants cause deforestation, water contamination, and flooding in a very large radius close to their facilities, thus directly harming local ecosystems (DASH; DASH; SETHI, 2022). On the other hand, the efficiency of wind turbines depends on an irregular phenomenon, the wind due to air temperature variation. Also, it generates noise pollution, electromagnetic interference, and climate changes that drive away the local flora and fauna, as a direct consequence of the migration of birds and other land animals (FARINA; ANCTIL, 2022). Biomass also drastically affects green areas, local fauna, and flora; there is a release of gases, but less polluting than fossil sources, and it contributes to acid rain (AWOSUSI *et al.*, 2022). Geothermal plants also release gases into the atmosphere, such as H_2S, causing land subsidence and even increasing the temperature around their installation, unbalancing the ecosystem (YILMAZ, 2022). Ocean plants also locally deteriorate the fauna and flora due to the presence and movement of the instruments necessary for energy conversion, in addition to presenting difficulties in the maintenance of their installations (GOURVENEC *et al.*, 2022).

The main environmental impact of solar energy is related to the materials used to manufacture its optoelectronic boards (RAHMAN; FARROK; HAQUE, 2022). However, this is easily resolved based on disposal logistics and awareness. Considering the problems related to the origin of the materials and also infrastructure needed, all other matrices also present the same problem. The photovoltaic energy matrix also needs sunlight for its operation. However, the sun can supply the planet with about 10,000 times more energy than what is needed for global daily consumption, making the argument of daylight dependence a disadvantage and inconsistent (RÜHLE; SHALOM; ZABAN, 2010).

Among other materials, perovskite solar cell (PSC) technology has stood out among photovoltaic devices. It is because, in less than ten years of development, it has already achieved energy conversion efficiency (PCE) values of 25.2% in single junction and 31.3% in multiple junctions (Tandem), as certified by the National Renewable Energy

Laboratory (NREL). Such values are comparable to single crystal silicon devices that have already reached their theoretical limit in practice. Figure 1 shows the evolution of the efficiency of photovoltaic devices as a function of the year, highlighting the emerging solar cells.

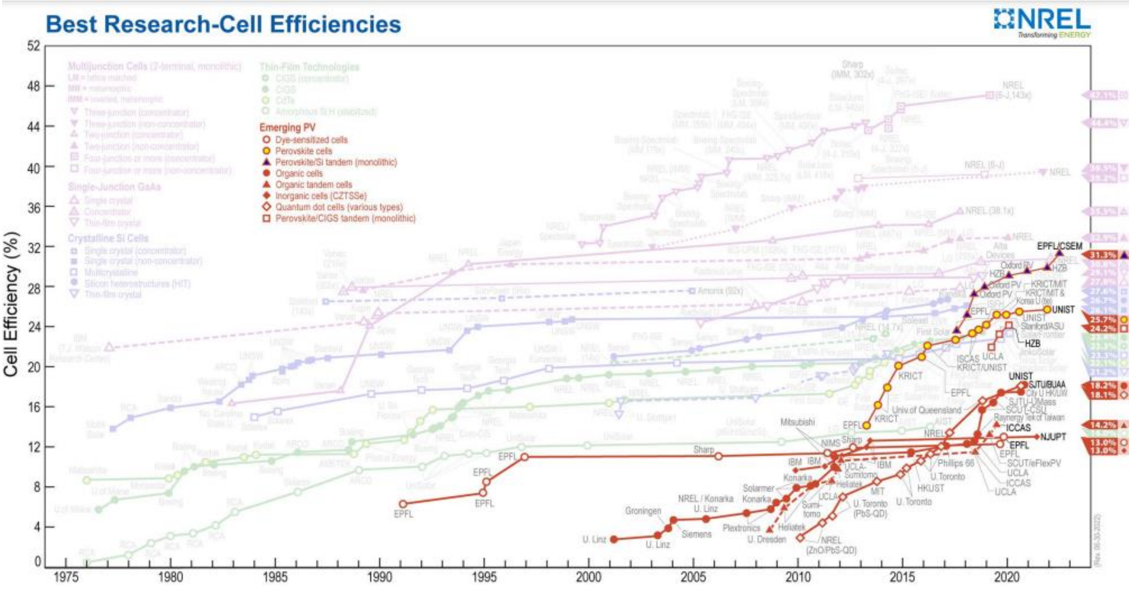

Figure 1: Best Research-Cell Efficiencies: Emerging Photovoltaics.

Source: National Renewable Energy Laboratory (NREL), 2022.

The interface phenomena between the layers of photovoltaic devices are one of the biggest challenges to be solved. Thus, many studies focus on understanding and improving the adjacent layers of the active layer, which is responsible for the photovoltaic effect (WANG, Junxian *et al.*, 2022). The electron transport layer (ETL) is responsible for assisting in the efficient dissociation of excitons according to the electron affinity and level of the HOMO and LUMO orbitals. Still, it should have high electron mobility, a good interface, and interaction with perovskite. In this context, developing research related to the ETL is extremely important since the active layer is already capable of generating a high amount of charge carriers. However, they are not fully converted into electric current due to problems related to adjacent layers such as ETL and the hole carrier layer (HTL). Another aspect is that problems in the ETL have a more drastic influence on the efficiency of PSC since this layer is responsible for the transport of electrons, which are the most influential in the generation of electrical energy (HUANG, Yulan *et al.*, 2020). It is also possible to manufacture high-efficiency devices without HTL, known as HTL-Free devices, which is not yet possible regarding the removal of ETL.

2.2 OPERATION OF THIRD GENERATION’S PHOTOVOLTAIC TECHNOLOGY

The photovoltaic effect is a physical phenomenon related to the ability of an electron in a molecular semiconductor located in the HOMO molecular orbital to be excited when absorbing a defined quantum of electromagnetic radiation (photon), reaching the lower energy LUMO molecular orbital. Proper electronic distribution is an important requirement that makes possible the energy jump of at least one electron. Even so, the difference in the energy levels of HOMO and LUMO must be in the same order as the quantum energy of the incident solar radiation. The bandgap is defined as the amount of energy required for this electronic transition to occur, which mathematically represents the difference in energy states between HOMO and LUMO. Moreover, this electronic jump will only occur efficiently if the energy quantum of the photon of solar radiation presents at least the same energy amount as the material's bandgap (ZHU, Lingyun *et al.*, 2019).

The bandgap of these semiconductors matches with the wavelength range of solar radiation consistent with visible light, which makes it possible to create a voltage or electric current after the material is exposed to light, resulting in the formation of an electron-hole pair, known as exciton (WANG, Han *et al.*, 2020). The bandgap energy becomes very large if the HOMO and LUMO orbitals are too far apart. It makes the electron's excitation difficult due to the large potential energy barrier for such a transition. Such characteristic of the high energy value of bandgap is common to insulating materials with high electrical resistance and difficulty locomotion of charge carriers.

After the exciton is formed, its dissociation must occur to separate the electron from the hole efficiently. In the HOMO orbital, where the material lost the electron, there is momentarily a hole with a positive electrostatic characteristic corresponding to the displacement of this negative charge to the LUMO orbital. Coulomb interactions are responsible for holding the electron-hole pair together until an electrostatic force sufficiently strong to overcome the binding energy of the electron-hole pair, usually 2 meV to 40 meV in PSC, and breaks this interaction. Another possibility for this quasiparticle is the recombination process that, due to electronic relaxation, can stabilize the system due to the decay of the excited electron and interrupt the separation of charges (HINRICHSEN *et al.*, 2020).

The lifetime of exciton in perovskites is approximately 78 ns, and if its dissociation does not occur in this period, there is no effective generation of photocurrent (GAUTAM *et al.*, 2018). The dissociation process is extremely fast, taking about 2 ps. After dissociation, electrons and holes can be transported by charge carriers with a much longer lifetime, about 2 µs. For the ideal device, it is interesting that the exciton dissociation occurs quickly. Then the electron and the hole are transported by their respective charge carriers in opposite directions in the circuit. Carrier diffusion length (LD) is 100–1000 nm, which is a very interesting value considering that the total thickness of all stacked device layers generally does not exceed 700 nm (GAUTAM *et al.*, 2018).

In polymeric solar cells, these parameters are very disadvantageous, which makes perovskite materials more interesting and capable of achieving higher efficiency values. In these devices, excitons have binding energy twenty times greater (0.5 eV), diffusion length three orders of magnitude smaller (10 nm), and lifetime a thousand times smaller (460 ps). In contrast, charge carriers have a lifetime of 1-4 ps and diffuse up to a maximum of 10 nm, which means that the dissociation of armies in polymeric devices requires much more energy. At the same time, both the exciton and the charge carriers are more unstable, requiring faster processes that involve less distance (GAUTAM *et al.*, 2018).

Because of these disadvantages, polymeric solar cells rely heavily on interface processes with adjacent layers or heterojunctions to effectively separate the electron and the hole to generate the photocurrent. Exciton dissociation occurs at the interface of different materials' layers with different electron affinities (EA) and ionization potentials (IP). The difference in EA and IP between the two materials is that of the layer responsible for the photovoltaic effect. The adjacent one with the duty of transporting the produced charges generates electrostatic forces at the interface that more efficiently separates the electron and the hole. Thus, the material with the highest EA collects the electron, while the hole is transported to the layer with the lowest IP. In other words, the electron is captured for the ETL layer, while the hole, for the HTL layer, until it reaches their respective electrodes, generating the photocurrent.

An alternative to favor the dissociation of exciton in free charges is the combination of different materials within the active layer. One has the characteristics of an electron acceptor, while the other has an electron donor. This strategy is known as heterojunction devices, common in polymeric solar cells that insert nanoparticles with electron-accepting properties into the volume of the active layer. The reason is that the polymer cannot efficiently dissociate the exciton, which makes such separation dependent on the interfaces between the polymer and the nanoparticle created in the volume of the active layer. It potentiates the electron-hole separation within the volume of the active layer, reducing the high dependence of the interface with the ETL and HTL layers of the device. One of the major impacts is the immediate increase of free charges, favoring a greater photocurrent density, allowing a higher energy conversion efficiency. In PSC, the generation of free charges is almost instantaneous. So, there is no big dependency on the interface with an electron-acceptor material. In addition, perovskite can transport the electron and the hole more efficiently, due to its high charge mobility, to its respective selector layer without creating interfaces, as is required in polymeric devices (NAN; ZHANG; LU, 2019).

The organization of the device in layers according to the difference in physical properties favors even more for directing these charges to their respective electrical poles, making the device more efficient. In addition, the ETL and HTL layers can exhibit hole and electron blocking properties, respectively. It enhances the direction of charges to their electrical poles properly. Consequently, it reduces the probability of recombination of these charges, which also tends to improve the uptake of charges by the electrodes. If the charge mobility of the photovoltaic material is not high enough, the charge carriers have a high probability of recombining with other particles, quantum quasiparticles, or crystal lattice defects with opposite charge (TURREN-CRUZ; HAGFELDT; SALIBA, 2018).

The photocurrent reduction may be due to difficulties in exciton generation and the charge transport processes to the electrode. The recombination processes can occur in the active layer and the volume in the other thin films of the device. That is, it is not only in the production of charges that the device's efficiency can be reduced but also in the processes after its generation. It is often difficult to distinguish which of these phenomena harms the circuit. Therefore, understanding the charge carrier recombination mechanisms is crucial information to recognize device performance issues or how to optimize them.

Wagner *et al.* (2017) reported that the quality of the interface between the layers and the kinetic processes of crystallization of the films alter the quantum efficiency. In general, it is desired to obtain homogeneous, compact, thin films with good adhesion to the adjacent layers or substrate, low concentration of defects, the lowest possible fraction of adsorbed liquids or gases, and lower porosity. Such characteristics are related not only to the types of materials used but also to the processes employed to produce thin films.

Spin coating is the most common method of deposition of layers of solar cells, which can be used for the active layer and the others. Such a technique involves depositing a layer from a solution dripped onto a rotating substrate. There are two major variations of this technique: static and dynamic mode. The static mode is when the film precursor solution drips and then starts rotating the substrate. The second function, the solution dripping, is performed while the substrate rotates. Each type of material has an optimized condition, be it among the mentioned modes, the rotation speed, the number of steps, or the processing time. Such parameters drastically influence the layers' homogeneity, crystallization, and thickness.

Another possibility is the combination of processes to obtain a film according to the project’s requirements. In the deposition of perovskites, it is very common to use anti-solvent or gas blasting for precipitation. Annealing is also practical and can be combined with other strategies to ensure solvent elimination and increase the crystalline fraction. In addition, this heat treatment in some materials, such as perovskite and metallic oxides, can take advantage of higher temperatures to act as a sintering mechanism, contributing at the same time to solvent elimination, porosity reduction, increasing compaction, and also activating the crystal structure of the unit cell (XIANG *et al.*, 2020).

The thickness of the device layers is the main parameter to be controlled, which is drastically affected according to the selection of the deposition technique. Increasing the volume of the active layer tends to increase the capacity of the semiconductor to generate excitons. On the other hand, this also increases the average path the charges must travel to reach their respective electrodes, implying a greater probability of recombination processes occurring during their transport. Still, increasing a layer's dimension also increases the probability of defects occurring in its crystal lattice that can deflect or capture electrons or holes. In this way, each material presents its optimal parameters. In general, it tries to consider increasing the layer thickness, to improve the photocurrent production with the smallest possible recombination effect due to the increase in the distance that the charge carriers must travel.

When the charge carrier reaches the edge of a layer, it faces another problem, the main interface problem, which is the potential barrier to transition from a film composed of one material to another. In general, charges and their carriers must have kinetic energy sufficiently above the potential energy barrier to jump to the adjacent layer. Thus, it is interesting that the layers in question have as much affinity as possible to reduce the distance between them and present a better interface. It is also worth mentioning that the lower the electrical resistance and the greater the mobility of charge carriers, the lower the energy losses through the path of electrons and holes (ATTIA; ELGENDY; RIZK, 2019).

Also, concerning the interface, the distribution of energy levels of the HOMO and LUMO orbitals of the subsequent layers must be adequate to generate a preferential direction for the transport of electrons and another direction for the holes. At the active layer interface, in addition to the potential barrier, there is a potential difference that favors exciton dissociation. The electron is attracted to the adjacent layer with the highest electron affinity, which aligns with a lower energy LUMO orbital. In turn, the hole tends to move to the layer with the highest ionization potential and the highest energy HOMO orbital. Consequently, this displacement of charges at the interface generates a potential difference that induces an electric field accelerating the charge carriers towards their respective electrodes.

However, increasing the difference between the energy levels to maximize the effect of electron affinity or the ionization potential makes the potential barrier even higher. If the difference between the occupied orbitals is very large, the migration of holes does not happen. And the same phenomenon occurs if the difference between the unoccupied orbitals is exaggerated, not allowing the electrons to jump. On the other hand, the difference in energy levels cannot be too small; otherwise, the induced electric field will have low intensity and little efficiency in acceleration, charge transport, or exciton dissociation (GAO *et al.*, 2018). Figure 2 shows the energy diagram that must be respected in the manufacture of devices to generate a cascading effect of charges.

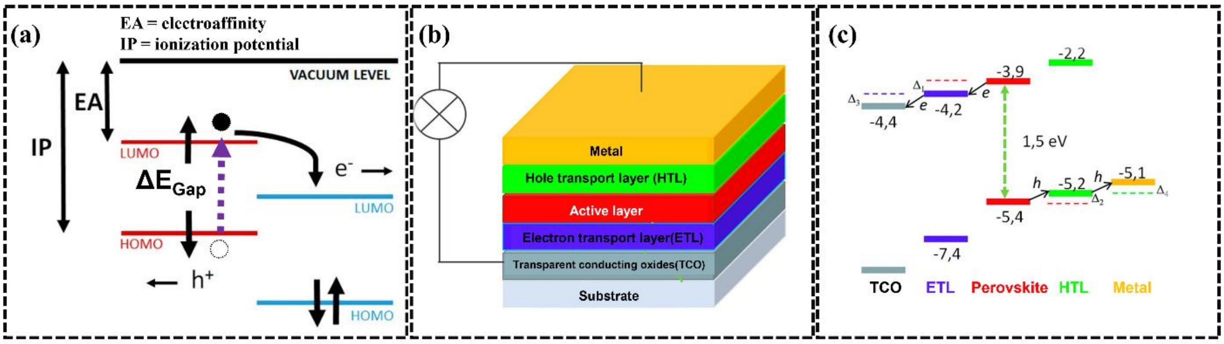

Figure 2: Charge separation of an exciton into a free electron/hole pair (a); layer deposition structure of a device (b); alignment of device molecular orbital energy levels and the cascading effect of charge migration (c).

Source: Adapted from LUCEÑO-SÁNCHEZ, DÍEZ-PASCUAL and CAPILLA (2019); INTEREMPRESAS (2016).

Once exciton dissociation occurs and each charge is conducted to its respective adjacent layer, the probability of recombination is reduced. That is because when generating a flow of charge, a magnetic field is created that tends to conduct and act as a free path, orienting the electron and the hole. Thus, once ensuring a proper alignment between the molecular orbitals of the device materials, concerns in the ETL and HTL layers are electrical resistivity, mobility of charge carriers, and morphology defects, which act as traps and deflection of electrons or holes (ZHANG, Guichuan *et al.*, 2020).

2.3 SOLAR CELL ARCHITECTURE

As already mentioned, photovoltaic devices are manufactured from the subsequential deposition of nanometric layers based on materials with different characteristics and physical properties. Each component and organization are selected according to the requirements for generating electrical energy from solar radiation. Depending on each combination of materials in a particular solar cell, the architecture also presents changes in the order and the number of layers deposited. In addition, the first difference between the types of devices is the choice of material that will support its architecture, which can be rigid, with glass being the most used, or even flexible, such as poly(ethylene terephthalate) (PET) (RAMAN, Vivekanandan; JO; KIM, 2020). The determination between rigid and flexible substrates must be carried out knowing the mechanical behavior of the other layers, whether they are capable or not of deforming several times without harming the device's operation.

Currently, perovskite photovoltaic devices, as a layer responsible for the photovoltaic effect, have as a conventional architecture the subsequent deposition of the following constituents:

I. Substrate, whose main function is to support the other layers;
II. Transparent conducting electrode (TCE) that acts as the cathode of the circuit, or even so-called transparent conducting oxides (TCO) because the main materials that constitute this layer are formed of oxides;
III. Electron transport layer (ETL) that has the competence to conduct electrons and block holes;
IV. Active layer that holds the function of the light harvesting and charge carrier generation;
V. Hole transport layer (HTL), which is responsible for the injection/transport of holes and/or electron blocking;

VI. Metal electrode of low work function as the anode.

Compared to this organization, the architecture understood as inverted can also be used, which is called due to the inversion of the position between the ETL layer with the HTL, thus changing the device polarization, causing the inversion of the anode and cathode. Figures 3 (a) and (b) exemplify the assembly of perovskite devices in conventional and inverted architecture, respectively. It is worth mentioning that, regardless of the architecture, it is desired to prepare homogeneous layers with good interfaces, bandgap optimization, and alignment of the HOMO and LUMO orbitals to obtain high energy conversion efficiencies.

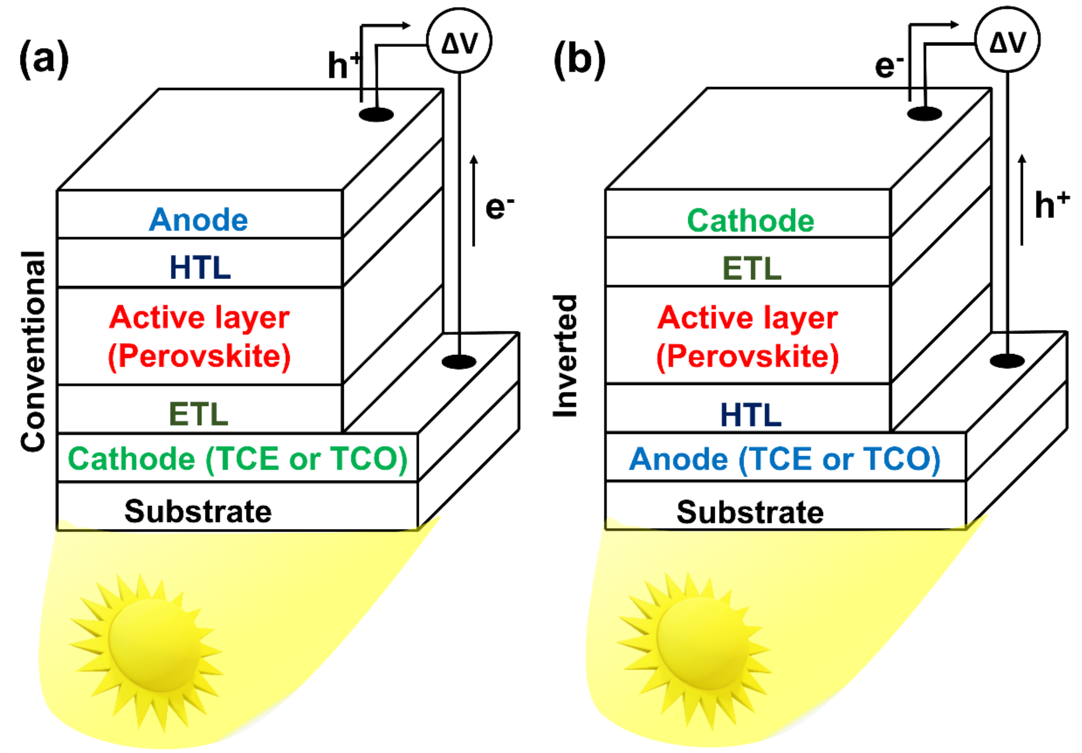

Figure 3: Layer stacking structure of perovskite photovoltaic devices with the conventional architecture in (a) and inverted in (b).

Source: Prepared by the author.

Some studies over the years have shown that the inappropriate combination of ETL and HTL materials with the architectures does not generate devices with good PCE values. It even stimulates the degradation of perovskite. Therefore, it is worth noting that it is impossible to guarantee that a good ETL material for the conventional architecture will work well in the inverted one (RAMAN, Vivekanandan; JO; KIM, 2020).

In general, one of the main problem in devices is the interface between the perovskite and the adjacent HTL and ETL layers. That is a consequence of the fact that at the interface with the active layer, the scattering of electrons and holes occurs, dispersing charge and reducing the circuit current. If the adjacent layer also does not present good mobility of charge carriers, a local concentration of electrons and holes can occur, favoring recombination.

The perovskite layer film is usually prepared from a precursor solution directly on the device. It generates many problems related to the reproducibility of the devices, which is related to the purity of the reagents, adequate equipment for preparing the solutions and for deposition, and the researcher's experience and care during manufacture. These materials are very sensitive to ambient temperature and humidity, even inside atmosphere conditioning equipment such as a glovebox (SALIBA *et al.*, 2018).

Wang and collaborators (2019), as well as many other researchers, noticed that in the process of deposition of the perovskite layer, a part of the active layer film permeated the porosity defects of the adjacent layer (HTL or ETL, depending on which architecture). Thus, the idea arose of creating a region with a gradual transition between the perovskite structure and the closest layer. Thus, the concept of combining a layer with a mesoscopic structure that permeates the active layer with another compact layer of the same material was developed (ZHANG, Yi *et al.*, 2017). It is usually done for ETL material in conventional architecture while inverted for HTL. However, the preparation of porous perovskite structures tends to reduce the solar cell's efficiency drastically. In fact, this interface within the active layer of perovskite acts as a defect that captures the charge carriers and reduces the photocurrent (WU, Jiawen *et al.*, 2020).

Defects can be classified as shallow as a vacancy, interstitial atoms, or substituent, but they can also be related to shallow or deep energy levels (XIE *et al.*, 2021). The larger the size of the defects, in general, the more they harm the device as they are heterogeneities in the perfection of the crystal lattice that capture the charge carriers. In this sense, the grain boundaries and the interfaces are the recombination centers. Another aspect is that, after the formation/sintering of the perovskite solid film, the process of permeation of the next layer on top would be inefficient, not giving rise to the desired gradual transition zone. The interface would also not be very good and have a high surface area between HTL or ETL with perovskite. Moreover, if the solvent of the layer to be deposited above the perovskite also dissolves it, it would destroy the crystallinity of the active layer. On the other hand, if the solvent does not have an affinity for perovskite, it will generate a repulsion between the layers and will not allow an adequate spreading of the film.

The first PSC structures were planar, and it was desired that the HTL and ETL layers were as compact as possible so that the porosity or voids of the films would not deflect the light, optimizing the useful volume of material in the device (ZIMMERMANN *et al.*, 2019). After verifying that the solvents of the perovskite precursor solutions, such as dimethylformamide (DMF) and dimethylsulfoxide (DMSO), do not break down the layers of metallic oxides, such as those of titanium and tin oxide, used as ETL, the trend began to try to increase the interaction and gradual mixing between adjacent layers with perovskite. The aim would be to improve the interface as it is possible to increase the surface area, allowing a greater flow of charges.

Another variation of the PSC architecture is the so-called triple mesoscopic, consisting of three mesoporous layers (ETL, a carbon layer, and a spacer), which are within the volume of the active layer. However, this architecture improves the long-term stability of perovskite devices even more than the standard mesoscopic one. Sheng *et al.* (2020) reported that there is a reduction in the open-circuit voltage (V_{oc}) of the device, which can limit the range of high PCE values (SHENG *et al.*, 2020). On the other hand, Zhao et al. (2019) reported that this situation could be circumvented with the proper regulation between the energy levels of the occupied and unoccupied orbitals of the materials employed, more gradually, using the combination of zinc and tin oxides (ZHAO, Jianhong *et al.*, 2019). Figure 4 exemplifies the configuration of possible architectures for perovskite solar cells combining such developments in mesoporous layers.

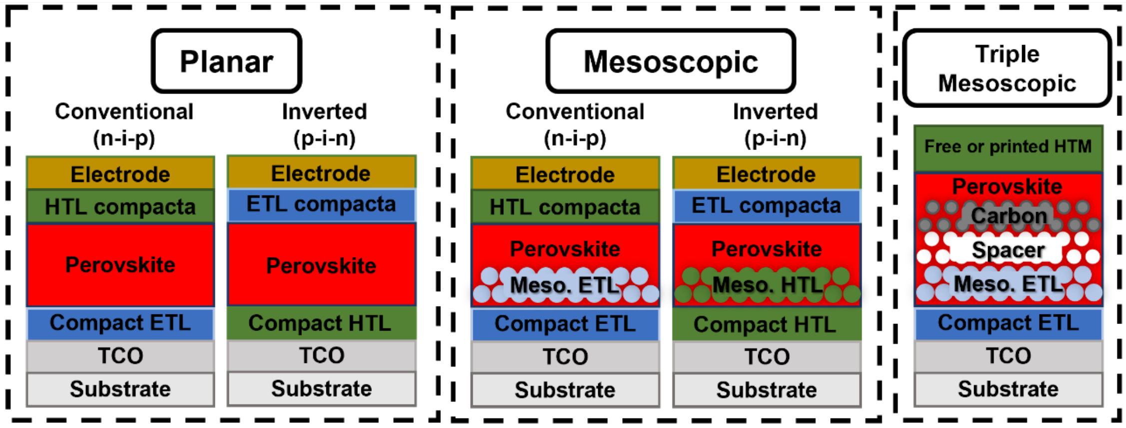

Figure 4: Planar, mesoscopic, and triple mesoscopic configurations of perovskite solar cells.

Source: Prepared by the author.

2.4 PEROVSKITE SOLAR CELLS (PSC)

The term perovskite is designated to a large group of compounds with a cubic crystalline structure, such as the mineral calcium titanate ($CaTiO_3$). These materials have the general formula ABC_3, where A and B are cations, and C is an anion, usually the ion O^{-2} or halide ions. It is noteworthy that the size and arrangement of these atoms in the unit cell directly affect the properties of the material (ZHANG *et al.*, 2017). Figure 5 shows the face-centered cubic arrangement (FCC) of perovskite.

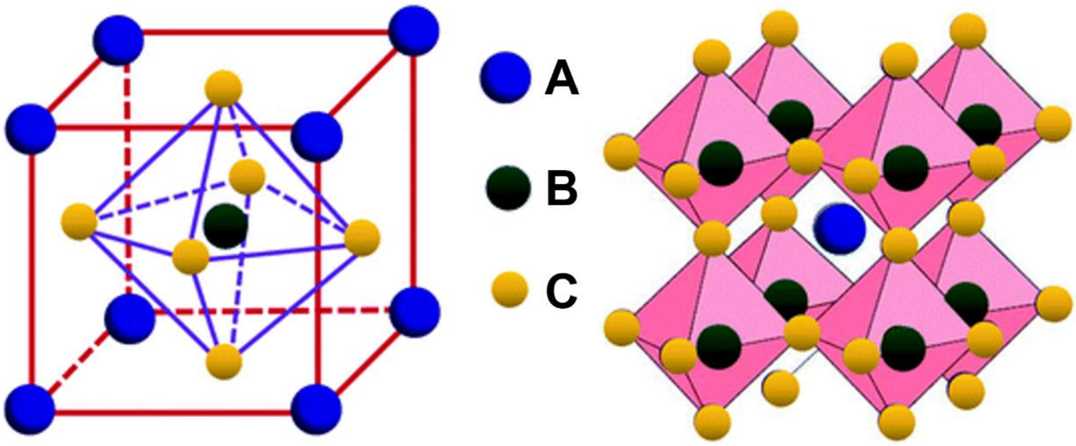

Figure 5: Structure of perovskites with ABC_3 formula.

Source: Adapted from YI *et al.* (2019)

Perovskite solar cells have been the subject of several research groups due to their considerable evolution in less than a decade and the improvement of their architecture. Organic-inorganic hybrid perovskite devices achieved more than 25% PCE (ICHWANI *et al.*, 2022). Other advantages are its intrinsic characteristics, such as high absorption coefficient in a wide region in the visible solar spectrum, direct bandgap, high mobility of electrons and holes, ambipolar transport and tunneling, and high charge and diffusion length that exceeds micrometers in single crystals. Consequently, it achieves higher PCE values than other materials used in emerging solar cells and competes directly with silicon solar cells (CASE; BEAUMONT; KIRK, 2019).

Hybrid organic-inorganic perovskites are the most studied and, in general, are made up of methylammonium lead iodide ($CH_3NH_3PbI_3$, abbreviated as $MAPbI_3$), as well as formamidinium lead iodide ($HC(NH_2)_2PbI_3$, abbreviated as $FAPbI_3$) (SUZUKI; OKU, 2022). Generally, its synthesis is carried out on top of the substrate with the sequential addition of its precursors, methylammonium or formamidinium iodide, which crystallize when reacting with lead iodide. In addition, perovskite may require heat treatments to achieve the film's desired structure and morphology and eliminate the solvent or unwanted molecules. Its synthesis on the device is carried out under an inert atmosphere and mostly via spin coating with the aid of solvents such as DMF/DMSO in a 4:1 ratio (TAVAKOLI; PROCHOWICZ; *et al.*, 2018).

On the other hand, perovskite solar cells have low stability in environmental and climatic conditions due to their high rate of degradation by the effect of humidity, oxygen, UV radiation and visible light, heating under aplication of electrical voltage, dissolution process (solvents, solutes, additives), temperature and also has mechanical fragility. It currently makes commercializing all this innovative technology with high PCE values unfeasible since these conditions are common while the device works (BISQUERT; JUAREZ-PEREZ, 2019). Therefore, studies look for strategies to improve both the efficiency and stability of this class of devices. The most recent works demonstrate that the improvement of perovskite stability can be performed by different methods, such as the insertion of organic groups or stabilizing inorganic cations in its composition, additive engineering, device encapsulation, and finally, the development of strategies focused on the improvement of the interface of the active layer with the adjacent ones (DENG, Kaimo *et al.*, 2021).

The insertion of groups such as methylammonium (MA) and formamidinium (FA) from their respective iodides (MAI and FAI) aims to generate a three-dimensional structure that generates a lower migration of iodide ions while stabilizing the unit cell, improving compatibilization and solubility generate high values of PCE (ZHAO, Yang *et al.*, 2022). The insertion of cations such as Cs^+ and rubidium Rb^+ also tries to improve the stability and efficiency of the devices. It is worth noting that the methylammonium group is very volatilizable and has low thermal stability. Thus, many researchers are directed toward partially replacing the amount of MA^+ by adding both FA^+, Cs^+, and Rb^+ (NIU *et al.*, 2021). In this context, what causes the reduction of device efficiency, in general, is the conversion of the photovoltaic cubic to hexagonal phase, called yellow phase, which has low energy conversion activity and its predominance at room temperature is energetically favorable (SHUKLA *et al.*, 2021; ZHAO, Yang *et al.*, 2022). This conversion can occur while the device runs, reducing the PCE over time.

The stabilization of the system can also be done through additivation with salts, such as MACl or CsCl that act as dopants. The great difference between this strategy and the previous one is that after the heat treatment for sintering and crystallizing the perovskite, usually at 100 °C for at least 2-30 min, these salts are volatilized and do not remain in the perovskite structure (DENG, Liangliang *et al.*, 2021). The improved stability is due to the stabilization of the cubic phase, mainly at the interface, and the increase in charge transport, mostly due to the improvement of morphology on the surface in contact with the ETL (HOU *et al.*, 2021). It is worth noting that the nucleation, crystallization, and sintering temperatures of perovskites, in general, are extremely low because they have low activation energy (56.6–97.3 kJ mol^{-1}) compared to the amorphous silicon (280– 470 kJ mol^{-1}) (HOU *et al.*, 2021).

Encapsulation is a methodology used to protect solar cells against degradation. Its mechanism, in general, is based on the device's coating with a polymer acting as a barrier that separates it from the atmosphere and natural weather. In addition to mainly guaranteeing the physical barrier to gases, moisture, and oxygen, a good encapsulation, must also be insulating and with the highest possible transmittance in the wavelength range of the absorbing material (RAMAN, Rohith Kumar *et al.*, 2021). Some articles even try to incorporate the shielding effect at specific wavelengths that accelerate the degradation of the active layer. Inorganic encapsulation uses mainly glass, silicon nitrides, and metal oxides as a barrier. On the other hand, organic encapsulation is dominated by polymers due to the ease of processing, low cost, and properties compatible with this application. The most used polymers are ethylene-vinyl acetate (EVA), Surlyn™ (a DuPont's ionomer resin-copolymer of ethylene and methacrylic acid), epoxy resin, polydimethylsiloxane (PDMS), poly(methyl methacrylate) (PMMA), thermoplastic polyurethane (TPU), polytetrafluoroethylene (PTFE), polyisobutylene, polyethylene terephthalate (PET), poly(vinyl alcohol-co-ethylene)(EVOH), poly(p-chloro-xylylene), polyimide, paraffin, organo siloxane, hot melt polymer foil, silicone, adamantane (RAMAN, Rohith Kumar *et al.*, 2021).

As already highlighted, interface problems are predominant in reducing efficiency and its loss under operation, generating low stability. In this way, understanding well and improving the interfaces between perovskite and adjacent films (ETL and HTL) are of utmost importance. In addition, the optoelectronic behavior of these materials in their volume also alters the functioning of solar cells.

The most used HTL for the conventional architecture of these photovoltaic cells is spiro-OMeTAD ($C_{81}H_{68}N_4O_{80}$, chemical name 2,2',7,7'-Tetrakis(N,N-di-p-methoxyphenylamino)-9,9'-spirobifluorene). However, in addition to this material being very expensive, making commercialization unfeasible and requiring dopants to improve the mobility of hole carriers, it also undergoes degradation processes with moisture and with the migration of iodide ions from the perovskite layer. In addition, spiro-OMeTAD tends to undergo surface modifications in contact with perovskite, which can cause morphology problems and even generate large voids due to its decomposition and interface instability (JENA *et al.*, 2018). Poly[bis(4-phenyl)(2,4,6-trimethylphenyl)amine] (PTAA) is another HTL alternative that has high hole mobility and adds superior stability compared to spiro-OMeTAD devices. But this material is also very expensive (TZOGANAKIS *et al.*, 2021).

Another material for the HTL layer, but more used in inverted architecture, is PEDOT:PSS, which usually solves the mentioned problems; however, its hole mobility is lower, which makes its processing and doping even more important. This film is also incapable of blocking electrons. In addition, water is generally used as a solvent, which, added to its acidic character and hygroscopic characteristic, can facilitate the degradation of perovskite or even interfere with the other layers of the device (XIA; YAN; LIN, 2021).

In the electrode layer deposited on the substrate, indium tin oxide (ITO) is usually used, which functions as a transparent conductive cathode (in the conventional architecture) or as a transparent conductive anode (in the inverted architecture). However, ITO is a material that increases the cost of the solar cell due to the price of indium and its scarcity, which can represent up to 50% of the device's cost (LIU, Gengling *et al.*, 2022). In addition, this material is not recommended for application on flexible substrates due to its mechanical fragility, forming films susceptible to cracking, which can even cause the device to collapse. ITO needs a reasonably high temperature to treat its layer, a problem for flexible polymeric substrates due to thermal degradation. Fluorine-doped tin oxide (FTO) is a cheaper substitute with stability and heat resistance superior to ITO (MAYIMELE *et al.*, 2022). However, it is necessary to use even higher temperatures to prepare its film. Even so, it has many voids and a tendency to provide a large leakage current, making this layer less efficient over time (VILLARREAL *et al.*, 2022).

Another important issue in terms of performance is the current-voltage hysteresis commonly seen in perovskite devices. Such a phenomenon is related to the difference between the backward (B) and forward (F) current density by voltage curve (WANG, Lipeng *et al*., 2021). The factors that affect hysteresis are still under debate, but it is most commonly attributed to mobile ion migration and high levels of recombination. Methods for reducing hysteresis include architectural suitability, alignment of the HOMO and LUMO orbitals, layer homogeneity, surface passivation, increasing lead iodide content, and general strategies to reduce recombination (VILLARREAL *et al.*, 2022; WANG, Lipeng *et al.*, 2021a). Figure 6 represents the hysteresis through the Current Density X Voltage (JV) curve and exemplifies the migration of electrons, holes, and ions that generate such an effect due to polarization and electric dipoles. Still, in this figure, it is possible to observe the effect of interface problems on the ETL acting as a defect that captures the charge carriers.

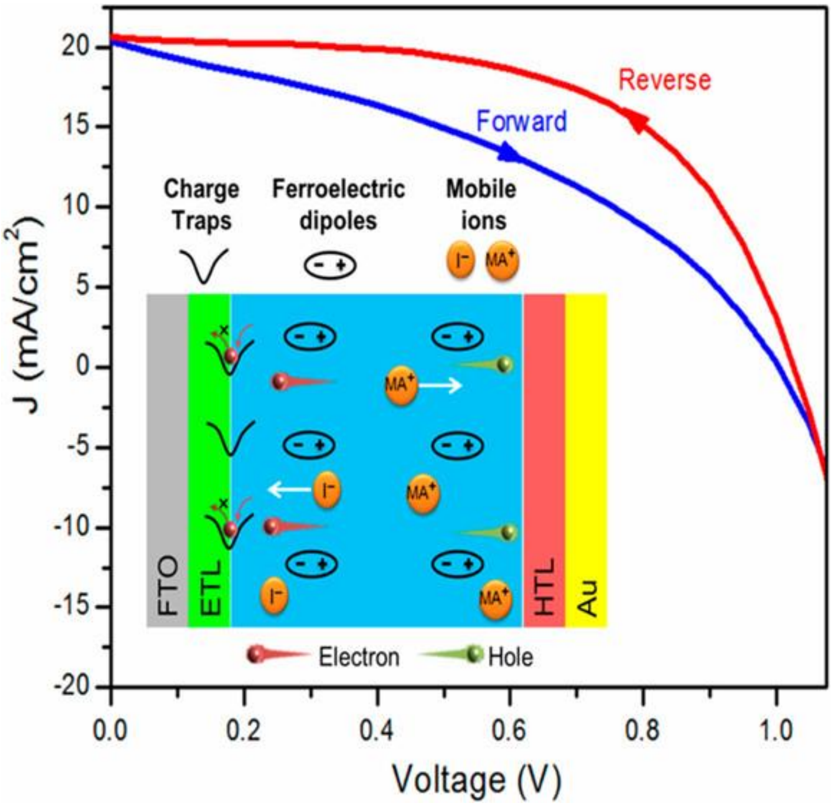

Figure 6: Exemplification of hysteresis through the JV curve and the mechanism of such a physical phenomenon.

Source: Adapted from CHEN *et al*. (2016).

CHEN *et al*. (2016) explained that the efficiency of the reverse scan increases with the increase of the scan rate. On the other hand, the efficiency in the direct scan decreases with the scan rate. Hysteresis becomes more pronounced when the sweep rate increases and hysteresis can be eliminated using a sufficiently slow sweep rate. Sweep range with different starting biases can also change device performance. Also, forward scanning with a more negative starting potential would deteriorate efficiency, while a reverse scan starting with a more positive applied bias could increase performance. It clearly demonstrates the importance of standardizing the parameters during the analyses, especially concerning reference and compared articles in the discussion of results. UNGER *et al*. (2014) demonstrated that preconditioning with light soaking in different polarizations can significantly influence the performance of the perovskite device. That is a consequence of light absorption under large positive applied voltage before characterization can dramatically improve the fill factor, short circuit current density (J_{sc}), and PCE. On the other hand, light absorption under large negative polarization can suppress its performance.

Reducing the capacitance of the perovskite interface with the adjacent films improves charge transport, allowing for substantial hysteresis relief. Furthermore, the difference in electron and hole mobility explains such a physical phenomenon. Hysteresis is difficult to prevent since the perovskite structure itself is formed by an ion arrangement in the ABC_3 stoichiometry. Consequently, a preference for the mobility of one charge carrier over the other may occur. Even so, the polarization of this structure tends to create oriented domains that, also favored by the migration of ions, alter the diffusion coefficient of the carriers. In this way, opposite polarization can be obtained depending on the direction of the JV curve, which, potentiated by the different mobility of the negative and positive charge carriers, generates profiles with unequal efficiencies (WANG, Lipeng *et al.*, 2021a). It makes it difficult to obtain the real PCE of the device since, under operation, such phenomena will occur. Generally, such real efficiency is approximately the average of the backward and forward curves. Hysteresis also tends to accentuate the degradation and reduce the stability of the device. Yet, it makes it possible to form electronic domains with irregular and heterogeneous properties (WANG, Lipeng *et al.*, 2021b).

Hysteresis can mask their real efficiency and reduce the properties and stability of devices. Most articles in the literature also present only the relative results of the backward curve with higher values or even just its PCE, without presenting adequate statistics of the devices. The reproducibility of perovskite devices prepared by spin coating is another problem. It is because there is a sequential deposition of layers, and the device's performance will be constituted by the mutual contribution of the quality of each film and its interfaces, the researcher's experience and reproducibility, the purity of the reagents, and the conditioning of the laboratory. SALIBA *et al.* (2018) reported a protocol for manufacturing high-efficiency devices. They point out that even experienced and renowned researchers in device manufacturing have problems with data dispersion and performance of their control devices. Figure 7 shows the efficiency of control devices based on CsMAFA and RbCsMAFA over two years of work by an experienced team of researchers.

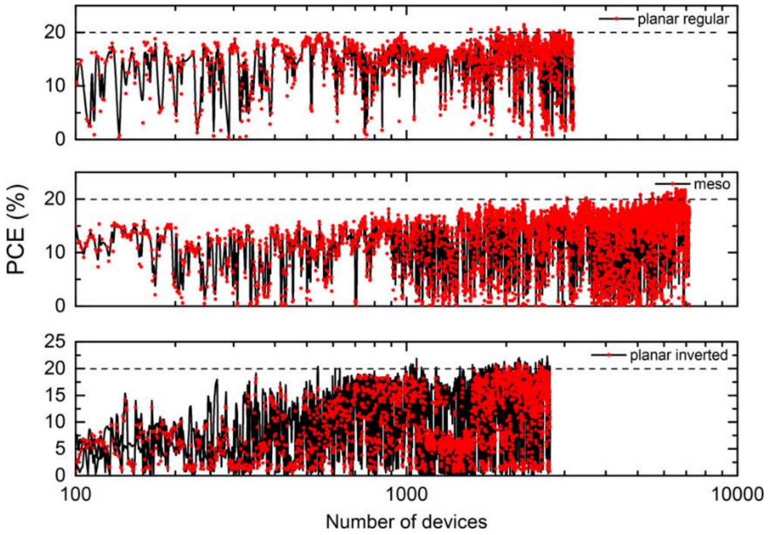

Figure 7: Power conversion efficiency as a function of devices produced in chronological order data collected over approximately two years of CsMAFA and RbCsMAFA perovskite solar cells.

Source: Adapted from SALIBA et al., (2018).

2.4.1 Lead Methylammonium Iodide Perovskite ($MaPbI_3$)

$MAPbI_3$ perovskite is widely cited in the literature for its easy synthesis and excellent PCE values. Thus, it is considered a reference for PSC. The efficiency of these devices is limited mainly due to the unavoidable defects at the interface of the carrier layers and the conversion from the photovoltaic cubic to the non-active hexagonal phase. FENG *et al.* (2022) used triphenylphosphine oxide (TPPO) as a post-passivation agent of defects in the device with structure ITO/PEDOT:PSS/$MAPbI_3$/PCBM/Bphen/Ag (where PCBM is a fullerene derivative, the phenyl-C_x-butyric acid methyl ester). The TPPO layer can protect $MAPbI_3$ from moisture and oxygen degradation and improve photoelectric properties. The optimized efficiency of TPPO-$MAPbI_3$ solar cells reached 14.9% PCE with negligible hysteresis behavior. The $MAPbI_3$ control device showed 13.7% efficiency. Encapsulated TPPO-$MAPbI_3$ PSCs increased stability, and samples remained at about 83% of their initial efficiency for 30 days at 35% relative humidity at 25 ˚C. The devices maintain about 87% initial efficiency after aging under an inert atmosphere in a glovebox for 1800 h at room temperature. $MAPbI_3$ has a bandgap close to 1.5 eV; most of the ETL used in the devices is of TiO_2 due to its high bandgap and the alignment of the unoccupied orbitals with that of perovskite (HU *et al.*, 2019). The high hysteresis in the combination of $MAPbI_3$ with TiO_2 is attributed to the low conductivity of holes (1.1×10^{-5} S cm^{-1}) compared to the high mobility of electrons (0.1–1 cm^2 V^{-1} S^{-1}) of ETL. It induces charge accumulation at the interfaces between TiO_2 and perovskite, which reduces efficiency in addition to causing hysteresis. ABDELHADY *et al.* (2016) reported that an interesting heterovalent dopant enabled the successful binding of Pb^{2+} with Bi^{3+} to reduce the bandgap of $MAPbI_3$ in a controlled manner in the range between 2.17-1.89 eV, being a promising strategy for the adequacy of the optical-electronic properties.

JUNG *et al.* (2020) overcame the challenge of efficiently combining SnO_2 with $MAPbI_3$ after ozone treatment for 25 min under the ETL layer. This treatment above SnO_2 allowed hydrophilizing of its surface to facilitate the spreading of the perovskite precursor solution more homogeneously and improve the morphology of the active layer. Figure 8 shows the optical microscopy during the analysis of contact angle with water, scanning electron microscopy of the surface of the substrate/SnO_2(ETL)/$MAPbI_3$ structure, and the cross-section of the device. The analyzes showed an improvement in wettability, which favored the formation of perovskite films with a better interface, fewer voids, and a slight increase in the grain sizes of the active layer, which potentiates greater conduction of charge carriers. The device treated with UV-ozone obtained 17.01 ± 1.34 % of PCE in the JV backward curve, while the control presented 13.78 ± 2.15 %.

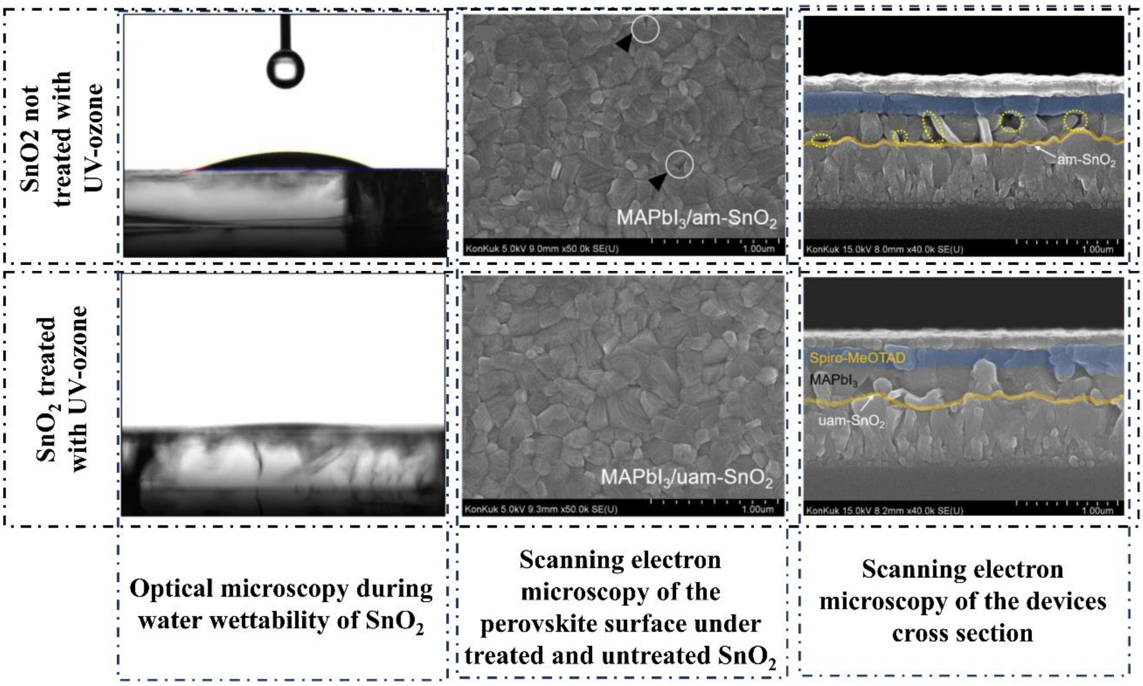

Figure 8: Micrograph obtained by optical microscopy during the measurement of contact angle with water of SnO_2 films treated and untreated with UV-ozone, scanning electron microscopy of the surface of the substrate/SnO_2 (ETL)/$MAPbI_3$ structure, and also of the cross-section.

Source: Adapted from JUNG et al., (2020).

2.4.2 CsMAFA

CsMAFA is the abbreviation for the stoichiometric formula $Cs_{0.05}MA_{0.12}FA_{0.83}PbI_{2.55}Br_{0.45}$ relative to perovskite with the addition of 5% Cs in the composition of $(FAPbI_3)_x(MAPbBr_3)_{1-x}$ (named MAFA), which is known to provide high-efficiency solar cells. This perovskite potentiates devices that use cations and methylammonium, and formamidinium in the ABC_3 structure, where “A” is the structure maintaining the proportion $(MAFA)_{0.95}(CsI)_{0.05}$, “B” the lead cation, and “C” the bromine and iodine anions. Another widely used cation is rubidium forming the perovskite RbCsMAFA or just RbMAFA. The main function of the insertion of Rb^+ and Cs^+ in the perovskite structure is to reduce radioactive recombination and eliminate non-reactive impurities, which makes the device more efficient and also tends to help in its stability (ZHANG, Mengmeng *et al.*, 2020a). It is worth noting that in the literature, there is a much lower amount of work in the area of CsMAFA compared to $MAPbI_3$ because the triple cation technology is extremely recent. But the few works in the literature already demonstrate that this perovskite performs significantly better.

SOLANKI *et al*. (2019) prepared devices based on MAFA perovskite with the insertion of Rb, Cs, and the combination of both in the FTO/compact-TiO_2/perovskite/Spiro-OMeTAD/Au architecture. Figure 9 (a) shows the data obtained from the JV curve in the forward direction of the device with the best performance. It is possible to observe an increase in photovoltaic parameters with the insertion of the mentioned cations, highlighting the combination of Cs with Rb obtaining PCE of 19.1% in its best device. Figure 9 (b) shows a statistical distribution of the prepared devices, confirming the improvement in efficiency and a slight reduction in data dispersion. The study concludes that Cs^+ incorporation to form CsMAFA perovskite suppresses defect density, adding to longer charge carrier lifetimes, lower photoluminescence quantum yield, and higher energy conversion efficiency compared to double cation perovskite (MAFA). However, the incorporation of Rb^+ generates a higher density of defects, favoring a decrease in the lifetime of the charge carrier and an increase in trap-assisted radioactive recombination, which represents a consequence of the formation of unwanted phases.

On the other hand, the RbCsMAFA perovskite presents extended lifetimes of charge carriers with balanced diffusion lengths, reduced defect densities, and much higher hole diffusion length. CsMAFA has the longest electron diffusion length among the samples studied, but with intermediate molecular and bimolecular recombination. Finally, it is worth noting that improved PCE is expected from more efficient charge extraction before charge recombination.

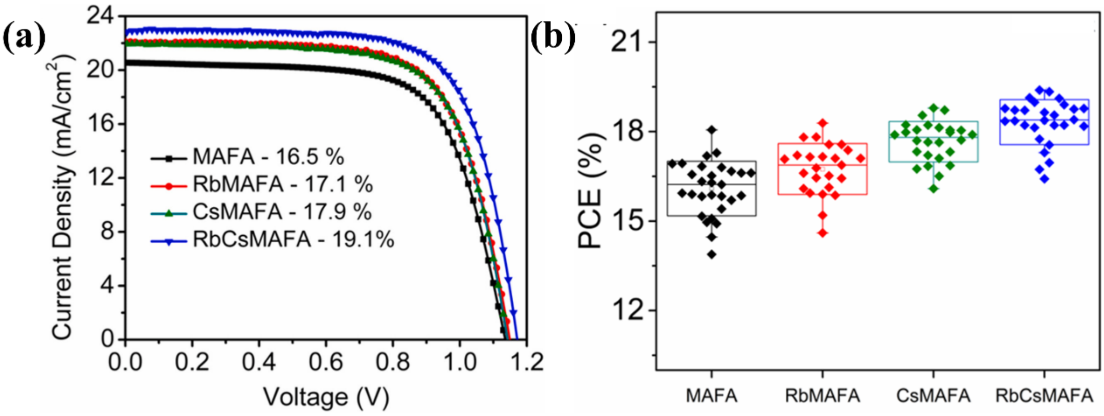

Figure 9: JV forward curves of the best devices under illumination manufactured with perovskite films constituted by different cations (a) and the distribution of PCE performance of the set produced and measured in the forward direction.

Source: Adapted from SOLANKI et al., (2019).

Passivation is a method to improve device stability, which generally aims to create a thin layer at the perovskite interface with a material that aims to protect the active layer, mainly against oxidation reactions. This way, the passivating material tends to oxidize the perovskite in sacrifice. Simultaneously, forms a protective layer that can also increase the gas barrier property and migration of unwanted species. HE *et al*. (2021) studied the quinacridone (QA) passivating effect on $MAPbI_3$ and compared their results with CsMAFA devices. The best $MAPbI_3$ devices reached 18.87% in the backward (B) scan and 16.59% in the forward (F) scan, and after passivation, with QA reaching 21.09%(B) and 20.13%(F). It demonstrates an improvement in PCE and a reduction in hysteresis as an effect of passivation. With CsMAFA, it improved by 21.17% (B) compared to the reference of 19.36% (B). Although the results of the direct curve were not presented, it can be seen that $MAPbI_3$ suffers a much greater property gain than CsMAFA. However, the improvement due to the passivating effect of CsMAFA with QA is undeniable, reaching devices with more than 21% PCE. In addition, it explains the difficulty of optimizing perovskite devices that already have very high-efficiency values, as is the case of CsMAFA.

ZHANG, Mengmeng *et al.* (2020) were the pioneers in using sodium p-toluenesulfonate (STS) as a surface modification of the CsMAFA perovskite film, providing trap state passivation and consequently a significant increase in PCE from 18.70% to 20.05%. X-ray excited photoelectron spectroscopy (XPS) demonstrated that the sulfonate anion ($–SO_3^-$) and the Na^+ cation of the STS were capable of interacting, respectively, with the Pb^{2+} and I^-/Br^- of the perovskite. It favors the reduction of electron trap and hole state densities of the CsMAFA film after modification with STS. The charge recombination suppression and the perovskite valence band increase, facilitating hole extraction and improving device response by reducing hysteresis.

2.5 ELECTRON TRANSPORT LAYER (ETL)

Good preparation of the electron transport layer is crucial to obtaining an efficient device. In addition to the proper alignment of the LUMO orbital level with the active layer, it must have a good interface with the perovskite and the conductive transparent electrode to efficiently transport the negative charges and connect the circuit properly. In addition, it is interesting that the ETL has an electron-blocking property by presenting a higher bandgap and generating more negative HOMO orbital levels, which blocks the transport of holes towards the cathode. In this way, efficient ETL layers present high electron affinity with good electron extraction capacity, favoring the dissociation of excitons and the optimized collection of negative charge carriers, reducing the recombination processes. YOU *et al.* (2020) employed an optimized 7 nm layer of WO_3 above the TiO_2 layer in $MAPbI_3$ solar cells. The results demonstrated the improvement of up to 20.14% of PCE in the backward curve, which is much better than the single WO_3-based device with 17.04% or TiO_2 with 16.99% as ETL. It is because of the hole blocking effect due to the thin layer of tungsten oxide, which increased the short-circuit current density(J_{sc}), related to the current density at zero voltage, and the fill factor (FF).

In addition to the high electron mobility, the ETL layer must have excellent transmittance in solar radiation in the conventional architecture for perovskite solar cells. That guarantees the maximum incidence and absorption of photons by the active layer, allowing a greater photocurrent and minimizing energy losses through the optical path. The processing ease of this layer must also be guaranteed to generate stable films efficiently (MOHAMAD NOH *et al.*, 2018).

Currently, several studies are trying to implement different types of electron carrier layers in perovskite solar cells. Concerning the conventional architecture, the most used materials are normally metal oxides, including TiO_2, ZnO, SnO_2, Al_2O_3, Nb_2O_5, Zn_2SnO_4, and WO_3 (JIANG; ZHANG; YOU, 2018; SHAHIDUZZAMAN *et al.*, 2020).

Graphene is also a material with excellent electrical and electronic properties in theory. However, in practice, its properties drastically depend on the preparation method. That encourages many researchers to work on inserting graphene into solar cells, especially high-efficiency and promising ones such as perovskite (FERGUSON; SILVA; ZHANG, 2019).

2.5.1 TiO_2 as electron transport layer (ETL) in perovskite solar cells (PSC)

Titanium dioxide is a semiconductor with good transparency, low toxicity, corrosion resistance, good photostability, a high bandgap of approximately 3.2 eV, and a high refractive index of around 2.7 (KE *et al.*, 2014). Due to its excellent properties, TiO_2 is the material for ETL most used in highly efficient PSCs due to its adequate conduction band, diversity of possible methods for deposition, chemical stability, and low cost (WANG, Yongling *et al.*, 2019). This oxide has mainly three polymorphs: anatase and rutile, which have a tetragonal structure, and brukite, with an orthorhombic unit cell. Rutile is the most stable crystalline phase and can be converted from anatase by heat treatment between 600 °C and 1200 °C (RUIZ *et al.*, 2003). In general, after film deposition, the TiO_2-based ETL are sintered at temperatures between 300 °C and 500 °C to ensure greater electron acceptor properties, transparency, and optical-electronic activity compatible with solar cells due to the predominance of the anatase polymorph (PROCHOWICZ *et al.*, 2020). For application in solar cells, the polymorph brukite is the least studied among the three because it is the most difficult phase to be synthesized, with little applicability in this area due to the lack of desired properties for device production and high production cost.

The preparation of layers of titanium oxides can be through the use of different precursors, such as titanium tetraisopropoxide, titanium tetrachloride, tetrabutyl titanate, titanium diisopropoxide bis(acetylacetonate), colloidal dispersion of nanoparticles, or commercial pastes (KESKIN et al., 2020; KHAN et al., 2019; YANG et al., 2021). The most used techniques for deposition are spray pyrolysis, spin coating, spray coating, blade coating, slot die, and inkjet printing (BUFFIERE *et al.*, 2020; KUMAR; AFTAB; AHMAD, 2020; YANG, Zifan *et al.*, 2021). In addition, studies using TiO_2 attempt to use mesoscopic ETL layer technology with a compact layer followed by a mesoporous layer. It tends to improve the interface of the ETL with the conductive transparent electrode, favored by the smooth and compact layer. At the same time, it improves the interface between the titanium dioxide and the active layer by generating greater roughness, which increases adhesion and surface area and improves the interface while optimizing electron collection (LEE, Junyeong *et al.*, 2022).

However, the widely used TiO_2-anatase as ETL exhibits poor electronic mobility and has many problems in charge separation at the interface between the ETL and the active layer (TAVAKOLI; YADAV; *et al.*, 2018). That makes further PSC enhancement difficult. The doping of TiO_2-anatase with inorganic elements such as Y, Al, Mg, Li, Nb, Ru, Zr and passivation of its surface using reduced graphene oxide and PCBM have been widely studied strategies (KIM *et al.*, 2018). In addition, the works that aim to improve the devices' efficiency and stability simultaneously attempt to reduce the sintering temperature of this layer. It is to reduce energy-related costs and apply these ETLs in combination with other materials that degrade at high temperatures or adapt to flexible devices that use polymeric substrates.

2.5.2 Graphene in solar cells

Graphene is a two-dimensional carbon allotrope with the configuration of a nanosheet that has alternating double bonds, with a hexagonal arrangement of carbon atoms bonded together with sp^2 hybridization. Depending on the quality of the graphene nanosheets, this material can present the electronic behavior of metal, semiconductor, or even an insulator. According to the graphene production route, materials with carbon atom vacancies, functional groups, preferred orientations in the lattice, roughness, folds, and different sheet dimensions and layer overlap can be obtained, drastically altering their properties (LIU, Lili *et al.*, 2015). That is explained by the defects and overlap of other layers, tending to distort the electronic and band distribution properties of this material (CASTRO NETO *et al.*, 2009; OOSTINGA *et al.*, 2008). Figure 10 shows the 3D and 2D diagrams of the distribution of graphene bands and their influences from the superposition of another layer or even an electric field.

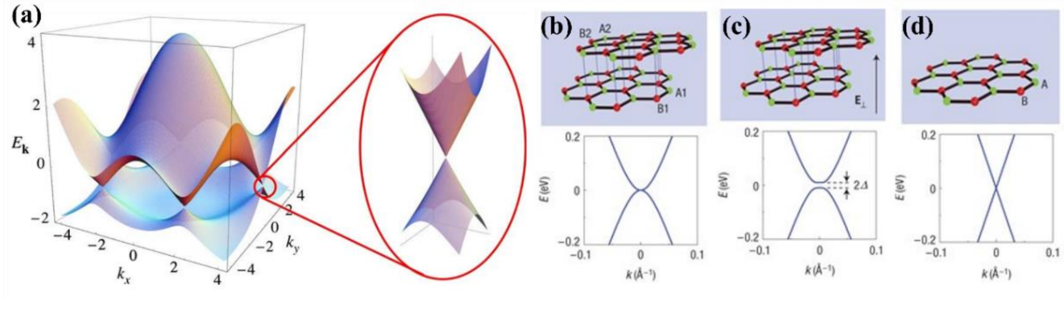

Figure 10: Electronic dispersion in the honeycomb lattice of graphene with the separation of valence and conduction bands due to the presence of defects (a); schematic band diagrams in 2D of bilayer network structure (b), bilayer under the influence of an electric field (c) and monolayer graphene (d).

Source: Adapted from CASTRO NETO *et al.* (2009); OOSTINGA *et al.* (2008).

Graphene can be obtained by different routes, bottom-up or top-down. The most well-known methodologies are chemical vapor deposition (CVD) and liquid phase exfoliation with the aid of surfactants, and the most common is the chemical exfoliation of graphite. Although this allotrope of carbon is, in theory, a monolayer consisting of only carbon, in practice, graphene is considered as structures obtained from graphite with stacking up to 30 sheets or sheet thicknesses up to 10 nm as the so-called graphene nanoplatelets. WANG, Shao Pei, GUO, and ZHOU (2013) highlighted that minor changes in the perfection of the lattice alter the band distributions, and even the angle of rotation between the blades attenuates the electronic properties of this material. In addition, commercial graphenes have a wide lateral size distribution and a wide variety of impurities adhered to the nanolaminates due to difficult synthesis and purification.

Thus, in the literature, there are different classes of graphenes, and within these same groups, there is a great variety of properties due to method, raw material, or supplier. Such groups, better known as graphene materials (GRMs), are defined as 2D, flake, or sheet-shaped carbon forms. HUANG, Xingyi *et al.* (2020) described that the classes of GRMs may include: few-layer graphene (FLG), graphene flake (GF), graphene nanoplatelet (GNP, GnP), graphene nanoflake (GNF), graphene nanoribbon (GNR), multi-layered graphene (MLG), reduced graphene oxide (rGO, RGO), graphene oxide (GO), and single-layered graphene (SLG). On the other hand, its three-dimensional (3D) arrangements, such as aerogels and foams from these 2D carbon materials, are also considered graphene scaffolding. The other 2D carbon materials, such as expanded graphite (EG), exfoliated graphite (ExG), graphite micro-particle (GMP), and natural flake graphite (NFG), are not considered graphene materials owing to the high number of stacked layers. In addition, as the number of overlapping layers increases, a drastic property reduction can be observed. Yet, graphitic materials still have excellent, even superior in some cases, properties compared to many metal oxides and conductive nanoparticles.

In theory, it is considered the best electrical and thermal conductor (>5000 W/mK) with charge mobility (HUANG, Xingyi *et al.*, 2020). BOLOTIN *et al.* (2008) reported that a carrier mobility value exceeding 2×10^5 cm^2 V^{-1} s^{-1} was measured at a carrier density of $\approx2\times10^{11}$ cm^{-2} in suspended, single-layer graphene. A much higher mobility value over 10^7 cm^2 V^{-1} s^{-1} has been realized in a graphene layer on a graphite substrate with an ultralow carrier density ($n\approx3\times10^9$ cm^{-2}). Due to its optical transparency (having only 2.3% of the energy absorbed when light passes through it), its excellent mechanical properties (hardness of 13.09 GPa and Young's modulus of 162.96 GPa), flexibility and elastic recovery of 75.27%, and great electrical and electronic characteristics, graphene has been applied in solar cells to improve the efficiency of devices (JIN, Huile *et al.* 2018). In the literature, it is reported that Young's modulus and intrinsic strength show a wide range of distributions of 6–42 GPa and 76–293 MPa for GO stacked layer and 250±150 GPa and 30–50 GPa for GO monolayer (HUANG, Xiao Ming *et al*., 2020; LIU, Lizhao *et al*., 2012). Such a wide range of properties is a consequence of the great variety of different nanosheets in the same set of samples, even being a structure with high-density deliberate defects such as the oxygen groups. JIN, Jeong Un *et al.* (2019) also reported that graphene improves the gas barrier property, drastically reducing the permeation of molecules that can accelerate the degradation of the devices.

This carbon allotrope has been applied in solar cells based on the use of reduced graphene oxide (rGO) or graphene oxide (GO) prepared from the chemical exfoliation of graphite. As mentioned, the properties of graphene are directly related to its quality and the route of obtaining it, which makes it difficult to correlate the works and provides a very large discrepancy in the published results. Owing to the diversity of properties on account of the quality of the material, graphene has been implemented in the field of solar cells in several layers. Its application as a transparent conductive electrode attempts to take advantage of the high electrical conductivity, mechanical strength, and flexibility of the films, maintaining the optical transparency almost completely, thus being a candidate to replace the ITO.

Other works have shown that graphene can also be applied both in the carrier layer for holes or electrons and in the active layer to improve the efficiency of devices. Generally, these works do not present the levels of valence and conduction bands when exhibiting semiconductor properties or the work function when exhibiting metal property at a point of coincidence between the electronic bands known as the Dirac point (LUCEÑO-SÁNCHEZ; DÍEZ-PASCUAL; CAPILLA, 2019).

KUSUMA *et al.* (2018) produced a composite of graphene nanoribbons (GNR) with TiO_2 as the electron carrier layer for CdS/ZnS-based quantum dot sensitized solar cells (QDSSC). GNR was synthesized from the breakdown of the structure of multi-walled carbon nanotubes (MWCNT) by the oxidation process. The devices with graphene nanoribbons and TiO_2 presented PCE of 3.69% ± 0.16%, while with the compact TiO_2, they resulted in only 1.74% ± 0.05%. The device with graphene oxide as ETL prepared from graphite exhibited an energy conversion efficiency of 2.16% ± 0.12%, while with the ETL of TiO_2-MWCNT, the PCE was 1.99% ± 0.21 %. The authors concluded that the morphology of graphene, when mixed with TiO_2, changes its dispersion, which leads to a better transport of charges. In addition, nanoribbons create a preferential path for electrons in a more targeted manner when compared to nanosheets, which have a larger lateral size. In addition, the layer's electrical resistance was lower with 0.12% of GNR, considered the optimal concentration according to their study of the variation of charge contents. In the same work by Kusuma *et al*. (2018), it was reported that GNR with TiO_2 is also considered an excellent candidate for the ETL layer for OPV devices due to its high electrical conductivity.

The reduction process of oxidized graphene originates materials with different properties depending on the reagents used and the mechanism of action to remove the oxygenated groups from the nanosheets. Although they reduce the probability of contamination of the final material, thermal reduction methods tend to produce a graphene structure with many vacancies or even distortions in the hexagonal network that favor the reduction of electrical conductivity (KAKAVELAKIS *et al.,* 2017; MARTÍN-GARCÍA *et al.*, 2018). The rGO structure also, during the reduction process, can favor the recrystallization and re-stacking of nanoblades, mainly by processes that use a powder at high temperatures.

JOKAR *et al.* (2018) prepared planar heterojunction perovskite ($MAPbI_3$:PCBM) devices with inverted architecture and evaluated the type of graphene to apply as a hole extractor layer. The rGO samples were prepared with three different reducing agents: hydrazine (rGO-NH), sodium borohydride (rGO-BH), and 4-hydrazino benzenesulfonic acid (rGO-HBS), with rGO-NH and rGO-HBS capable of achieving the best PCE devices of 16.0% and 16.4%, respectively, in the JV forward curve, excellent stability, and reproducibility. Furthermore, these materials outperformed the device with GO (PCE 13.8%) and even the PEDOT:PSS, a reference layer with 14.8% of PCE. Finally, the flexible device demonstrated excellent results in maintaining 70% initial performance after 150 flexes cycles.

2.5.3 Tin dioxide (SnO_2) as electron transport layer (ETL) in perovskite solar cells (PSC)

The low heat treatment temperature for preparing this layer is a huge advantage compared to titanium dioxide films. Furthermore, SnO_2 nanoparticles show excellent band alignment with perovskite and may even have superior charge extraction capability. This set of properties combined with easy processing has dramatically helped to improve the efficiency of flexible devices, a huge improvement over TiO_2 ETLs. Although this tin dioxide layer has made many advances possible, its devices have a lot to improve, especially regarding some key problems that must be solved, mainly to reach solar cells with PCE above 20% (CHUNG *et al.*, 2020).

SONG *et al.* (2019) stated that the low crystallinity and surface defects of SnO_2 due to low-temperature processing induce a short diffusion length of charge carriers, despite the higher electron mobility. It reduces the property of collecting electrons because the distance covered is limited even if they can move at greater speed. Thus, the optimized thickness value is approximately 30 nanometers. This layer's thickness is smaller than other materials used as ETL, even compared with the TiO_2 which is commonly used until 200nm. On the other hand, such optimization manages to circumvent the leakage current problem and still presents an efficient hole blocking. A very interesting advantage due to the low thickness is the improvement of transmittance, enhancing the greater collection of photons by the active layer. Therefore, it is very important to control the deposition of this layer, requiring a uniform film with a thickness close to the optimized one.

YI, Haimang *et al.* (2018) found that vice performance is altered depending on the type of SnO2 precursor. Thus, three types of SnO_2-based layers were studied. The first was the preparation of the film by spin coating deposition of the compact layer (S-SnO_2) from the sol-gel solution precursor, SnO_2 52.59 mg of Tin (IV) chloride pentahydrate ($SnCl_4.5H_2O$) into 1 ml isopropanol. The second method was depositing the mesoporous layer (N-SnO_2), diluting the colloidal dispersion of nanoparticles manufactured by Alfa Aesar by 1% in water. Finally, the SnO_2 bilayer (B-SnO_2) was prepared following ITO/S-SnO_2/N-SnO_2/$MAPbI_3$/Spiro-OMeTAD/Ag architecture. In the backward direction, the S-SnO_2 showed 12.97 ±1.16% PCE obtained from the JV curve, with a maximum of 14.7%. The devices with N-SnO_2 obtained 14.05 ± 1.08% with 15.66% record efficiency. On the other hand, combining these films in the bilayer architecture increased power conversion efficiency to 16.84 ± 0.53, and the record was 17.61%.

The combination of compact and mesoporous layers is already a technology widely used in TiO_2 ETLs or passivation mechanisms. The compact contact of the ETL with the transparent conductive electrode makes the conduction of charges more efficient. At the same time, the mesoporous interface with the active layer tends to increase the surface area and roughness, improve the adhesion, and, consequently, the extraction of electrons. However, as the application of SnO_2 as an ETL layer in solar cells is more recent than other materials, few works still explore variations in the combination of materials with tin dioxide or its architecture.

3. OBJECTIVES AND PROPOSAL OF WORK

The general objective of the present work is to manufacture and evaluate the efficiency of CsMAFA multi-cation perovskite solar modules as a function of the variation of the electron transport layer based on tin dioxide with different graphenes and titanium dioxide nanoparticles. As specific objectives can be highlighted:

- Preparation of control devices compatible with power conversion efficiency presented in the literature;
- Evaluation of the influence of different tin dioxide precursors on the electron transport layer;
- Evaluation of surface modification in tin dioxide with KCl as a hysteresis reduction strategy;
- Preparation and performance evaluation of SnO_2 nanoparticles in colloidal suspension as ETL;
- Preparation and performance evaluation of tin dioxide ETL layers with GNP at different concentrations, in addition to identifying the most promising proportion;
- Preparation and performance evaluation of mixing SnO_2 from colloidal suspension with GNP at different concentrations, in addition to its comparison with the precursor of $SnCl_4.5H_2O$. Based on this test, I could verify if graphene interferes with the formation of SnO_2 in relation to the SnO_2 (IPA);
- Preparation and performance evaluation of double layer ETL based on SnO_2 films with GNP;
- Avaluation of the influence in the order of deposited ETL layers on the performance of double layers devices. This could help to understand whether the greater interference of GNP in electron transport is mainly related to the interface with FTO or with perovskite;
- Substantiation of the influence of different concentrations of GNP on the double layer;

- Device manufacturing with different types of graphene in different concentrations to verify the influence of the interaction of chemical groups in the SnO_2 matrix;
- Device manufacturing with titanium dioxide anatase in the best concentrations observed in the experiments with graphene;
- Examination of the influence of all modifications on the photovoltaic properties of the device, such as J_{sc}, V_{oc}, FF, PCE, hysteresis, and real PCE, which is the average of backward and forward measurements.
- Finally, identification of the most promising modifications for optimizing perovskite devices.

3.1 METHODOLOGY

3.1.1 Materials

Reagents:

- **2,2′,7,7′-tetrakis(N,N-di-p-methoxyphenyl-amine)9,9′-spirobifluorene (Spiro-OMeTAD) –** Xi'an Polymer Light Technology Corp.
- **4-terc-butylpyridine (tBP; 98%)** – Sigma-Aldrich.
- **Acetonitrile anhydrous (ACN)** – Sigma-Aldrich.
- **Cesium iodide (CsI, 99.9 %)** – Tokyo Chemical Industry (TCI) America, Inc.
- **Chlorobenzene (CB)** – Sigma-Aldrich.
- **Dimethyl formamide anhydrous (DMF)** – Sigma-Aldrich.
- **Dimethyl sulfoxide anhydrous (DMSO)** – Sigma-Aldrich.
- **Fluorine-doped tin dioxide (FTO)-coated glasses substrates (TEC7 – 300 mm x 300 mm x 2.2 mm)** – GreatCell Solar Materials LTD.
- **Formamidinium iodide (FAI)** – GreatCell Solar Materials LTD.
- **Graphite in Flakes -** Natural graphite flakes were supplied by Nacional de Grafite Ltda, Brazil, with an average particle size of around 150 nm and carbon between 87 and 99% (Graflake 99550).
- **Hydrogen Peroxide 50% -** Vetec Química Fina Ltda.
- **Isopropanol (IPA)** – Sigma-Aldrich.

- **Isopropyl alcohol (IPA, anhydrous, 99.5%) -** Sigma Aldrich.
- **Lead bromide (PbBr2, >98%)** – Tokyo Chemical Industry (TCI) America, Inc.
- **Lead iodide (PbI2, 99.99%)** – Tokyo Chemical Industry (TCI) America, Inc.
- **Lithium bis(trifluoromethanesulfonyl)imide (LiTFSI; 99.95%)** – Sigma-Aldrich.
- **Methylammonium bromide (MABr)** – GreatCell Solar Materials LTD.
- **Methylammonium iodide (MAI)** – GreatCell Solar Materials LTD.
- **Nitric Acid P.A. –** Vetec Química Fina Ltda.
- **Sodium Nitrate** – Vetec Química Fina Ltda.
- **Sulfuric Acid P.A. –** Vetec Química Fina Ltda.
- **Tin (IV) Chloride Pentahydrate ($SnCl_4.5H_2O$)** – Sigma-Aldrich, (CAS 244678-100G).
- **Tris(2-(1H-pyrazol-1-yl)-4-tert-butylpyridine)cobalt(III)tri [bis(trifluoromethane)sulfonimide] (FK209 Co(III) TFSI)** – GreatCell Solar Materials LTD.

Nanoparticles:

- **Tin(IV) oxide, 15% in H_2O colloidal dispersion (SnO_2 (H_2O)):** Alpha Aeser, batch M21H020, density of 1.153 and molecular weight 150.69 g/mol (CAS 18282-10-5).
- **Few layers graphene (FLG):** up to 5-layer, 3-layer centered graphene with an average size of 120 nm. Composition of 54.8% of a non-ionic surfactant and 39.2% of graphene. This material was provided by MG graphene
- **Graphene nanoplatelets (GNP):** 6-8 nm thick graphene nanoplatelets from Strem Chemicals INC (CAS 1034343-98-0).
- Titanium Dioxide anatase (TiO_2): provided by MKNano, MKN-TiO2 A050 – Anatase titanium dioxide Nanopowder, with 50 nm spherical particles, 98% purity, pure, APS, and lot #D0711.
- **Graphene oxide (GO):** obtained from chemical and physical exfoliation by the improved Hummers method proposed by TIENNE *et al.* (2022)

from natural graphite flakes supplied by Nacional de Grafite Ltda, Brazil, with an average particle size of around 150 mm and carbon contents between 87 and 99% (Graflake 99550). This structure has approximately 30–60 µm lateral size and thickness lower than 40 nm and <20 layers stacked. The residue of GO at 700 °C by TGA in N_2 flow is about 63.2% related to the carbon compound. The rest is mainly related to oxygenated groups such as epoxy, hydroxyl, carbonyl, and carboxylic acid.

- **Reduced graphene oxide (rGO):** obtained by the thermal reduction of GO in a muffle furnace at 1000 °C for 2 min followed by ultrasonication for 24 h in 70% ethanol at a concentration of 50 mg/ml. This structure has approximately 10–50 µm lateral size and approximately 4-20 layers stacked. The composition of this material is 93.9 ± 0.6 % carbon, also calculated by TGA.

3.1.2 Methods

First, it is worth mentioning that two types of SnO_2 base material were used:

I. precursor from $SnCl_4.5H_2O$ dispersed in isopropanol (IPA) which generates the SnO_2 film due to exposure to the atmosphere at temperature concomitant to the preparation of the ETL, which was assigned as SnO_2 (IPA);

II. commercial colloidal dispersion of SnO_2 nanoparticles in water was assigned as SnO_2 (H_2O).

Thus, solutions were prepared according to the type of precursor with the type of modification implemented and the type of graphene or titanium dioxide in different proportions. The present work was divided into 5 groups schematized in a didactic way presenting all types of evaluated ETL layers (Figure 11).

Group 1 is related to preparing the most common ETL layers in the literature with pure tin dioxide composition using different methods, with SnO_2 (IPA) being the most widely used. However, there is great variation in the concentration of its precursor solution. The present work used the standard concentration for this precursor of 0.05 M, representing the proportion of 17.53 mg/ml of solvent. Double this concentration was also tested, implying a thicker layer, assigned with the code of SnO_2 (IPA) 0.1M. The $SnCl_4.5H_2O$ precursor usually has a great hysteresis problem. Thus, the literature evaluated surface modification with KCl as a passivating effect. Finally, the control without the ETL and the layer from the nanoparticles in water, with code SnO_2 (H_2O).

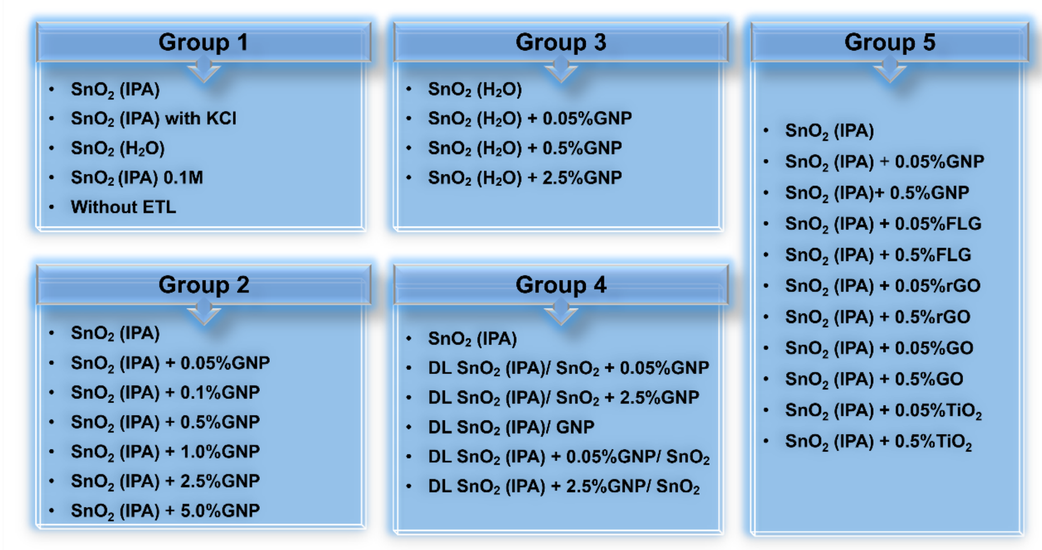

Figure 11: Scheme of the types of ETL tested as perovskite devices according to composition and chemical modification, with the acronym DL referring to the samples that were prepared in the double layers, and the slash ("/") is the separator to differentiate the composition of each layer.

Source: Prepared by the author.

Group 2 is related to preparing tin dioxide mixtures with graphene nanoplatelets. The precursor used in this group is SnO_2 (IPA), combined with the most common commercial graphene type (GNP) in different proportions. A graphene concentration scan was performed from 0.05% to 5.0%, and it is worth noting that the concentration of the solution was set at 17.54 mg/ml. In the initial tests, SnO_2 (IPA) mixtures with 10%, 25%, 50%, 75%, and 90% of GNP were also performed, but all devices had short circuit problems or lack of contact, making such compositions unfeasible.

Group 3 was carried out to prepare the SnO_2 (H_2O) mixture with 0.05%, 0.5%, and 2.5% of GNP. Dilution was carried out in a 1:3 ratio of commercial colloidal solution in water. The graphene concentration was corrected based on the mass of SnO_2 present in the standard dilution.

In Group 4, the double layer (DL) experiment was carried out with a compact film and the other with a mixture of GNP with SnO_2 (IPA), as exemplified in Figure 11, with the forward-slash (“/”) separating the first and second films. The variation in this set was related to the order of deposition of the compact layer and the mixture with graphene according to the glass/FTO/ETL1/ETL2/Perovskite/HTL/Au architecture. It was also performed in the compositions of 0.05% and 2.5% of GNP, as well as the deposition of 100% of GNP above the compact layer of SnO_2. Finally, Group 5 was prepared based on the optimized concentrations with different types of graphene and titanium dioxide nanoparticles.

3.1.3 Synthesis of graphene oxide (GO) and reduced graphene oxide (rGO)

5 g of graphite from Nacional de Grafite 99550 with average particle size (+50 mesh) were used. The graphite flakes were transferred to a 1 L Erlenmeyer flask with 4.5 g of sodium nitrite ($NaNO_2$) and 169 ml of sulfuric acid (H_2SO_4) under magnetic stirring for 3 h in an ice bath, initiating the step of graphite interleaving. The oxidation process started with the slow addition of 22.5 g of potassium permanganate (over 2 h) to the Erlenmeyer containing the reagents in the intercalation step. After this period, the ice bath was removed, and stirring was continued for 7 days. Then, the exfoliation step began, with the dripping of 605 ml of 5% H_2SO_4 for 3 h with magnetic stirring. Subsequently, the viscous solution was washed with a solution of 3% H_2SO_4 and 0.5% H_2O_2 (15.8 ml of H_2SO_4, 7.8 ml of H_2O_2, and 476.4 ml of distilled water) with magnetic stirring for 12 h. Twelve washes were performed with a solution of 3% H_2SO_4 and 0.5% H_2O_2 using a centrifuge. Then, the material was centrifuged and washed with distilled water until pH 7. This process generated oxidized graphite. Then, the material was dried in an oven at 100°C until constant mass, resuspended in an Erlenmeyer flask with 70% ethanol with the proportion of 50 mg/ml, and placed in an ultrasound bath for 24 h in order to exfoliate oxidized graphite to obtain oxidized graphene (GO). Finally, the GO was thermally reduced in a muffle furnace at 1000°C for 2 min. Then, another step of exfoliation with 70% ethanol in the proportion of 1.0% nanoparticle to solvent in ultrasound was performed for 3 h to ensure maximum delamination. Finally, the material was dried in an oven at 100 °C until constant mass, obtaining the rGO (TIENNE *et al.*, 2022).

3.1.4 Sample preparation

As already mentioned, there are two types of precursors: SnO_2 (IPA) and SnO_2 (H_2O). The samples were prepared from the dilution of standard solutions to reduce the error related to mass weighing less than 1mg, mainly for the compositions with low nanoparticle contents. Thus, when preparing larger volume dispersions, larger masses are weighed, and due to the use of calibrated micropipettes, greater precision in sample preparation is achieved. The concentration of the mixtures with SnO_2 (IPA) was fixed with a molarity of 0.05 M of $SnCl_4.5H_2O$, 17.54 mg/ml. Even so, the prepared solutions had a volume of 1 ml fixed to avoid the effects of variations of favoring density. Thus, two standard solutions of $SnCl_4.5H_2O$ were prepared at concentrations of 110 mg/ml, called S, and 5.8 mg/10ml (0.58 mg/ml, called S2). As for graphene and TiO_2 nanoparticles, standard solutions were prepared at a concentration of 1mg/ml. Table 1 shows the dilutions performed with a volume of approximately 1ml.

Table 1: Procedure for preparing the dilutions with S1 and S2 solutions of $SnCl_4.5H_2O$.

Nanoparticle content	**Nanoparticles' solution (1mg/ml)**	**S1 (110mg/ml)**	**S2 (0,58mg/ml)**	**IPA**
5.0%	850 µL	150 µL	-	-
2.5%	425 µL	150 µL	128 µL	296 µL
1.0%	170 µL	150 µL	566 µL	114 µL
0.5%	85 µL	150 µL	711 µL	53.6 µL
0.1%	17 µL	150 µL	828 µL	5 µL
0.05%	8,5 µL	150 µL	843 µL	-

Source: Prepared by the author.

The SnO_2 (H_2O) solutions were made from a 1:3 dilution of the commercial colloidal solution to deionized water. For 250 µL of the commercial solution, 750 µL of deionized water was added. Thus, as the commercial solution contains 15% nanoparticles, it was carried out following this calculus:

- in 250 µL, SnO_2 colloidal dispersion has 15% of SnO_2;
- so, it has 37.5 µL of SnO_2 (250 x 0.15);
- as the density of the solution is 1.153 g/ml, there is 43.24 mg of SnO_2 (37.5 x 1.153);

Therefore, the concentration of the solution to be prepared with a 1:3 dilution is 43.24 mg/ml. To incorporate graphene, a standard solution of GNP was prepared at a concentration of 1.44 mg/ml. Then, the mixtures were performed according to the procedure shown in Table 2.

Table 2: Procedure adopted to prepare the dilutions of SnO_2 (H_2O) samples with GNP.

GNP content (w/w)	**GNP's solution (1,44 mg/ml)**	**Commercial SnO_2 solution**	**Deionized water**
2.5%	750 µL	250 µL	-
0.5%	150 µL	250 µL	600 µL
0.05%	15 µL	250 µL	735 µL

Source: Prepared by the author.

Finally, all solutions were dispersed for at least 5 h in an ultrasound bath before deposition of the ETL films. In Figure 12 are photos of the prepared solutions.

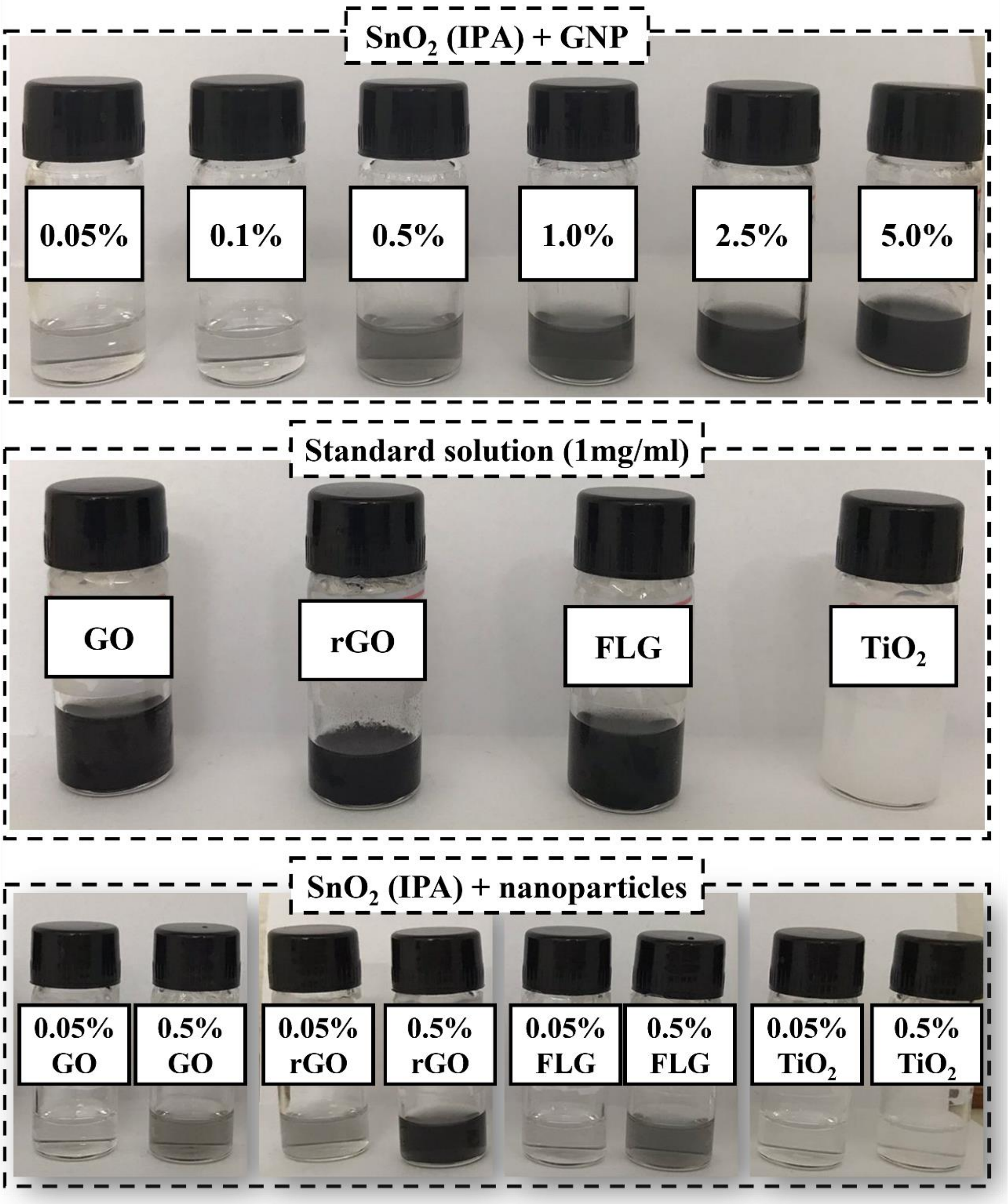

Figure 12: Photo of the main solutions prepared.

Source: Prepared by the author.

3.2 DEVICE PREPARATION

The preparation of the device was carried out at the Laboratório Nanotecnologia e Energia Solar (LNES) at the chemistry institute of the Universidade Estadual de Campinas (UNICAMP). The experimental procedure was divided into five steps that will be explained in detail in topics 3.2.1 to 3.2.5, as summarized below:

- Substrate preparation: cleaning, cutting of FTO-coated glass, etching;

- ETL deposition: preparation of solutions according to the proposed variation, deposition by spin coating followed by heat treatment;
- Perovskite deposition: preparation of the CsMAFA solution, deposition by spin coating followed by heat treatment;
- HTL deposition: preparation of the Spiro-MeOTAD solution and its dopants, deposition by spin coating, conditioning under low humidity and without light and contact cleaning;
- Metal electrode evaporation: evaporation of 70 nm of gold (Au) by thermal evaporation with a mask for the device.

3.2.1 Substrate preparation

First, the commercial 30x30 cm glass/FTO plate was cut to 97x91 mm dimensions using a cutter pen. Then, with the aid of a mask, the area of the 24x15 mm substrate was marked with a glass cutting pen. It is worth mentioning that all markings with the glass cutting pen are carried out on the glass side, opposite the FTO layer, as the pen destroys the conductive coating and can generate defects in the functional area due to the propagation of cracks. The conductive side check was performed using a multimeter. Another way to check which side of the glass is with the FTO is by evaluating the surface roughness, with the roughest side being the one covered with the conductive layer of FTO and the glass being the smoothest side. Each device will be constructed from individual 24x15 mm substrates. The etching step can be performed individually on each 24x15 mm piece or the 97x91 mm set with previously made cut marks.

With the aid of Kapton® tape, the area of the FTO that will be preserved was protected (conductive side of the substrate), leaving 2 mm of the smaller size of the substrate (related to the 15 mm) exposed. The etching process removes FTO from the exposed region. That is done to control the device's active area and prevent a short circuit in the edge region. For this chemical attack, a paste of metallic zinc in water, with no defined concentration, was placed on the exposed part of the FTO. The paste must be prepared so that it is not too liquid but has enough fluidity to cover the desired area adequately. This step can also be performed with zinc powder directly on the desired area, but it is difficult to get the zinc to spread properly by adhering to the entire surface when it is powdered. Then wait for the water to evaporate from the slurry. The elimination of water is observed by whitening the covered area and presenting the appearance of a dry solid. When the region covered with the paste is dry, a 4 M solution of HCl is dripped. It is possible to observe the bubbling of the reaction of the HCl with the metallic zinc and even a small release of white smoke. It should be dripped little by little as the region of the paste releasing from the substrate is observed. When noticing that the entire FTO's film has come off the substrate, slowly blast the HCl solution with a plastic pipette to remove the film. Then, the substrate was washed with a jet of deionized water, removing residues of the paste and still removing excess acid from the surface. Figure 13 shows the main steps of the etching process as described above.

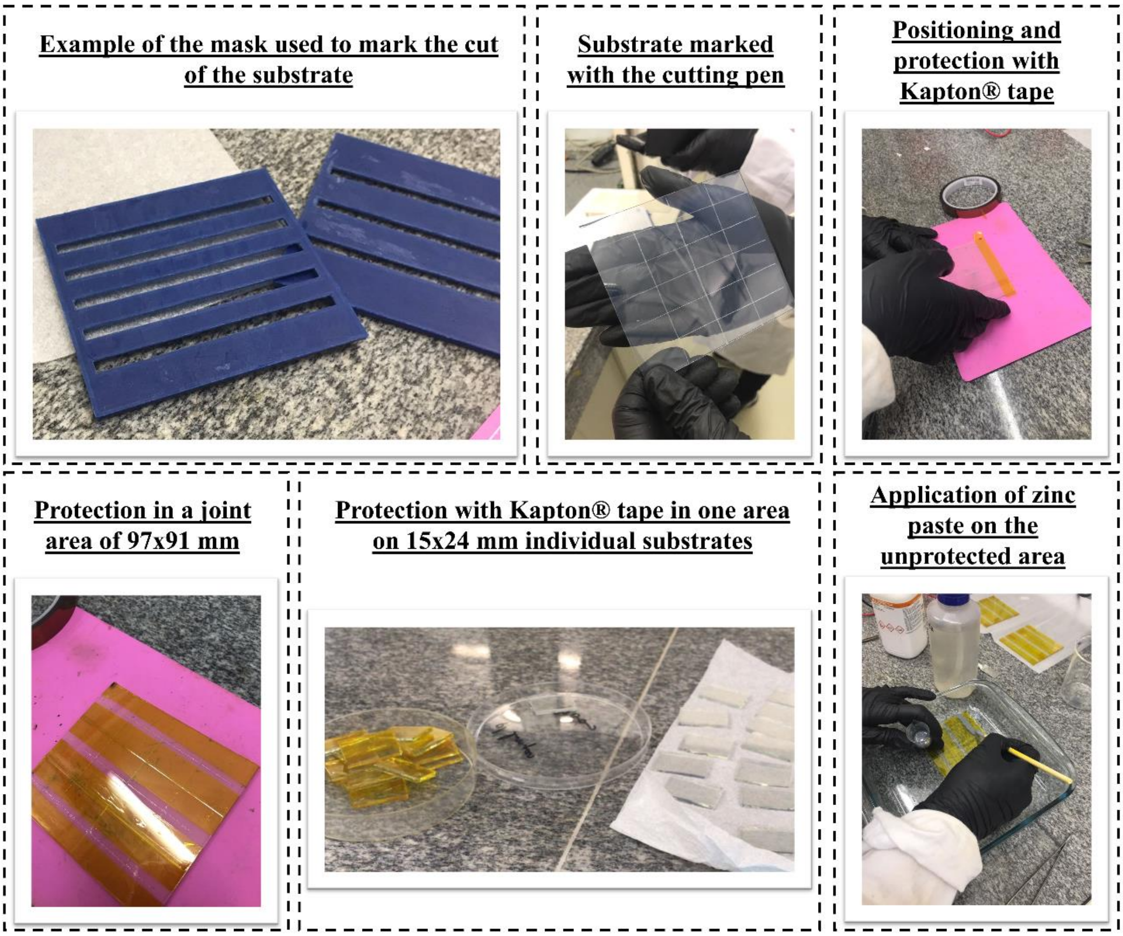

Figure 13: Photos of the main steps of the etching process.

Source: Prepared by the author.

After the etching process, the substrates (15x24 mm) were cut from the markings and cleaned. First, a soft bristle brush with Hellmanex diluted at 2% was used to scrub the substrate on both sides. Then, the substrate was cleaned by an ultrasonic bath in 4 steps:

1) Hellmanex® solution diluted in 2% water for 15 min at 40°C;
2) warm deionized water for 5 min;
3) IPA for 15 min;

4) warm deionized water for 15 min.

Finally, the substrates were immediately dried with compressed air to avoid the deposition of unwanted impurities and stains that could interfere with the device's performance. It is worth mentioning that the substrates remained submerged in warm water until they were dried directly by compressed air. Then the substrates were treated for 25 min in a UV ozone cleaner with a gentle airflow to remove organic residues and hydrophilize the surface. It is worth noting that the ETL should be placed above the substrate immediately after the ozone UV treatment to reduce the chance of contamination and loss of hydrophilicity.

3.2.2 ETL deposition

As described in section 3.1.4- Sample preparation, the ETL layers were deposited via spin coating in the static method. First, the solution is dripped, and then the equipment starts rotating. To carry out the deposition of the ETL layers, it is necessary to carry out protection on the opposite side of the etching of approximately 3 mm, as exemplified in Figure 14. That is because the contact cleaning, performed after the deposition of the HTL, is incapable of removing the oxide tin layer. It is also worth mentioning that for the double-layer samples, protection was carried out with scotch magic tape for each process, removing after spin coating and before annealing. The conditions can be described below according to the groups:

- for the SnO_2 (IPA): the deposition was carried out in static mode using 50 µL of the ETL solution and with the rotation speed of 3000 rpm for 36 s and a ramp of 1000 rpm.s^{-1}. Then, pre-drying is carried out at 100 °C for 5 min and then heat treated at 180 °C for 1 h. Finally, the sample was treated in UV ozone for 25 min to clean and hydrophilize the surface. The perovskite layer was deposited immediately after UV ozone treatment.
- for the sample treated with KCl: the deposition was carried out in static mode using 50 µL of pure SnO_2 (0.05m mol of $SnCl_4.5H_2O$ in isopropanol) with the rotation speed of 3000 rpm for 36 s and a ramp of 1000 rpm s^{-1}. Then, pre-drying is carried out at 100 °C for 5 min and then heat treated at 180 °C for 1 h. Finally, the sample was treated with UV ozone for 20 min to clean and hydrophilize the surface. Then, 50 µL of a 10 mM KCl solution are deposited in static mode with a rotation speed of 3000 rpm for 30 s and acceleration of 2000 rpm s^{-1}. Subsequently, the

treated substrate undergoes annealing at 100 °C for 10 min, followed by 25 min in UV ozone to clean and hydrophilize the surface. The perovskite layer was deposited immediately after UV ozone treatment.

- for SnO_2 (H_2O): the deposition was carried out in static mode using 100 µL of the diluted stock solution, according to topic 3.1.4- Sample preparation for the aqueous samples. The spin coating was configured for a rotation speed of 3000 rpm for 36 s and a ramp of 2000 rpm s^{-1}. Then, pre-drying is carried out at 100 °C for 5 min, heat treated at 180 °C for 1 h, and followed for 25 min in UV ozone. Finally, the sample was treated in UV ozone for 25 min to clean and hydrophilize the surface. The perovskite layer was deposited immediately after UV ozone treatment.
- for samples with double layer:
  - the first layer was performed in static mode using 50 µL of the ETL solution, a rotation speed of 3000 rpm for 36 s, and a ramp of 1000 rpm s^{-1}. Then, pre-drying is carried out at 100 °C for 5 min and then heat treated at 180 °C for 1 h.
  - the second layer was deposited after this process following the same procedure 50 µL of ETL solution rotation speed of 3000 rpm for 36 s and ramp of 1000 rpm s^{-1}. Then, pre-drying was carried out at 100 °C for 5 min and then heat treated at 180 °C for 1 h. Finally, the sample was treated in UV ozone for 25 min to clean and hydrophilize the surface. The perovskite layer was deposited immediately after UV ozone treatment.

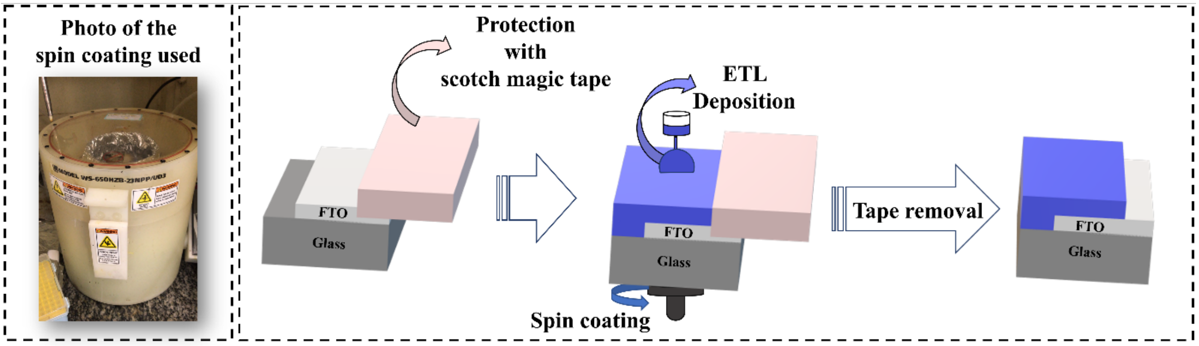

Figure 14: Scheme of ETL deposition by spin coating and protection with magic scotch tape.

Source: Prepared by the author.

3.2.3 Perovskite deposition

For the deposition of the CsMAFA perovskite layer, the following fresh solutions were first prepared inside the glovebox:

1) <u>Solution A:</u> 693.4 mg of (PbI_2 in 1 ml of a mixture of solvents DMF:DMSO (4:1) and homogenized with magnetic stirring at 180 °C for 10 min for complete solubilization and activation of the lead;
2) <u>Solution B:</u> 275 mg of $PbBr_2$ in 0.5 ml of a mixture of solvents DMF:DMSO (4:1) and homogenized with magnetic stirring at 180 °C for 10 min for complete solubilization and activation of the lead;
3) <u>Solution C:</u> 117 mg of CsI in 0.3 ml DMSO and homogenized with magnetic stirring at 150 °C for 10 min for complete solubilization;
4) <u>Solution D:</u> to prepare the $FAPbI_3$ solution, 213.4 mg of FAI was added to solution A (PbI_2) and remained under magnetic stirring at room temperature for 1 h; it is worth noting that the PbI_2 solution was sustained at room temperature before mixing so as not to compromise the organic component;
5) <u>Solution E:</u> to prepare the $MAPbBr_3$ solution, 71 mg of methylammonium bromide (MABr) was added to solution B ($PbBr_2$) and remained under magnetic stirring at room temperature for 1 h; the $PbBr_2$ solution was also kept at room temperature before mixing;
6) <u>CsMAFA solution:</u> 0.2 ml of solution E ($MAPbBr_3$) was added to 1 ml of solution D ($FAPbI_3$) under magnetic stirring for 2 min. Then, 64 μl of solution C (CsI) were added to this solution and kept under magnetic stirring at room temperature for 30 min. Likewise, all solutions were kept at room temperature.

CsMAFA films were deposited inside the glovebox in the spin coating in static mode combined with the chlorobenzene (CB) antisolvent precipitation method. For the depositions, the atmospheric conditions were kept below 2 ppm of H_2O and O_2, at a temperature between 22 and 27 °C. The vacuum purge remained activated during depositions and the next heat treatments. It is done so that the atmosphere does not saturate with the solvents used, which may compromise the quality of the perovskite films. The steps are described below:

1) Substrate/FTO/ETL samples after ozone treatment were placed on the spin coating support; the support vacuum suction was activated to hold the substrate and then gently cleaned with an N_2 jet to remove possible impurities on the surface;
2) 50 µl of the CsMAFA solution were deposited evenly above the ETL's sample to cover the surface completely;
3) spin coating was started at a speed of 1000 rpm with an acceleration of 200 rpm s^{-1} for 10 s;
4) then, the rotation was changed to 6000 rpm with acceleration from 2000 rpm s^{-1} for another 10 s;
5) after step 4, 200 µl of the chlorobenzene anti-solvent were gently blasted on the film under rotation of 6000 rpm, which was maintained for a further 10 s after the CB precipitation. It is worth noting that the steps from 3 to 6 were sequential and uninterrupted; the equipment was programmed in advance. The anti-solvent was used in a single jet, with a distance of approximately 2 cm from the substrate, with constant activation of the micropipette and a speed that was not too slow but also not capable of destroying the film;
6) finally, after the spin coating stopped spinning, the sample was transferred to a heating plate programmed at 100 °C, remaining for 30 min.

The annealing treatment was performed inside the glovebox, the sample was slowly cooled, and the HTL was deposited on top without surface treatment. Between these steps, samples were not taken from the glovebox and were performed one step immediately after the other to obtain high-efficiency devices. Figure 15 shows a summary scheme of the active layer deposition.

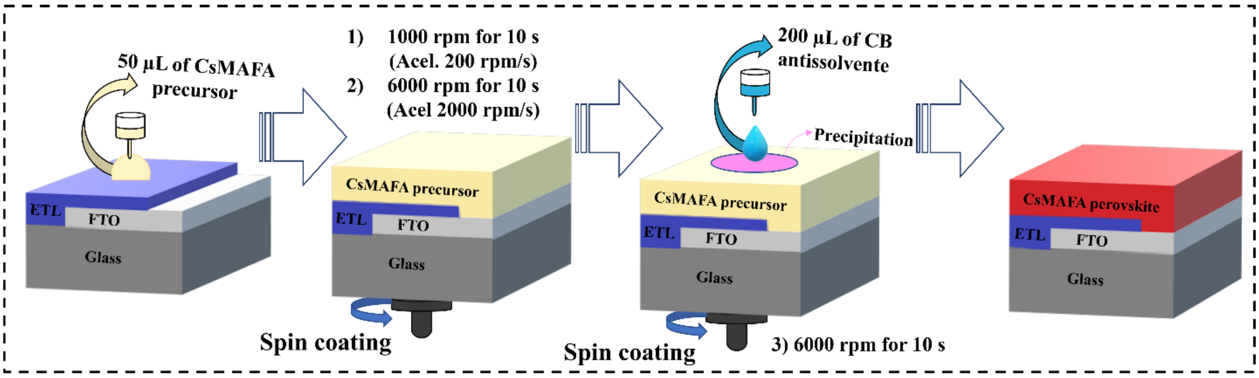

Figure 15: Scheme of perovskite layer deposition steps.

Source: Prepared by the author.

3.2.4 HTL deposition

The hole transport material, Spiro-OMeTAD, was doped and deposited over the perovskite by dynamic spin coating. The Spiro-OMeTAD solution is added while the device is already spinning. For the preparation of doped Spiro-OMeTAD, it was necessary to prepare its stock solutions:

- 4-tert-butylpyridine (TBP): commercial stock solution.
- lithium bis(trifluoromethanesulfonyl)imide (Li-TSFI): 1.8 M in acetonitrile. The recipe used: 64.6 mg in 125 µL of acetonitrile.
- tris(2-(1H-pyrazol-1-yl)-4-tert-butylpyridine)cobalt(III) bis(tri-fluoromethylsulphonyl)imide (FK209): 0.25M in acetonitrile. The recipe used was 18.8 mg in 50 µL of acetonitrile.

In the present work, the stock solutions were also prepared and used within a maximum period of 1 week. To prepare 20 devices, 99 mg of Spiro-OMeTAD in 987 ml of chlorobenzene were used. Then, 36 µL of TBP stock solution, 20 µL of Li-TSFI stock solution, and 8 µL of FK209 stock solution were added to the Spiro-OMeTAD solution. The solution was homogenized with a magnetic stirring for 2 min between adding one component and another. Spiro-OMeTAD solutions were prepared and then used to deposit HTL above the perovskite. It is not recommended to wait hours to use such a solution, which may decrease the efficiency of the devices. Each device was prepared using 50 µL of fresh Spiro-OMeTAD solution doped in dynamic mode with a rotation speed of 4000 rpm for 20 s. The dispersion of the solution was done all at once, with constant speed without taking too long and at the same time without being too aggressive. Preparation of doped Spiro-OMeTAD films is a crucial step for obtaining high-efficiency devices. In addition, it is worth mentioning that the perovskite film was cooled to room temperature. If the device is still hot during HTL deposition, efficiency may be compromised due to reduced mobility of Spiro-OMeTAD doped holes under the influence of high temperature. No heat or surface treatment was applied after the deposition of the HTL.

After deposition of the HTL, the samples were stored for at least 16 h inside a desiccator with a molecular sieve, with no vacuum applied, in the dark, with low humidity. This process was carried out outside the glovebox and is very important to complete the slow oxidation of Spiro-OMeTAD with the aid of doping to maximize hole mobility. Then, contact cleaning with acetonitrile was performed to remove the layer and perovskite and HTL in the same region protected against ETL deposition with scotch magic tape, as exemplified in Figure 16.

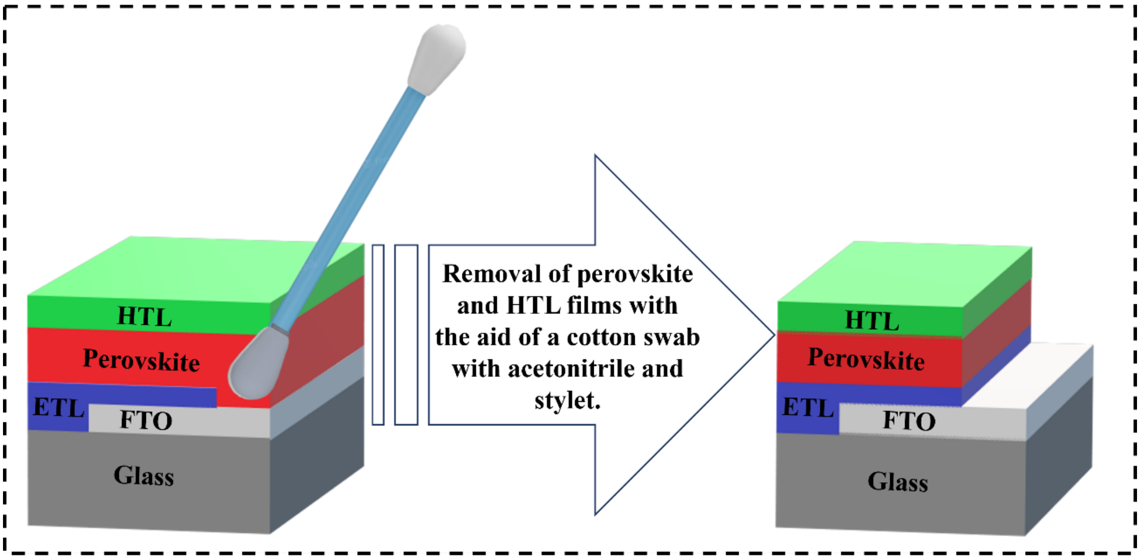

Figure 16: Schematic of the contact cleaning process to remove the perovskite and HTL films using a cotton swab with acetonitrile in the same area where the protection against ETL was carried out with a scotch magic tape.

Source: Prepared by the author.

3.2.5 Metal electrode evaporation

The gold electrodes were deposited by thermal evaporation at a rate of 0.1 Å.s^{-1} for the first 5 nm and then increased to 1.0 Å.s^{-1} until reaching 70 nm in thickness. The initial pressure was 5 x 10^{-6} mbar inside a glove box. A metallic mask delimits the device's contours with each substrate's three possible useful areas. Due to the capacity of the metallic mask used in this step, each batch is limited to a maximum of twenty devices. Furthermore, after evaporation of the metallic contact, the devices were kept under a vacuum until the support containing the samples slowly cooled down, approximately 30 min. After this period, the N_2 refill was activated, and the vacuum started to be broken while the support cooled to room temperature. This second process took around 20 min. That was done to avoid reducing the device's properties as Spiro-OMeTAD is very sensitive to high temperatures, especially in the presence of gases, even if inert, compromising its mobility of holes and the effect of the doping agents used. Figure 17 shows the architecture of the devices manufactured.

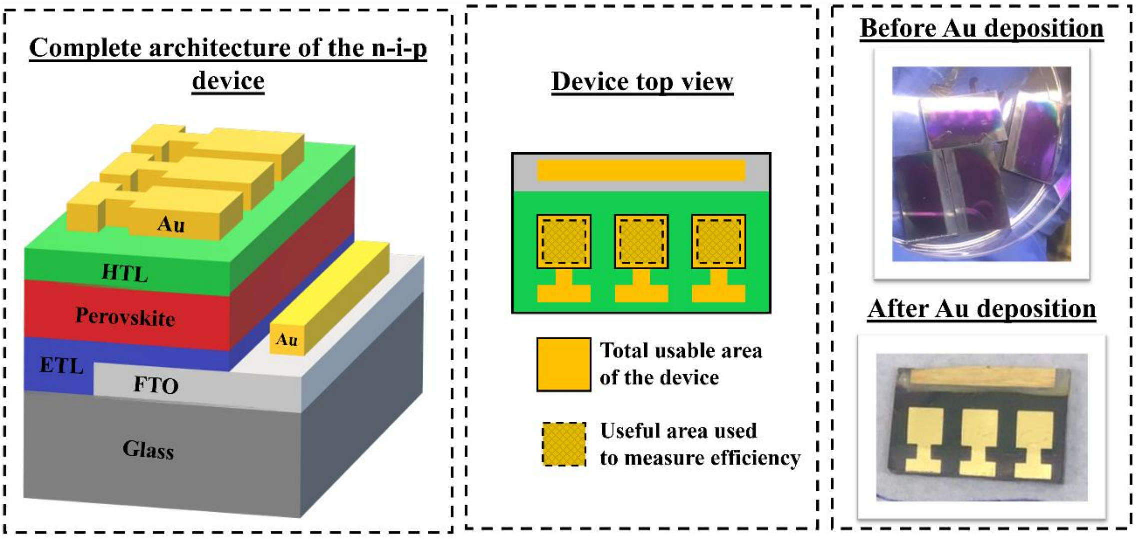

Figure 17: Architecture of manufactured devices.

Source: Prepared by the author.

3.3 DEVICE CHARACTERIZATION

The devices were characterized through their JV curves under lighting, as a radiation source, a 300 W Xenon lamp (Newport Co.) with a 1.5G AM filter. The JV curves were determined by a Keithley 2400 peak ammeter. The standard radiation intensity (1000 W m^{-2}) is determined by a Newport thermopile sensor in the Solar Sciencetech class AAA simulator. The JV curves were obtained from 0 to 1.20 V for both forward and backward scanning, with steps of 10 mV and a delay time of 0.25 s. The cells were masked with a black metal mask limiting the active area to 0.16 cm^2 and reducing the influence of the scattered light.

This curve makes it possible to obtain the photovoltaic parameters (V_{oc}, J_{sc}, FF), allowing the device efficiency (PCE) to be calculated. Figure 18 (a) shows the characteristic JV curves of the devices in the backward and forward directions. The current density was calculated from the ratio between the current measured by the active area of the device (0.16 cm^2). Figure 18 (b) shows the representative scheme for obtaining the photovoltaic parameters and the fill factor (FF) and power conversion efficiency (PCE) calculations. In short:

- V_{oc}: open-circuit voltage, representing the voltage with zero current density;
- V_{mp}: maximum power point voltage, representing the voltage at the maximum power point;

- J_{sc}: short-circuit current density, representing the current density with zero voltage; it was calculated
- J_{mp}: maximum power point density current, representing the current density at the maximum power point;
- P_{max}: maximum power obtained by the device;
- P_{in}: incident light power, 1000 W m^{-2} multiplied by the fraction of light intensity incident on the reference electrode during measurement. For example, if the light intensity is 99.5% of one sun, the incident power value will be 995 W m^{-2}. The results obtained in the present work were only accepted as valid results in which the lighting intensity was between 99.0 and 101.0%, that is, tolerating a variation of only 1.0% in the intensity of the incident radiation referring to 1 Sun;
- Area I: green rectangle area representing the power obtained by the device;
- Area II: blue rectangle area representing an ideal device with maximum use of power.

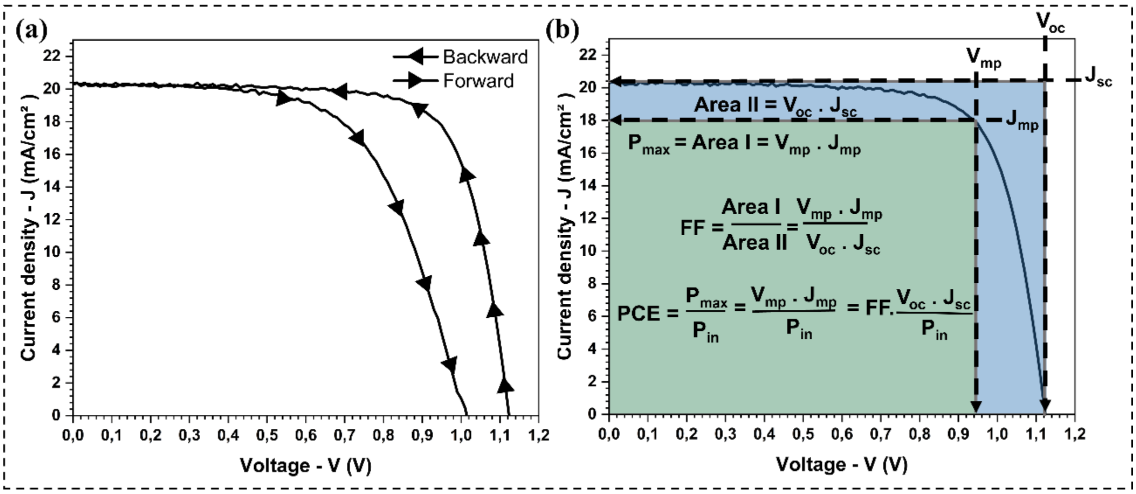

Figure 18: Device backward and forward characteristic curves (a); representative scheme of obtaining the photovoltaic parameters (b).

Source: Prepared by the author.

The parameters mentioned previously were obtained for both forward and backward curves. The real PCE was attributed to the mean of the PCE obtained by each device's backward and forward curve. Furthermore, the hysteresis index (HI) was calculated according to Equation (1).

$$HI = \frac{(PCE_{Backward} - PCE_{Forward})}{PCE_{Backward}} \quad \text{Equation 1}$$

3.3.1 Statistical treatment of the data obtained

The data obtained from the JV curves are presented according to the box plot statistics, as shown in Figure 19. The first quartile (Q1) represents 25% of the data, while the third quartile (Q3) represents 75%. The second quartile (Q2) represents the central data of the distribution, known as the median. The different interquartile (IQR) obtains a statistical value of the reliability of the data that can differentiate the statistically significant data from the outliers. Mathematically, the IQR is obtained through the difference of the values of the representative data Q3-Q1. The multiplicative factor of 1.5 in the IQR is generally used to determine the significant data of a population. The arithmetic mean describes a corresponding central value on the influence of all data and a reliable value that could describe the population. By evaluating the position of the mean and median, it is possible to verify the symmetry of the data distribution, which is also presented in the graphs of the results.

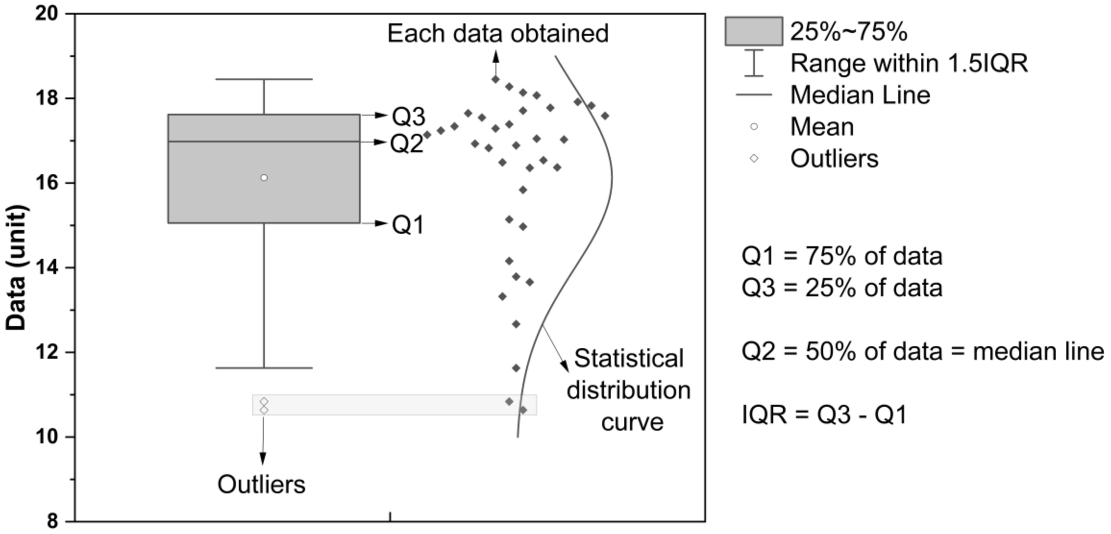

Figure 19: An example of how the data are presented in the present work, demarcating the main statistical values.

Source: Prepared by the author.

Figure 17 (a) shows the statistical limit related to the box plot with 1.5 IQR. It is possible to observe that this factor can describe at least 99.3% of the data, being a complete way of expressing the data of a population. In addition, it is possible to observe that within the box between Q1 and Q3 contained 50% of the population data. The IQR is another significant limitation of the data for comparing populations. This figure also compares how to represent the data as a function of the standard deviation (σ). The standard deviation is a measure that indicates the dispersion of data within a sample concerning the mean. The standard deviation describes how far the points are from the mean. The standard error (SE) measures a sample mean's variation in relation to the population mean. Therefore, it is a measure that helps to verify the reliability of the calculated sample mean. The standard deviation and standard error can be mathematically obtained by Equations 2 and 3, respectively.

$$\sigma = \frac{\sqrt{\Sigma(X_i - \bar{x})}}{n} \qquad \text{Equation 2}$$

$$SE = \frac{\sigma}{\sqrt{n}} \qquad \text{Equation 3}$$

Being: $\bar{x}$: average of values;

n: population size.

The greater the number of experiments for a sample, the more the sample mean and standard deviation of a group approaches its population value and real parameter. For experiments with fewer than 30 replications, it is necessary to consider a factor related to the probability density for the likelihood of this data. In addition, comparing only two data sets with sample mean and standard deviation without knowing their size drastically masks the interpretation of the results. Thus, it is necessary to incorporate in the interpretation of the results a factor capable of describing the probability density of a random variable, that is, that follows a probability distribution. The normal distribution from the z test approximates the range of mean and standard deviation to $\bar{x} \pm 1.96\sigma$, when there are at least 30 reproductions of the same experiment, which adds 95% reliability for a symmetrical distribution (one tail). The t-Student distribution also obtains a similar value. The presentation of data of $\bar{x} \pm \sigma$ (mean ± standard deviation) performed in many works compares a 64% confidence interval, being too low to compare two groups of samples. If the results follow a skewed distribution, such a way of presenting the data is still biased. That is because the standard deviation is relative to a central value that scatters the data evenly to both sides. Already 99.3% of confidence is related to the use of $\bar{x} \pm 2.698\sigma$, increasing the accuracy for representing the dispersion of data. Such factor relationships for standard deviation with the distribution curve confidence interval are shown in Figure 20 (b).

The confidence interval (CI) is important to indicate the margin of uncertainty (or imprecision) in the face of a calculation performed. This calculation uses the study sample to estimate the actual size of the outcome in the source population. Calculating a confidence interval is a strategy to differentiate two samples statistically. If there is an agreement between the intervals, it can be inferred that statistically, the values are equal at a certain confidence limit. The confidence interval with 99% significance is a way of predicting whether the result obtained is contained in this set and is a good way of describing it from the mean, being able to differentiate them or not from another set. Such a significance level describes 99% of the area below the probability distribution or the total accumulated probability. In other words, 99% of the range contains the sample mean, representing an adequate statistical model to interpret the data from a set of experiments with less than 120 replicates.

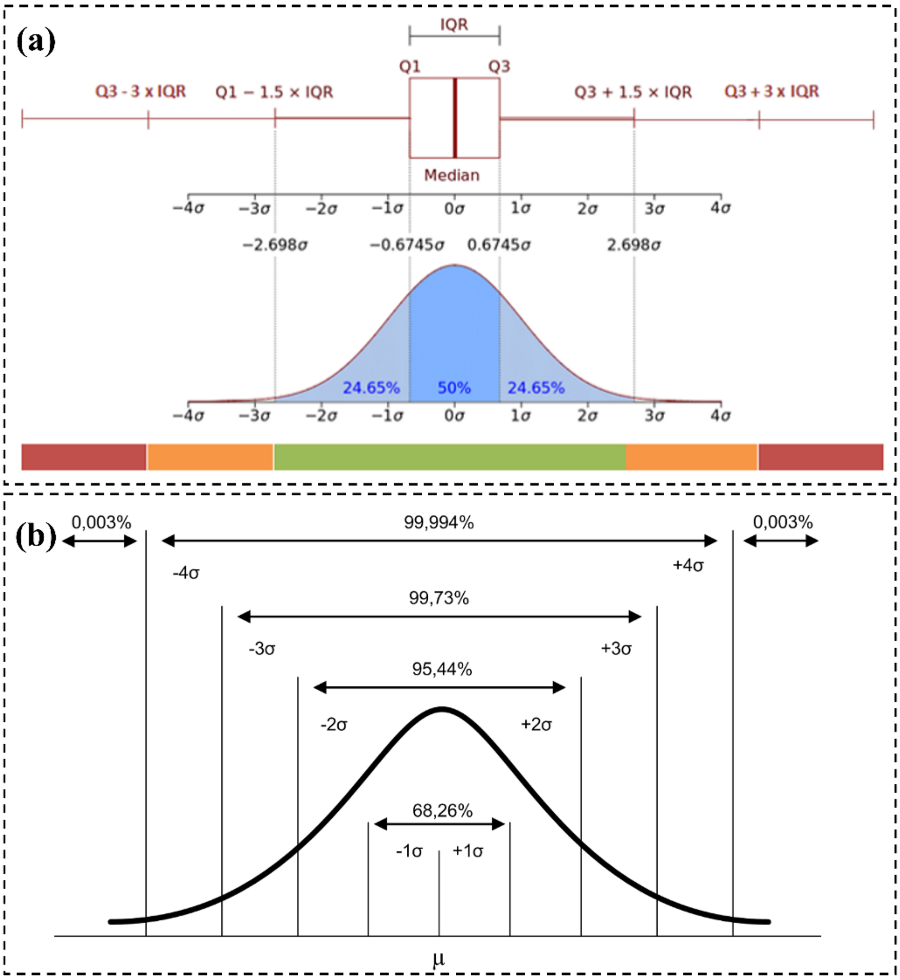

Figure 20: Comparative scheme concerning conventional statistical methods for data representation (a) and their respective confidence intervals in relation to the standard deviation (b).

Source: Naghshin, Vahid (2020) and Galvão, Walxiney (2020).

The results of the present work will be presented in the tables according to the 99% confidence limit and by box plot in graphics. The Student's t distribution is a probability distribution very similar to the normal distribution. It is also a bell-shaped distribution and is symmetrical about the mean. The big difference is that its use is for cases where the samples are small, the sample space is smaller than 120 units, and the population standard deviation is unknown. It is worth mentioning that sample spaces with more than 30 units are already considered large, and the normal distribution according to the z statistic is a good approximation. As in the present work, the standard deviation calculated is from the analyzed sample space, and the number of measurements is less than 120, or for most samples less than 30, it is appropriate to use the Student’s t statistic, with t being the Student parameter. Table 3 shows the values of the t-Student parameter for a distribution curve concerning the degree of freedom. The lateral line of the Student's t-distribution table represents the degree of freedom defined in the test by (n-1). In other words, 14 measurements were performed for a sample; in the table, one should look for the value 13 related to the degree of freedom by calculating 14-1=13. For intermediate values to the degrees of freedom of the table, interpolation must be performed concerning t-parameters. The t-Student values are still different depending on whether the distribution curve is symmetrical or skewed. The tails on both sides are equal for symmetric distributions, so it is considered a one-tailed statistic. For skewed distributions, where the mean and median do not match because the data tend to one end, there are two different tails, so it is considered a two-tailed statistic.

$$\text{Result} = \bar{x} \pm t.\frac{(\sigma)}{\sqrt{n}} \qquad \text{Equation 4}$$

Table 3: Parameter values for Student's t distribution.

One-tailed	**99%**	**99.5%**	**One-tailed**	**99%**	**99.5%**	**One-tailed**	**99%**	**99.5%**
Two-tailed	**98%**	**99%**	**Two-tailed**	**98%**	**99%**	**Two-tailed**	**98%**	**99%**
1	31.820	63.66	**14**	2.624	2.977	**27**	2.473	2.771
2	6.965	9.925	**15**	2.602	2.947	**28**	2.467	2.763
3	4.541	5.841	**16**	2.583	2.921	**29**	2.462	2.756
4	3.747	4.604	**17**	2.567	2.898	**30**	2.457	2.750
5	3.365	4.032	**18**	2.552	2.878	**40**	2.423	2.704
6	3.143	3.707	**19**	2.539	2.861	**50**	2.403	2.678
7	2.998	3.499	**20**	2.528	2.845	**60**	2.390	2.660
8	2.896	3.355	**21**	2.518	2.831	**80**	2.374	2.639
9	2.821	3.250	**22**	2.508	2.819	**100**	2.364	2.626
10	2.764	3.169	**23**	2.500	2.807	**120**	2.358	2.617
11	2.718	3.106	**24**	2.492	2.797	**>120**	2.326	2.576
12	2.681	3.055	**25**	2.485	2.787			
13	2.650	3.012	**26**	2.479	2.779			

Source: Prepared by the author.

4. RESULTS AND DISCUSSION

The presentation of the results and their discussions of the device performances were organized in 5 chapters according to the sample groups mentioned in the methodology. The results will first be described in terms of the photovoltaic parameters. At the end of each session, they will be corroborated and interpreted according to works in the literature. Below is the sequence of the experiments to be followed:

- 4.1 Group 1: Pure SnO_2
- 4.2 Group 2: SnO_2 (IPA) + GNP
- 4.3 Group 3: SnO_2 (H_2O) + GNP
- 4.4 Group 4: double layer of SnO_2 (IPA) + GNP
- 4.5 Group 5: SnO_2 (IPA) + different types of nanoparticles

4.1 GROUP 1: PURE SnO_2

Figure 21 presents the V_{oc} results for devices with SnO_2-based electron transport layers from precursors used in the literature. It can be seen that there is a significant difference between the forward and backward curves of samples without ETL and SnO_2 from $SnCl_4.5H_2O$ precursors without surface treatment. At first, the reverse curve is performed, and then the direct curve. Under the incidence of light, due to the photovoltaic effect, there is the power of an electric voltage and/or current that tends to favor the polarizations that interfere with the direction of the charge. It makes the reverse curve generally perform the best (CHEN *et al.*, 2016).

The difference in open-circuit voltage in the mentioned directions is one of the main reasons for hysteresis due to carrying charges at the interfaces. The V_{oc} also drastically affects the interface, which corroborates the identification that surface treatment with KCl tends to decrease the property difference in the device concerning the voltage sweep directions. However, it is possible to observe that compared to the devices without the surface treatment, there is a slight reduction of this parameter and increased data dispersion. That is probably due to the heterogeneity K^+ and Cl^- add to the device. However, it generally improves the interface between ETL and perovskite by reducing the V_{oc} difference between the scanning directions. The doping of positive potassium and negative chloride ions reduces polarization effects, making the devices' behavior more similar in the scanning directions. Another phenomenon observed is the increase of V_{oc}

in the forward direction in relation to the sample without surface treatment (ZHU, Pengchen *et al.*, 2020).

In general, doubling the precursor solution concentration tends to increase the thickness of the ETL layer. In the SnO_2 (IPA) 0.1M samples, there is a reduction in V_{oc}, which is due to lower efficiency of charge extraction or an increase in the probability of recombination due to the increase in the diffusion path through the ETL. Devices without ETL have low efficiency in extracting charges from the active layer. Removing the layer responsible for the extraction of electrons causes the perovskite to be in direct contact with FTO, increasing the drastic difference in the LUMO orbitals responsible for the cascade effect of electrons. It is observed by the drastic reduction of V_{oc} and accompanied by the increase of data dispersion. In addition, these devices also have a significant V_{oc} difference between the sweep directions.

The use of nanoparticles tends to generate greater roughness at the interface. It increases the surface area of the interface, which improves charge extraction. The SnO_2 (H_2O) samples slightly decreased the V_{oc} and the data scatter. The difference in V_{oc} in this sample's backward and forward directions was the smallest, even concerning the surface treatment of KCl.

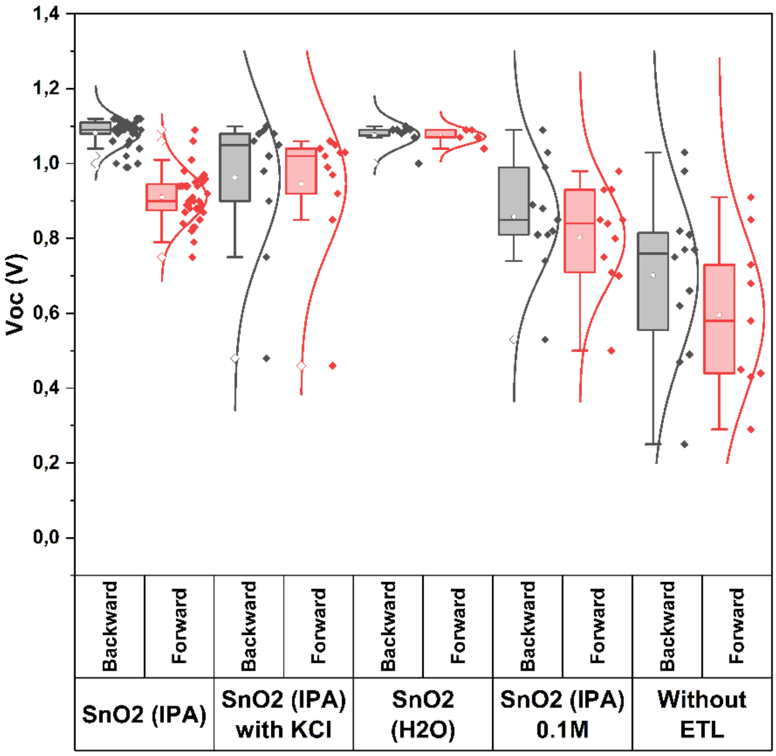

Figure 21: Graphic presentation of V_{oc} by box plot statistics and distribution curve for experiments of Group 1 with pure SnO_2 extracted from the JV curves of devices under 1 Sun illumination.

Source: Prepared by the author.

Figure 21 shows that the layers with SnO_2, regardless of the methodology, do not sharply reduce the short-circuit current (J_{sc}) response. Only the sample without ETL showed a very drastic reduction. In addition, the responses in the current generation were not much affected concerning the sweep direction. It can be explained by the J_{sc}, which represents the charge generation capacity by the active layer; the ETL employed does not harm the perovskite operation. Passivation with KCl and the use of nanoparticles increased data dispersion and slightly reduced J_{sc}. The increase in the surface heterogeneity reduces surface energy by the insertion of KCl, and a larger interfacial area can raise the possibility of electrons scattering (SOLANKI *et al.*, 2019). On the other hand, doubling the precursor solution concentration did not significantly affect J_{sc}.

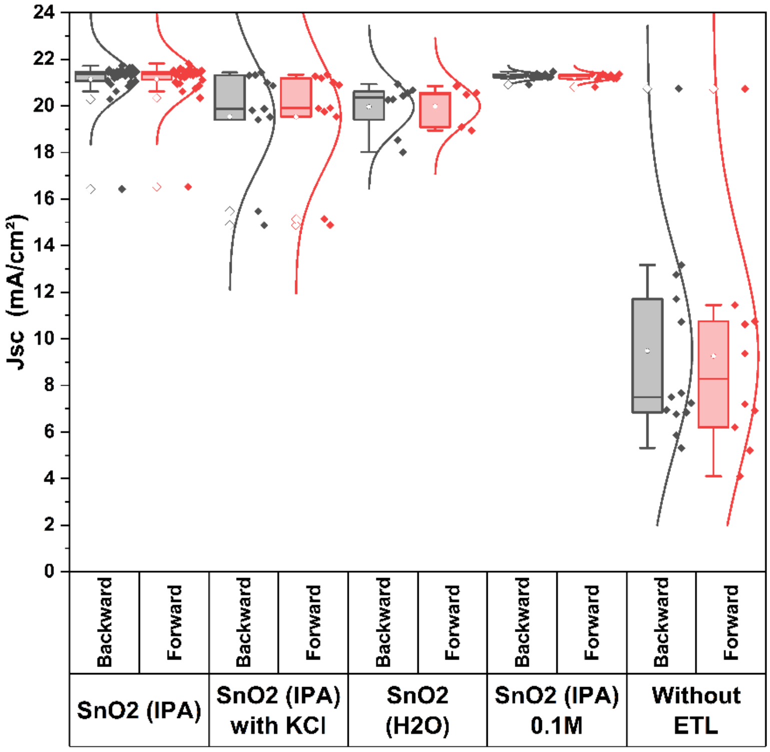

Figure 22: Graphic presentation of J_{sc} by box plot statistics and distribution curve for experiments of Group 1 with pure SnO_2 extracted from the JV curves of devices under 1 Sun illumination.

Source: Prepared by the author.

Table 4 presents V_{oc} and J_{sc} data with their respective 99% confidence limits and corresponding records. It is possible to observe that the samples SnO_2 (IPA), SnO_2 (IPA) with KCl, and SnO_2 (H_2O) did not present statistically significant differences in V_{oc} (backward) and J_{sc} (backward and forward). On the other hand, SnO_2 (IPA) shows a significant decrease in V_{oc} in the forward direction concerning the mentioned samples, which suggests a greater hysteresis. However, it can be noticed that SnO_2 (IPA) has higher average and record values in all these parameters. The sample SnO_2 (IPA) 0.1 M presented a significant reduction in the average values in V_{oc} in both directions.

Figure 23: Graphic presentation of FF by box plot statistics and distribution curve for experiments of Group 1 with pure SnO2 extracted from the JV curves of devices under 1 Sun illumination. It can be observed that the fill factor (FF) has a more drastic change concerning the parameters of J_{sc} and V_{oc} in relation to the precursors of the ETL. The reduction of FF values and the increase of data dispersion confirms the favoring of recombination processes owing to the insertion of defects due to K+ doping (SnO_2 (IPA) with KCl), the increase in roughness and surface area at the interface of the ETL (SnO_2 (H2O)), as well as the increase in the electron diffusion path (SnO_2 (IPA) 0.1M). Removing the ETL reduces electron extraction and increases the probability of recombination, as seen in the sharp drop in FF.

Table 4: Voc and J_{sc} data from Group 1 for experiments with pure SnO_2 extracted from the JV curves of devices under 1 Sun illumination, represented in terms of [mean ± 99% confidence limit (best)].

	V_{oc} (max) [V]		**J_{sc} (max) [mA/c²]**	
	Backward	**Forward**	**Backward**	**Forward**
SnO_2 (IPA)	1.08 ± 0.02 (1.12)	0.91 ± 0.03 (1.09*)	21.14 ± 0.39 (21.72)	21.15 ± 0.39 (21.82)
SnO_2 (IPA) with KCl	1.01 ± 0.10 (1.10)	1.00 ± 0.06 (1.06)	20.00 ± 1.69 (21.43)	19.99 ± 1.75 (21.34)
SnO_2 (H_2O)	1.08 ± 0.04 (1.10)	1.07 ± 0.03 (1.09)	19.96 ± 1.19 (20.93)	19.98 ± 1.45 (20.85)
SnO_2 (IPA) 0.1M	0.86 ± 0.14 (1.09)	0.8 ± 0.12 (0.98)	21.26 ± 0.13 (21.47)	21.23 ± 0.14 (21.35)
Without ETL	0.70 ± 0.19 (1.03)	0.6 ± 0.22 (0.91)	9.48 ± 3.44 (20.74*)	9.26 ± 4.51 (20.73*)

***** Data presented outside the limit established by the box plot of 1.5 IQR, being considered invalid (outlier).

Source: Prepared by the author.

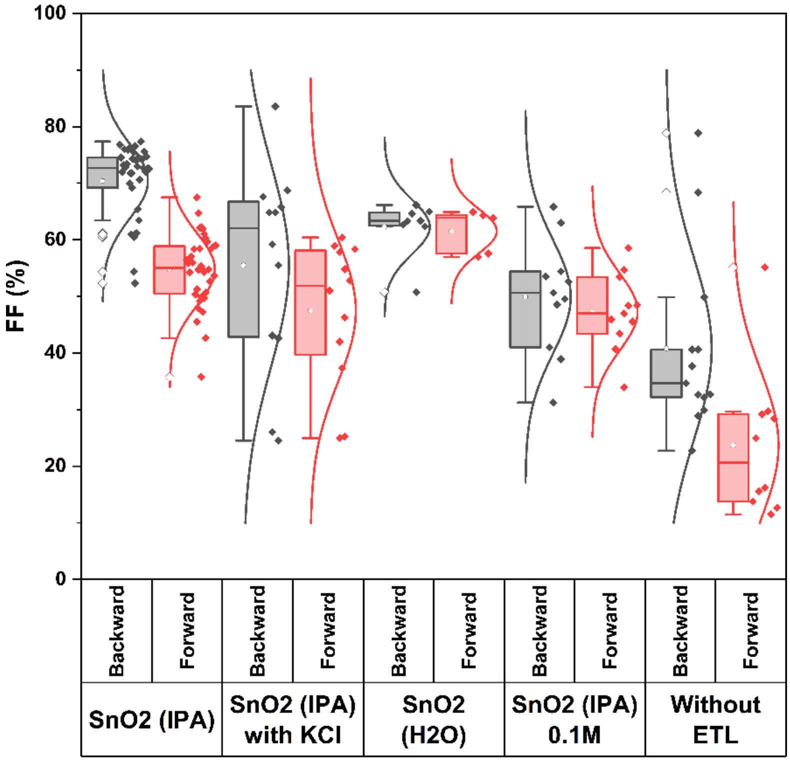

Figure 23: Graphic presentation of FF by box plot statistics and distribution curve for experiments of Group 1 with pure SnO_2 extracted from the JV curves of devices under 1 Sun illumination.

Source: Prepared by the author.

The energy conversion efficiency (PCE) is the mutual contribution of the photovoltaic parameters and the good contribution of the other layers in the extraction and transport of charges. In Figure 24, the great variation in the results in relation to the different SnO_2 precursors can be observed. The ETL that presented the best performance in the backward response was the SnO_2 (IPA) methodology. In the forward direction, it was from the colloidal solutions of nanoparticles (SnO_2 (H_2O)), which also showed the greatest similarity between both scanning directions. The removal of the ETL drastically compromised the functioning of the devices, reaffirming the need for a layer responsible for the extraction and conduction of electrons efficiently.

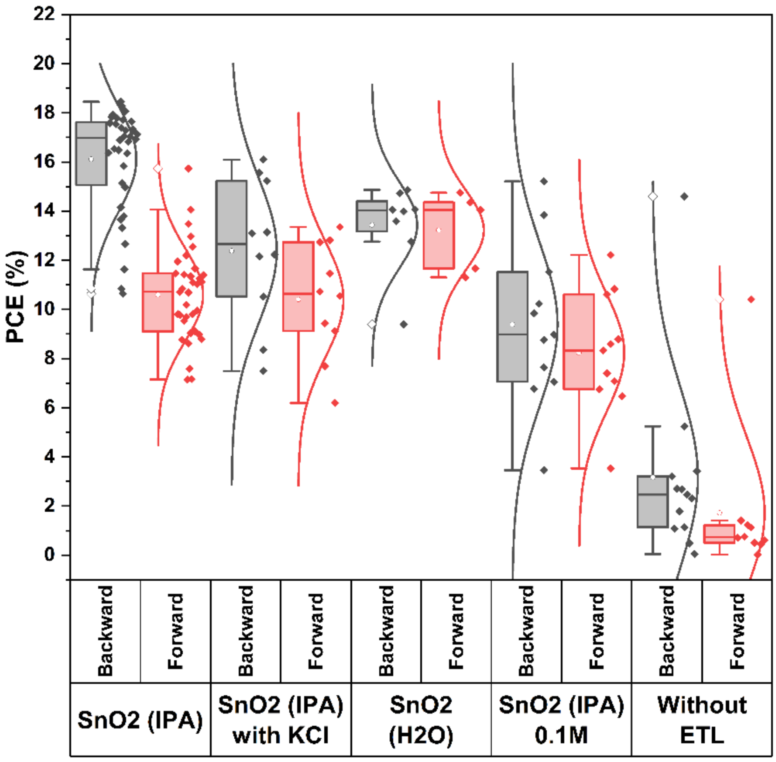

Figure 24: Graphic presentation of PCE by box plot statistics and distribution curve for experiments of Group 1 with pure SnO_2 extracted from the JV curves of devices under 1 Sun illumination.

Source: Prepared by the author.

In Table 5, it can be seen that the SnO_2 (IPA) samples with KCl and SnO_2 (H_2O) present similar results for FF and PCE, yet they have a low influence on the scanning direction of the device's performance. SnO_2 (IPA) 0.1 M presents a significant reduction in FF due to the probability of charge recombination, which implies a reduction of almost half the efficiency of the devices. The effect of removing the ETL is even more drastic, generating devices with less than 2% efficiency. The control sample SnO_2 (IPA) is the one that showed excellent PCE of 16.1 ± 1, and still with devices with values greater than 18% efficiency. However, in the forward direction, the efficiency is lower than the SnO_2 (H_2O) sample (13.2 ± 2.6) and similar to SnO_2 (IPA) with KCl.

The efficiencies of the control devices produced in the present work were consistent with those in the literature for CsMAFA perovskite with the respective methodologies (HUANG, Shumin *et al.*, 2022). SOLANKI *et al.* (2019) observed a maximum of 17.9% efficiency in backward measures, with the results of the present study being even higher (18.5%). DENG, CHEN, and Li (2020) also reported the best efficiency of 17% in the backward direction compared to 14.82% in the forward from $SnCl_2$ or $SnCl_4$.

Table 5: FF and PCE data from Group 1 for experiments with pure SnO_2 extracted from the JV curves of devices under 1 Sun illumination, represented in terms of [mean ± 99% confidence limit (best)].

	FF (max) [%]		PCE (max) [%]	
	Backward	**Forward**	**Backward**	**Forward**
SnO_2 (IPA)	70 ± 3 (77)	55 ± 3 (67)	16.1 ± 1.0 (18.5)	10.6 ± 0.9 (15.7*)
SnO_2 (IPA) with KCl	62 ± 12 (84)	52 ± 7 (60)	12.4 ± 2.8 (16.1)	10.4 ± 2.2 (13.4)
SnO_2 (H_2O)	62 ± 5 (66)	62 ± 6 (65)	13.4 ± 2.0 (14.9)	13.2 ± 2.6 (14.8)
SnO_2 (IPA) 0.1M	50 ± 9 (66)	47 ± 6 (59)	9.4 ± 3.0 (15.2)	8.2 ± 2.2 (12.2)
Without ETL	41 ± 13 (79*)	24 ± 13 (55*)	3.2 ± 3.0 (14.6*)	1.7 ± 2.9 (10.4*)

* Data presented outside the limit established by the box plot of 1.5 IQR, being considered invalid (outlier).

Source: Prepared by the author.

The devices showed a significant difference in efficiency in the scanning direction. Thus, it is necessary to verify the real conversion efficiency of the devices, which is shown in Figure 25 and is given by the average value of each backward and forward average. The control samples with the precursors $SnCl_4.5H_2O$ (SnO_2 (IPA)) and the colloidal dispersion of nanoparticles showed identical real performance. Statistically, the surface modification with KCl also coincided with these mentioned samples but with greater data dispersion. The three methodologies produced ETL matching at least 50% of the data. Colloidal nanoparticles have lower data dispersion and real high efficiency.

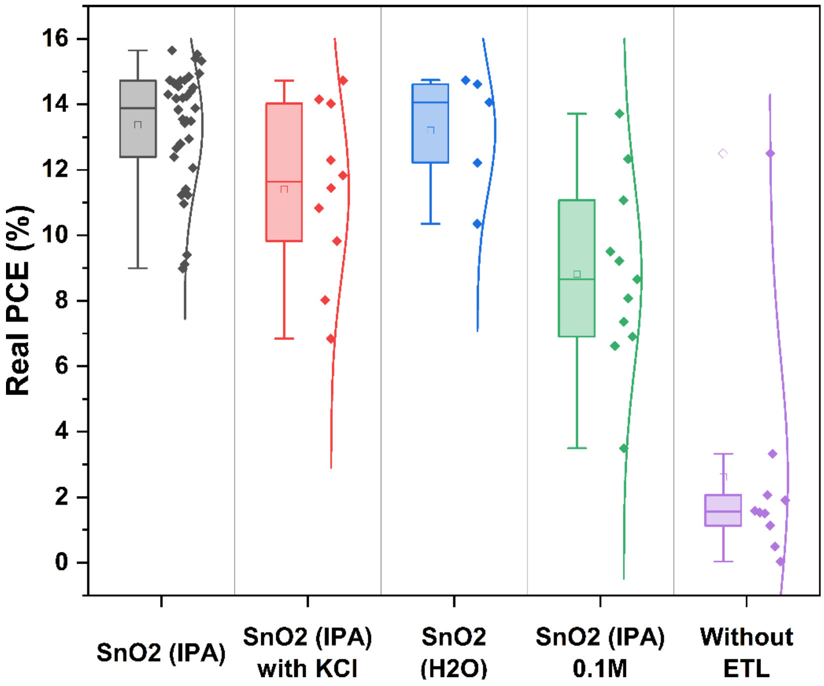

Figure 25: Graphic presentation of real PCE by box plot statistics and distribution curve for experiments of Group 1 with pure SnO_2 extracted from the JV curves of devices under 1 Sun illumination.

Source: Prepared by the author.

The hysteresis index shown in Figure 26 was significantly reduced by the methodologies doubling the concentration of the precursor solution, passivation with KCl, and colloidal dispersion. However, only the last two mentioned methodologies showed promising real efficiencies. Although the production of ETL by $SnCl_4$ has high hysteresis, it remains the sample with the highest Real PCE. Removing ETL, in addition to presenting low efficiency, generates very high hysteresis with large data dispersion.

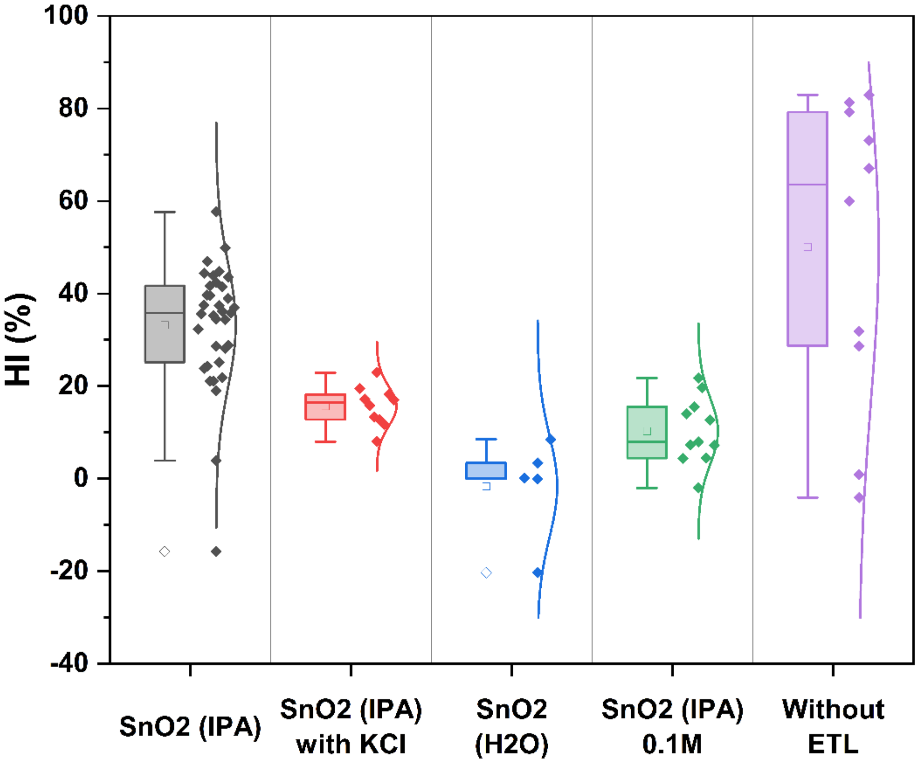

Figure 26: Graphic presentation of HI by box plot statistics and distribution curve for experiments of Group 1 with pure SnO_2 extracted from the JV curves of devices under 1 Sun illumination.

Source: Prepared by the author.

The real PCE data presented in Table 6 with its 99% confidence limits demonstrate that, statistically, the SnO_2 (H_2O) and SnO_2 (IPA) with KCl and SnO_2 (IPA) samples show the most promising performance. It is worth mentioning that the control samples from the $SnCl_4$ precursors and the nanoparticle's colloidal suspension present identical real efficiency averages. Concerning hysteresis, colloidal nanoparticles can generate electron transport layers with zero hystereses. YANG, Guang *et al.* (2018) reported that the improvement in hysteresis when using colloidal quantum dots suspensions of SnO_2 as an ETL precursor for perovskite is due to the good alignment of the HOMO and LUMO levels concomitant with the improvement of electrical conductivity and charge extraction because of the high surface area of the nanoparticles.

Despite the ETL SnO_2 (IPA) having the highest record of 15.7%, it also had high hysteresis values. Hysteresis not only reduces the actual efficiency but is also a way of evaluating the system's stability. Higher hysteresis generally reduces device lifetime (CUI *et al.*, 2020; TUMEN-ULZII *et al.*, 2020).

Table 6: Real PCE and HI data from Group 1 for experiments with pure SnO_2 extracted from the JV curves of devices under 1 Sun illumination, represented in terms of [mean ± 99% confidence limit (best)].

	Real PCE (max) [%]	**HI (|min|) [%]**
SnO_2 (IPA)	13.4 ± 0.8 (15.7)	35.3 ± 4.6 (-11.1*)
SnO_2 (IPA) with KCl	11.4 ± 2.5 (14.7)	15.6 ± 4.1 (8.0)
SnO_2 (H_2O)	13.2 ± 3.0 (14.7)	4.0 ± 17.7 (0)
SnO_2 (IPA) 0.1M	8.8 ± 2.6 (13.7)	11.5 ± 6.4 (-2.0)
Without ETL	2.6 ± 3.4 (12.5*)	56.1 ± 31.6 (-4.1)

* Data presented outside the limit established by the box plot of 1.5 IQR, being considered invalid (outlier).

Source: Prepared by the author.

Finally, Figure 27 shows the JV curves of the samples with the highest real PCE using different methodologies based on SnO_2. Hysteresis is evidenced by the difference between backward (B) and forward (F) curves. Furthermore, it is easy to observe that the most significant difference in reducing the efficiency of these devices is the reduction in V_{oc}, corresponding to the intercept of the abscissa axis (voltage value for zero current density). The SnO_2 (H_2O) exemplifies the sample with low hysteresis, in which the two curves are almost completely superimposed.

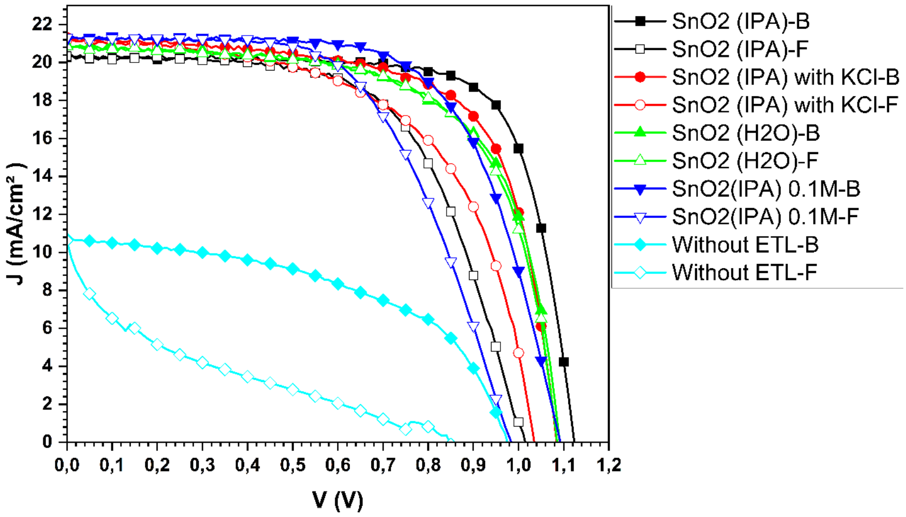

Figure 27: JV curve of the highest real PCE Group 1 devices with the pure SnO_2 experiments under 1 Sun illumination.

Source: Prepared by the author.

4.2 GROUP 2: SnO_2 (IPA) + GNP

In this section, the combination of the precursor $SnCl_4.5H_2O$ that obtained the hishest PCE results in the previous section with the incorporation of the most common commercial graphene, graphene nanoplatelets (GNP), in different contents, will be discussed. Figure 28 shows the behavior of V_{oc} concerning the increase in the concentration of graphene nanoplatelets (GNP). It is evident that increasing the concentration tends to reduce this parameter gradually. The efficiency of devices, in general, is directly related to the cohesion of the ETL layer and its crystalline structure. Graphene is a nanoparticle with a high surface area and significant lateral size dimensions compared to crystal lattices. Thus, the GNP present in SnO_2 films acts as heterogeneity. The interface between the nanoparticle and the SnO_2 matrix is similar to dislocations and grain boundaries. In these regions, aligning the LUMO energy levels may be difficult to ensure efficient electron transfer (SIDHIK *et al.*, 2018).

Concentrations above 0.5% GNP tend to present very similar V_{oc} regardless of the scanning direction. The first moment could suggest that it would be a direct reduction of the hysteresis due to the improvement of the interface. There are two possibilities: the stronger favoring of V_{oc} in the forward direction, decreasing the B-F difference, or reducing this parameter in the backward direction, making them equal. However, it is more evident that the GNP tends to reduce the polarization as it hinders the transport of charges in the backward scan, making the behavior closer to the forward one (CUI *et al.*, 2020; SIDHIK *et al.*, 2018). This theory is more significant because a clear decrease in V_{oc} can be observed as the filler concentration increases.

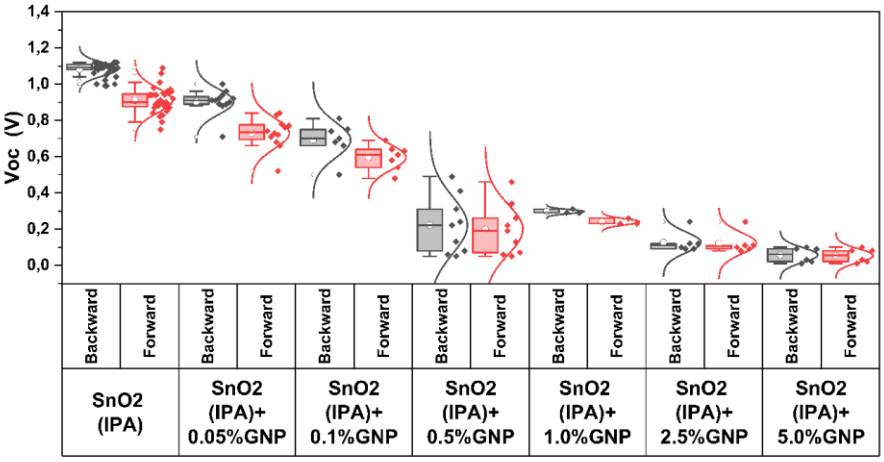

Figure 28: Graphic presentation of V_{oc} by box plot statistics and distribution curve for experiments of Group 2 with SnO_2 (IPA) containing different levels of GNP extracted from the JV curves of devices under 1 Sun illumination.

Source: Prepared by the author.

On the other hand, in Figure 29, J_{sc} does not have such a drastic reduction as observed in V_{oc}. It is evident that up to 0.5% there is photocurrent generation, which is very similar to the control device. From this concentration, it can be observed that there is a reduction in the current density while the data dispersion is increased. The active layer is not affected so much by the current generation due to the insertion of GNP. However, as observed in the photographs shown in Figure 12, the increase in GNP concentration tends to make the dispersions darker. Thus, it is believed that the reduction of the photocurrent from the increase in the GNP's concentration tends to reduce the collection of photons by the perovskite because the ETL layer becomes darker, slightly reducing the transmittance due to the greater absorbance and reflectance of this type of graphene (DEWI *et al.*, 2019).

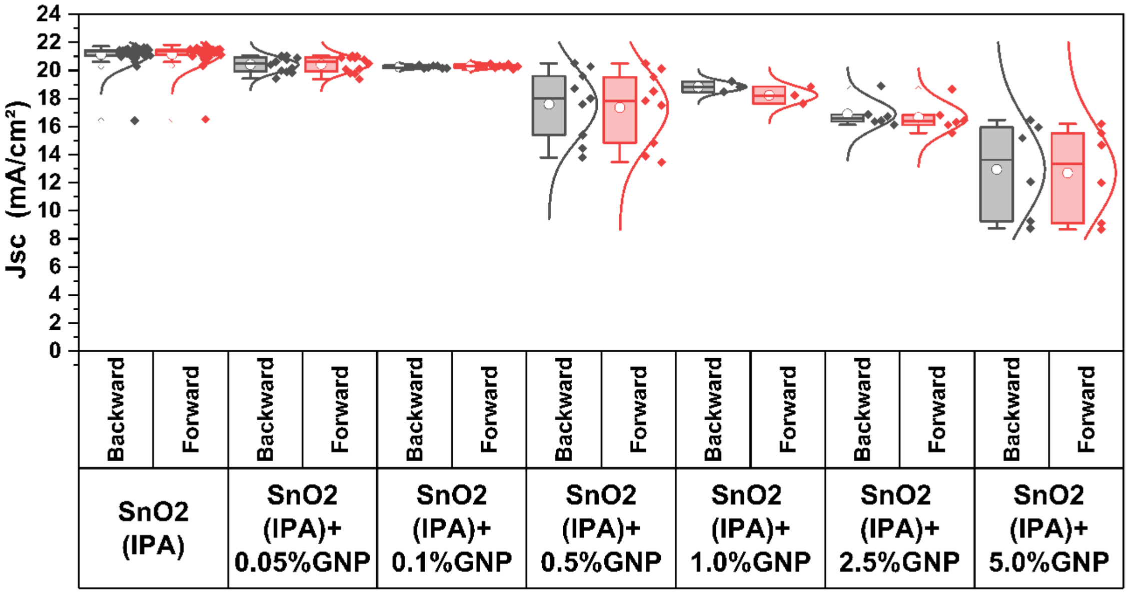

Figure 29: Graphic presentation of J_{sc} by box plot statistics and distribution curve for experiments of Group 2 with SnO_2 (IPA) containing different levels of GNP extracted from the JV curves of devices under 1 Sun illumination.

Source: Prepared by the author.

In Table 7, it is possible to observe, according to the 99% limit, that the insertion of graphene tends to significantly reduce the Voc parameter from 0.1% of GNP. However, for the J_{sc} parameter, such a drop is only more accentuated from 0.5%. Although J_{sc} decreased with increasing GNP concentration, even high concentrations showed very high J_{sc} values, above 16 mA/cm^2. Up to 1.0% GNP, the confidence interval for the short-circuit current density is statistically similar to the control layer of colloidal nanoparticles (SnO_2 (H_2O)), which obtained 19.96 ± 1.19% (20.93%) in backward and 19.98 ± 1.45%

(20.85%) in forward, exposed in the previous section concerning the experiments of Group 1.

Table 7: V_{oc} and J_{sc} data from experiments of Group 2 with SnO_2 (IPA) containing different levels of GNP extracted from the JV curves of devices under 1 Sun illumination, represented in terms of [mean ± 99% confidence limit (best)].

	V_{oc} (max) [V]		**J_{sc} (max) [mA/cm²]**	
	Backward	**Forward**	**Backward**	**Forward**
SnO_2 (IPA)	1.08 ± 0.02 (1.12)	0.91 ± 0.03 (1.09*)	21.14 ± 0.39 (21.72)	21.15 ± 0.39 (21.82)
SnO_2 (IPA)+ 0.05%GNP	0.90 ± 0.06 (1.00*)	0.73 ± 0.07 (0.84)	20.42 ± 0.47 (21.06)	20.44 ± 0.49 (21.05)
SnO_2 (IPA)+ 0.1%GNP	0.69 ± 0.12 (0.81)	0.60 ± 0.09 (0.69)	20.25 ± 0.12 (20.39)	20.29 ± 0.17 (20.47)
SnO_2 (IPA)+ 0.5%GNP	0.22 ± 0.16 (0.49*)	0.20 ± 0.14 (0.46)	17.59 ± 2.56 (20.51)	17.36 ± 2.73 (20.49)
SnO_2 (IPA)+ 1.0%GNP	0.30 ± 0.03 (0.31)	0.24 ± 0.05 (0.26)	18.84 ± 1.03 (19.22)	18.24 ± 1.67 (18.85)
SnO_2 (IPA)+ 2.5%GNP	0.13 ± 0.08 (0.24*)	0.12 ± 0.08 (0.24*)	16.90 ± 1.4 (18.89*)	16.65 ± 1.49 (18.67*)
SnO_2 (IPA)+ 5.0%GNP	0.06 ± 0.06 (0.10)	0.05 ± 0.05 (0.10)	12.95 ± 4.73 (16.47)	12.70 ± 4.53 (16.20)

***** Data presented outside the limit established by the box plot of 1.5 IQR, being considered invalid (outlier).

Source: Prepared by the author.

Figure 30 shows that the fill factor (FF) behavior is similar to that of J_{sc} as the GNP increases. However, this parameter represents the efficiency of extracting and collecting charges from the active layer. In other words, the explanation is more consistent with that of V_{oc}, where the increase in filler content tends to insert large defects, similar to dislocations and grain boundaries, due to the heterogeneity of the films owing to the nanoplatelets and their interface created with the SnO_2 (WU, Wu Qiang *et al.*, 2020). FF is also able to describe the occurrence of charge carrier recombination processes. Thus, it is believed that the interfaces created in the ETL volume tend to act as recombination centers, reducing the FF (WANG, Yongling *et al.*, 2019).

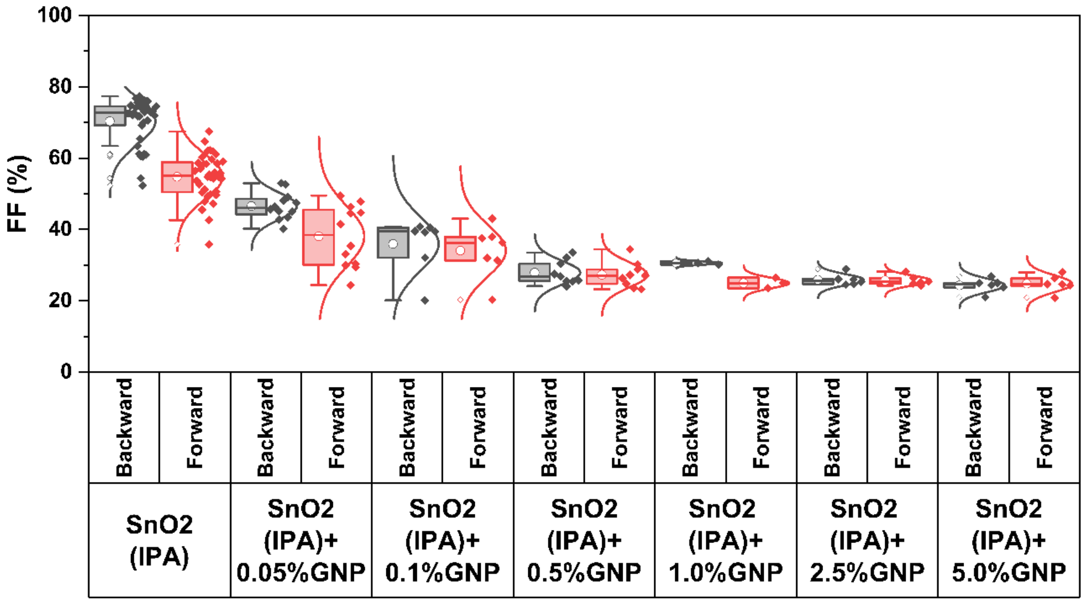

Figure 30: Graphic presentation of FF by box plot statistics and distribution curve for experiments of Group 2 with SnO_2 (IPA) containing different levels of GNP extracted from the JV curves of devices under 1 Sun illumination.

Source: Prepared by the author.

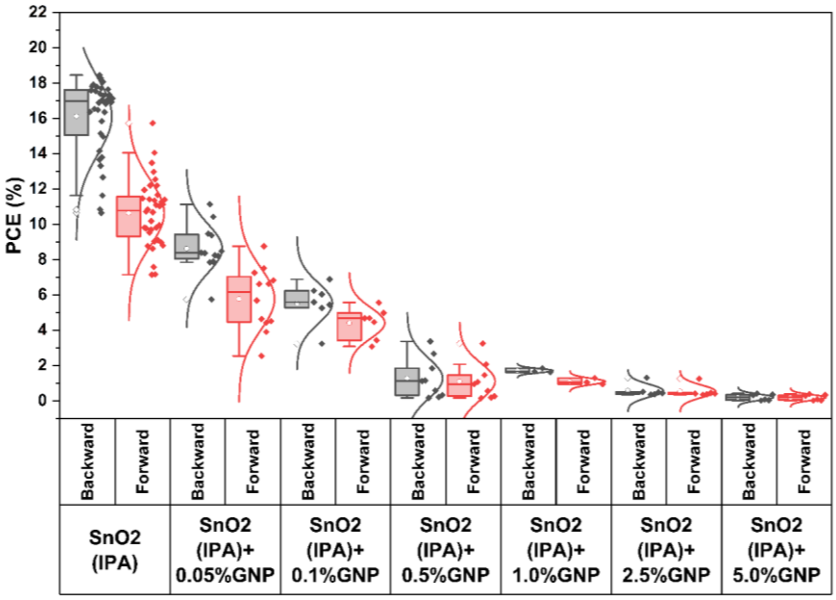

Figure 31: Graphic presentation of PCE by box plot statistics and distribution curve for experiments of Group 2 with SnO_2 (IPA) containing different levels of GNP extracted from the JV curves of devices under 1 Sun illumination.

Source: Prepared by the author.

The efficiency of the devices presents similar behavior to J_{sc} and FF; as the charge concentration increases, there is a gradual reduction in these parameters. The data distribution curves are also more symmetrical due to the incorporation of graphene, which is also evidenced by the greater proximity between the mean and the median. The device performance is a final answer that combines all the parameters mentioned. In this way, the reduction of this property is more drastic due to the mutual contribution of the problems presented in J_{sc}, V_{oc}, and FF (ZHU, Pengchen *et al.*, 2020). These results demonstrate a need to improve the graphene interface to be incorporated into the ETL of SnO_2.

In Table 8, it is possible to verify from the 99% confidence limit and the best values of each composition that even the smallest filler incorporation drastically increases the recombination, as evidenced by the FF and the reduction in the performance of the devices. Adding 0.05% makes the PCE drop by half. The efficiency dropped so much from 0.5% GNP that the solar modules obtained less than 2% PCE.

TAHERI-LEDARI; VALADI; MALEKI, (2020) obtained a maximum of 11% PCE (B) due to the insertion of graphene in the ZnO layer and highlighted that the pure rGO layer generated inefficient devices of 1% PCE. HAN *et al.* (2015) also reported that increasing graphene concentration reduces PSC efficiency. In addition, with the incorporation of 1.0% (vol), it obtained 11.7% efficiency (B) when combined with the mesoporous layer of TiO_2. This efficiency with high concentration was only possible thanks to optimizing the layer thickness, reaching 400 ± 20 nm of ETL. It is worth mentioning that this proportion was also performed concerning the volume and that the pure rGO layer generated a thickness of 20 µm.

Table 8: FF and PCE data from Group 2 for experiments with SnO_2 (IPA) containing different levels of GNP extracted from the JV curves of devices under 1 Sun illumination, represented in terms of [mean ± 99% confidence limit (best)].

	FF (max) [%]		**PCE (max) [%]**	
	Backward	**Forward**	**Backward**	**Forward**
SnO_2 (IPA)	70 ± 3 (77)	55 ± 3 (67)	16.1 ± 1.0 (18.5)	10.6 ± 0.9 (15.7*)
SnO_2 (IPA)+ 0.05%GNP	47 ± 3 (53)	38 ± 7 (50)	8.6 ± 1.2 (11.1)	5.8 ± 1.5 (8.8)
SnO_2 (IPA)+ 0.1%GNP	36 ± 9 (41)	34 ± 9 (43)	5.5 ± 1.4 (6.9)	4.4 ± 1.1 (5.6)
SnO_2 (IPA)+ 0.5%GNP	28 ± 3 (34)	27 ± 4 (34)	1.3 ± 1.2 (3.4*)	1.1 ± 1 (3.3*)
SnO_2 (IPA)+ 1.0%GNP	31 ± 1 (31)	25 ± 4 (27)	1.7 ± 0.3 (1.9)	1.1 ± 0.5 (1.3)
SnO_2 (IPA)+ 2.5%GNP	26 ± 2 (29)	26 ± 2 (28)	0.6 ± 0.5 (1.3*)	0.5 ± 0.5 (1.3*)
SnO_2 (IPA)+ 5.0%GNP	24 ± 3 (27*)	25 ± 3 (28)	0.2 ± 0.2 (0.4)	0.2 ± 0.2 (0.4)

***** Data presented outside the limit established by the box plot of 1.5 IQR, being considered invalid (outlier).

Source: Prepared by the author.

In Figure 32, it is observed that the real PCE also reduced as the GNP concentration increased. Even so, there is a coincidence at the lower interval limit established by the 1.5 IQR between the control sample and the composition with 0.05% filler. The dispersion of results is reduced due to the insertion of graphene. It is believed that there are point, linear, superficial, and volumetric defects in crystalline structures. As the size of the defects increases, they impact more on the properties. Thus, point defects are easier to spread through a film and have a variability of influence depending on whether they are substitutional or interstitial. That generates a wider dispersion of the data as each one will influence characteristically and also varies from its location. Large-area defects, such as the graphene interface with SnO_2, are so influential in the properties due to their high surface area and lateral size of the nanosheets that end up suppressing the smaller-dimensional effects. Therefore, GNP tends to reduce data dispersion with increasing content.

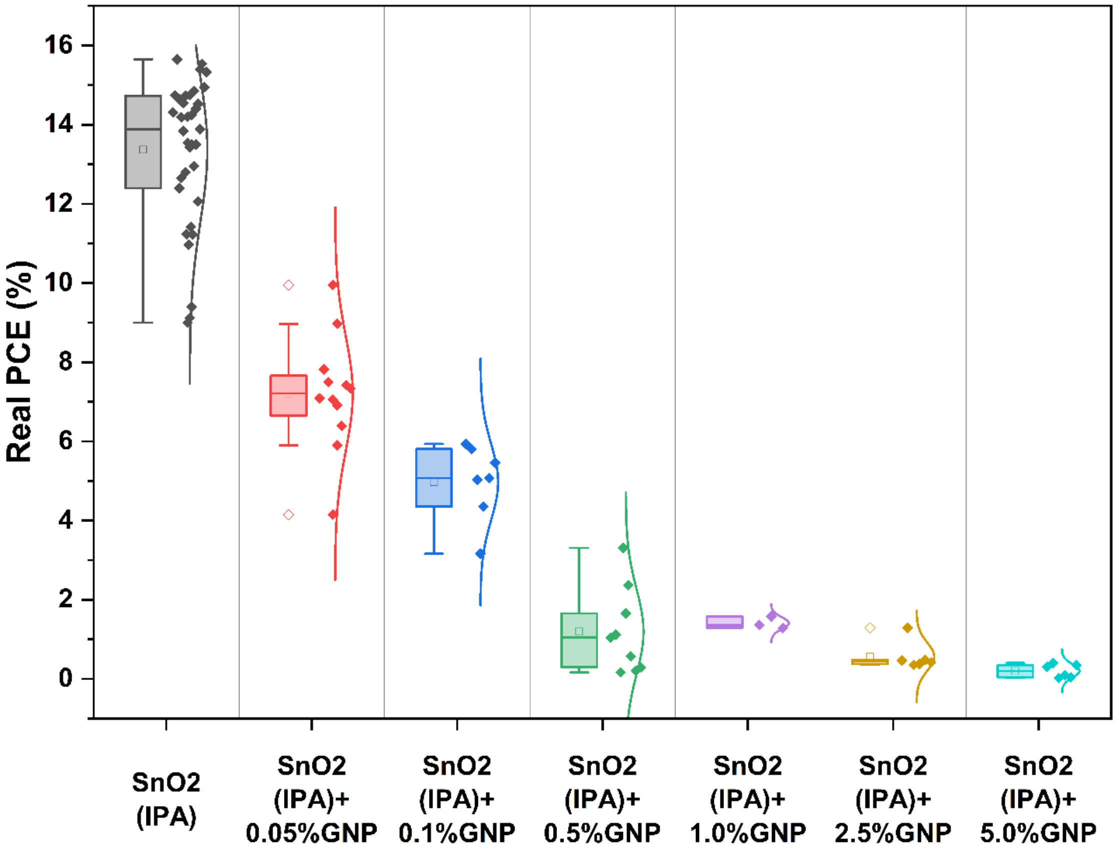

Figure 32: Graphic presentation of Real PCE by box plot statistics and distribution curve for experiments of Group 2 with SnO_2 (IPA) containing different levels of GNP extracted from the JV curves of devices under 1 Sun illumination.

Source: Prepared by the author.

As seen in Figure 33, the hysteresis index shows a slight reduction in the mean and median values and their dispersion as the GNP content increases. However, the content of 0.05% does not seem to have improved this parameter. Statistically, the control sample and the one with the lowest filler content are similar.

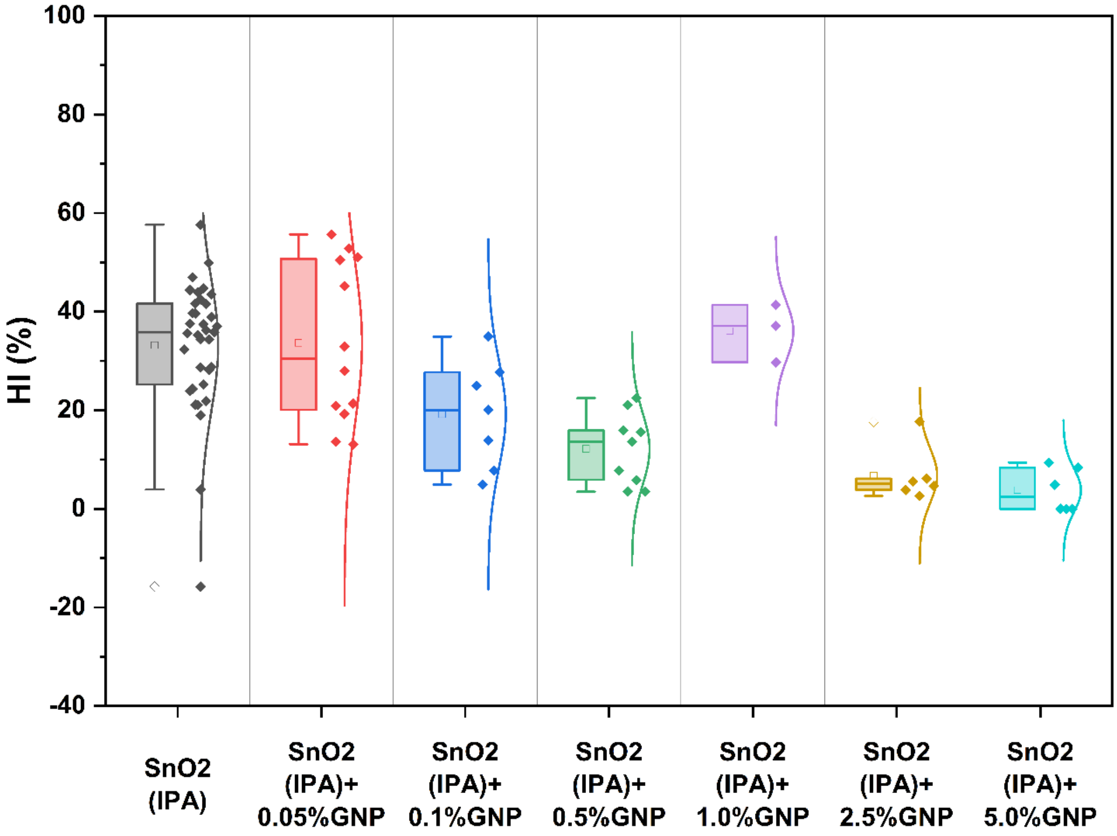

Figure 33: Graphic presentation of HI by box plot statistics and distribution curve for experiments of Group 2 with SnO_2 (IPA) containing different levels of GNP extracted from the JV curves of devices under 1 Sun illumination.

Source: Prepared by the author.

Table 9 shows that 0.05% of GNP obtained a real PCE of 7.2 ± 1.2%, slightly below the values obtained in the backward direction (8.6 ± 1.2%), while the control sample shows a sharper reduction of 2.7%. In addition, this sample had a record of 10% PCE. Even though it is a value outside the confidence limit, it is believed that this result indicates that it is possible to improve the performance of devices with proper deposition optimization, such as thickness control. Such results evidence the need to develop solutions for incorporating graphene in the ETL layers and optimize the layers performed concerning thickness and deposition conditions.

The HI also tends to decrease as the graphene concentration increases, except for samples with 0.05% and 1.0% GNP. It is believed that because the average PCE value has reduced, the small absolute variations of the average value of the backward and forward curves generate a higher percentage value. For example: in a hypothetical case that device A has 40% (B) and 30% (F) efficiency, while sample B has 10% (B) and 20% (F). The HI for sample A would be 25%, while for sample B, it would be 50%. Even though both present a 10% absolute difference between backward and forward efficiency, the sample with the lowest efficiency value (B) represents a more drastic percentage variation. It demonstrates the limitations of HI in percentage terms. It is believed that the HI expressed as a percentage is a qualitative way of interpreting the results, facilitating their interpretation. However, the quantitative verification in absolute terms is interesting in some cases.

Table 9: Real PCE and HI data for experiments from Group 2 with SnO_2 (IPA) containing different levels of GNP extracted from the JV curves of devices under 1 Sun illumination, represented in terms of [mean ± 99% confidence limit (best)].

	Real PCE (max) [%]	**HI (|min|) [%]**
SnO_2 (IPA)	13.4 ± 0.8 (15.7)	35.3 ± 4.6 (-11.1*)
SnO_2 (IPA)+ 0.05%GNP	7.2 ± 1.2 (10*)	33.7 ± 13.8 (13.1)
SnO_2 (IPA)+ 0.1%GNP	5.0 ± 1.2 (5.9)	19.2 ± 13.4 (4.9)
SnO_2 (IPA)+ 0.5%GNP	1.2 ± 1.1 (3.3)	12.2 ± 7.4 (3.4)
SnO_2 (IPA)+ 1.0%GNP	1.4 ± 0.4 (1.6)	36.1 ± 16.2 (29.7)
SnO_2 (IPA)+ 2.5%GNP	0.6 ± 0.5 (1.3*)	6.7 ± 7.6 (2.6)
SnO_2 (IPA)+ 5.0%GNP	0.2 ± 0.2 (0.4)	7.5 ± 6.1 (0)

* Data presented outside the limit established by the box plot of 1.5 IQR, being considered invalid (outlier).

Source: Prepared by the author.

Based on the evaluation of the JV curves of the samples with the highest real PCE values, shown in Figure 34, the previous discussions can be confirmed. The curves present the value in the intercept of the ordinate's axis similar to each other. Also, there is a visible reduction of J_{sc}, only from 1.0%. Meanwhile, the intercept on the abscissa axis has changed even from the lowest levels of GNP. In addition, it can be confirmed that the device with 0.05% graphene holds a significant variation, mainly in V_{oc}, concerning the scanning direction, corroborating that the HI result expressed as a percentage is consistent with reality. Another aspect is that from 1.0% filler, the JV curves of the devices resemble a straight line, a short-circuit characteristic of the device due to the linear behavior of current as a function of voltage, known as Ohm's law. Its efficiency results are also less than 2.0%, demonstrating that these contents do not generate significant energy conversion effects under these conditions. The devices performed as initial tests with a content of 10, 25, 50, 75, and 90% GNP also presented a short circuit or non-contact profile (horizontal straight line) showing no efficiency as a measurement response. Even so, the results were very satisfactory, demonstrating the possibility of optimization.

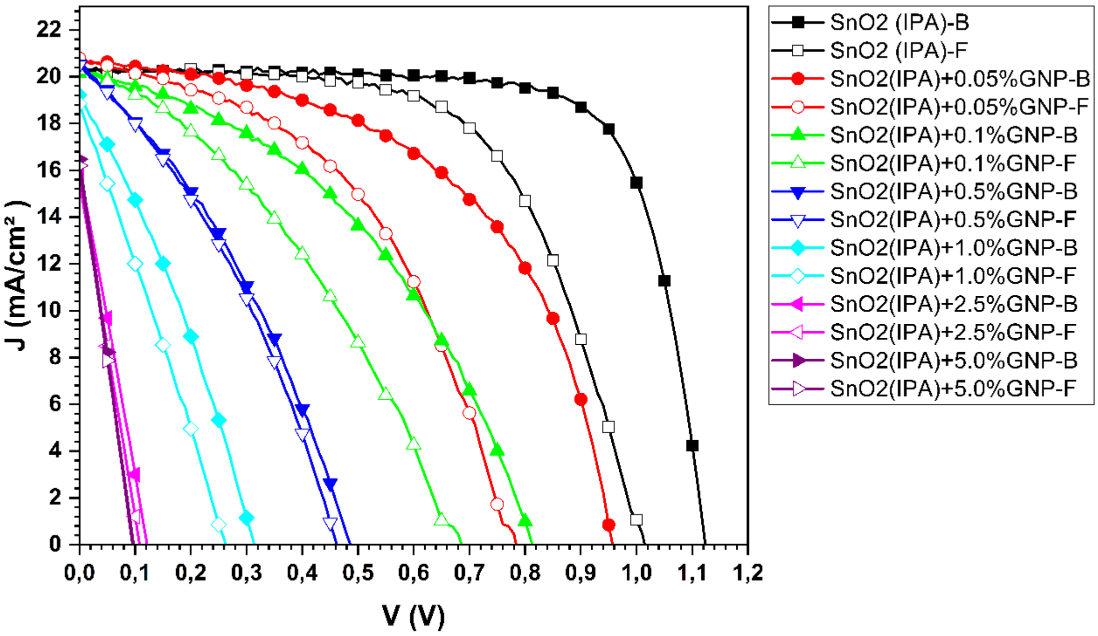

Figure 34: JV curve of the highest real PCE for experiments of Group 2 devices with SnO_2 (IPA) containing different levels of GNP experiments under 1 Sun illumination.

Source: Prepared by the author.

4.3 GROUP 3: SnO_2 (H_2O) + GNP

In the third section of the present work, the results related to combining the most promising GNP contents with the precursor from the dispersion of colloidal SnO_2 nanoparticles are presented. The selected graphene compositions were: 0.05%, which had the most promising performance, with subsequent levels of 0.5% and 2.5%, to perform a more comprehensive mapping. Figure 35 shows the open-circuit voltage results. Again, 0.05% GNP performed better, and the graphene content tends to reduce V_{oc}. There was also an increase in data dispersion on these devices. In addition, 2.5% filler already makes the device practically inefficient, with V_{oc} close to zero.

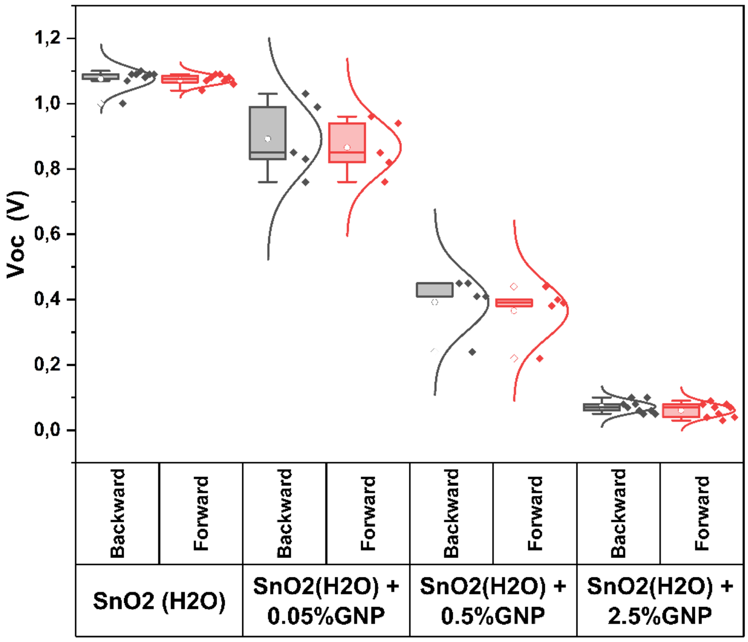

Figure 35: Graphic presentation of V_{oc} by box plot statistics and distribution curve for experiments of Group 3 with SnO_2 (H_2O) containing different levels of GNP extracted from the JV curves of devices under 1 Sun illumination.

Source: Prepared by the author.

The short-circuit current density, in Figure 36, shows a slight increase in the mean and median with 0.05% of GNP concerning the control devices. With 0.5% of graphene, there is also the preservation of J_{sc}, while the content is reduced to approximately 15 mA/cm^2. Furthermore, there is a great similarity between backward and forward scans.

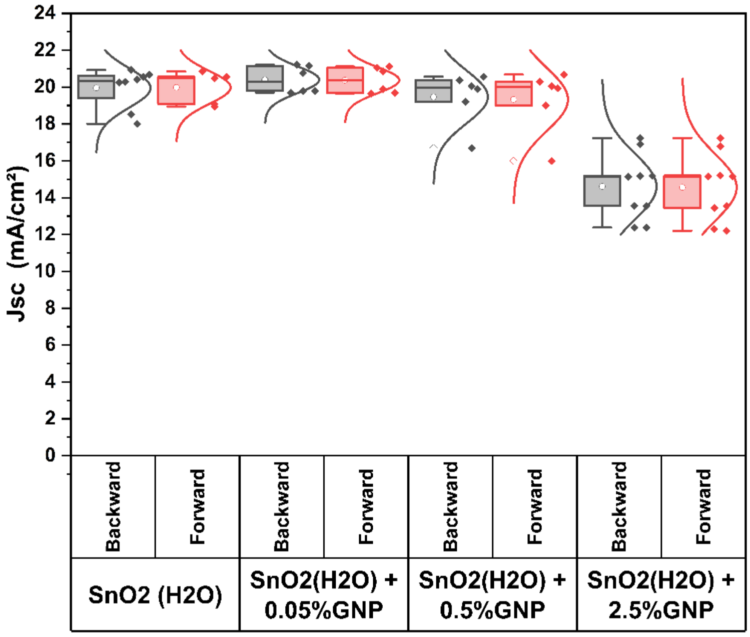

Figure 36: Graphic presentation of V_{oc} by box plot statistics and distribution curve for experiments of Group 3 with SnO_2 (H_2O) containing different levels of GNP extracted from the JV curves of devices under 1 Sun illumination.

Source: Prepared by the author.

As seen in Table 10, all samples exhibited remarkable similarities in the data concerning the directions of the sweep, as observed in the box plot plots. In addition, it shows the increase in the average and the best value of J_{sc} with 0.05% GNP. For this concentration, the precursors by the colloidal dispersions of nanoparticles and by the $SnCl_4$ (SnO_2 (IPA)) solutions, observed in section 2, presented statistically equal values. However, the sample SnO_2 (H_2O)+ 0.05%GNP had a smaller difference in the value B–F. As for 0.5% GNP, the tin tetrachloride isopropanol sample had the V_{oc} reduced to approximately 0.2 V, while for the colloidal dispersion, it presented twice the value, 0.39±0.14 V. J_{sc} also displayed improvement for the SnO_2 devices (H_2O)+ 0.5%GNP with values around 19.47 ± 1.99 (B) and 19.33 ± 2.38 (F) compared to 17.59 ± 2.56 (B) and 17.36 ± 2.73 (F) mA/cm^2 for SnO_2 (IPA)+0.5%GNP. Both precursors at 2.5% concentration showed inefficient devices with V_{oc} close to null.

It is believed that colloidal dispersions already have a higher surface area than the $SnCl_4$ precursor. Thus, the insertion of graphene, although representing a heterogeneity in the volume of the thin film, does not generate a significant variation in the amount of surface area. In addition, nanoparticles have lower hysteresis due to better interface and charge extraction, suppressing the deleterious effects of graphene nanosheets in generating new surfaces. It is worth mentioning that in the 1.5 IQR test, the best V_{oc} (F) for 0.5% of GNP is an outlier; however, this value is not discarded as non-standard since it is also in the central region of the distribution curve and within the 99% confidence limit.

Table 10: V_{oc} and J_{sc} data for experiments of Group 3 with SnO_2 (H_2O) containing different levels of GNP extracted from the JV curves of devices under 1 Sun illumination, represented in terms of [mean ± 99% confidence limit (best)].

	V_{oc} (max) [V]		**J_{sc} (max) [mA/cm^2]**	
	Backward	**Forward**	**Backward**	**Forward**
SnO_2 (H_2O)	1.08 ± 0.04 (1.1)	1.07 ± 0.03 (1.09)	19.96 ± 1.19 (20.93)	19.98 ± 1.45 (20.85)
SnO_2 (H_2O)+ 0.05%GNP	0.89 ± 0.18 (1.03)	0.87 ± 0.13 (0.96)	20.4 ± 0.99 (21.21)	20.38 ± 0.97 (21.12)
SnO_2 (H_2O)+ 0.5%GNP	0.39 ± 0.14 (0.45)	0.37 ± 0.14 (0.44)	19.47 ± 1.99 (20.57)	19.33 ± 2.38 (20.68)
SnO_2 (H_2O)+ 2.5%GNP	0.07 ± 0.02 (0.1)	0.06 ± 0.02 (0.09)	14.61 ± 1.82 (17.24)	14.56 ± 1.85 (17.24)

Source: Prepared by the author.

The fill factor, Figure 37, of this set of samples from Group 3 presents similar behavior to V_{oc}. For samples with the precursor SnO_2 (IPA), the behavior of FF is similar to J_{sc}. As the graphene concentration increases, there is a gradual reduction in this parameter. In addition, the lower content of GNP already significantly reduces the FF. Graphene tends to make it difficult to extract charges and favor recombination (MENG *et al.*, 2018).

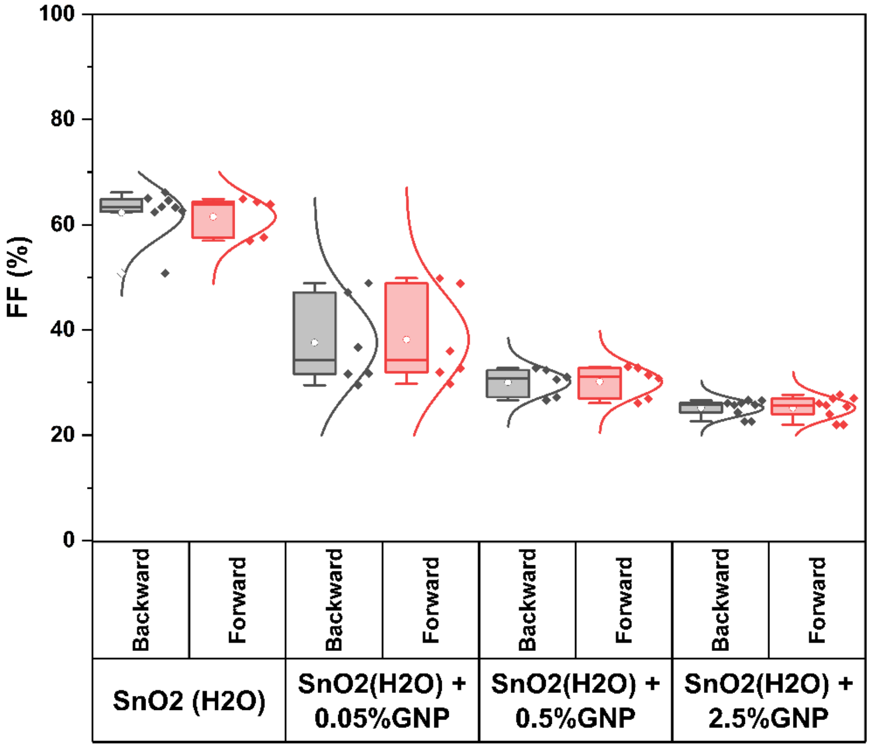

Figure 37: Graphic presentation of FF by box plot statistics and distribution curve for experiments of Group 3 with SnO_2 (H_2O) containing different levels of GNP extracted from the JV curves of devices under 1 Sun illumination.

Source: Prepared by the author.

The energy conversion efficiency, shown in Figure 38, also presents similar behavior to the FF and V_{oc} curves. The PCE reduction appears to be even more intense, and with only 0.05% of GNP, there is also a significant increase in data dispersion. On the other hand, the difference between the backward and forward results is very small.

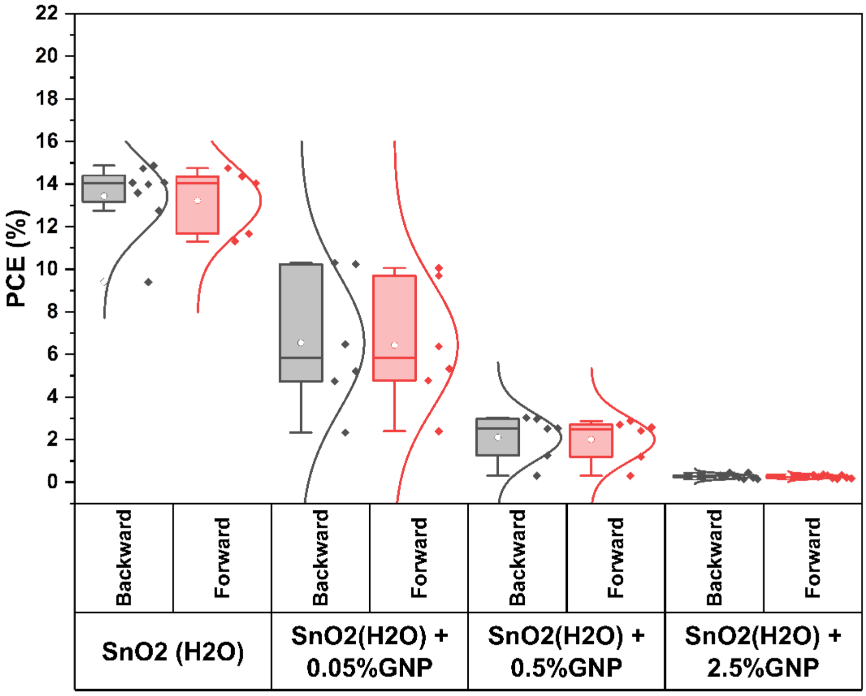

Figure 38: Graphic presentation of PCE by box plot statistics and distribution curve for experiments of Group 3 with SnO_2 (H_2O) containing different levels of GNP extracted from the JV curves of devices under 1 Sun illumination.

Source: Prepared by the author.

In Table 11, it is possible to compare the results more easily concerning the modifications used. Devices prepared from SnO_2 (H_2O) and SnO_2 (IPA) resulted in statistically similar FF values concerning GNP contents; only the result with 0.05% filler in the backward scanning direction was slightly higher (47 ± 3 (53)). On the other hand, the efficiency results of the devices do not present very significant statistical differences. Only SnO_2 (IPA) +0.05%GNP (B) devices have a higher PCE, of 8.6 ± 1.2 (11.1) for the other scans and concentrations, the samples with SnO (H_2O) showed a slightly higher average. Nevertheless, as mentioned, statistically, all samples compared at the same levels show coincidence in the 99% confidence interval.

Table 11: FF and PCE data for experiments of Group 3 with SnO_2 (H_2O) containing different levels of GNP extracted from the JV curves of devices under 1 Sun illumination, represented in terms of [mean ± 99% confidence limit (best)].

	FF (max) [%]		**PCE (max) [%]**	
	Backward	**Forward**	**Backward**	**Forward**
SnO_2 (H_2O)	62 ± 5 (66)	62 ± 6 (65)	13.4 ± 2 (14.9)	13.2 ± 2.6 (14.8)
SnO_2 (H_2O)+ 0.05%GNP	39 ± 13 (49)	40 ± 14 (50)	6.6 ± 4.4 (10.3)	6.4 ± 4.1 (10.1)
SnO_2 (H_2O)+ 0.5%GNP	30 ± 4 (33)	30 ± 4 (33)	2.1 ± 1.5 (3)	2 ± 1.4 (2.9)
SnO_2 (H_2O)+ 2.5%GNP	25 ± 2 (27)	25 ± 2 (28)	0.3 ± 0.1 (0.4)	0.3 ± 0.1 (0.4)

Source: Prepared by the author.

The real PCE exposed in Figure 39 corroborates the previous results. Inserting GNP tends to reduce the efficiency of these devices and still increases data dispersion with 0.05% GNP. The PCE distribution curves are symmetrical, with the mean and median very close. Furthermore, it is believed that spreading graphene nanoplatelets in SnO_2 nanoparticle dispersions would be like mixing two solids in a liquid (solvent). It is more difficult than dispersing graphene in a solution of a solubilized salt ($SnCl_4$) (IPA). Therefore, the slight attenuation of some properties while increasing its dispersion may be due to the generation of agglomerates added to the emergence of new surfaces in the dispersion of nanoparticles, which hinders the extraction and efficient conduction of electrons.

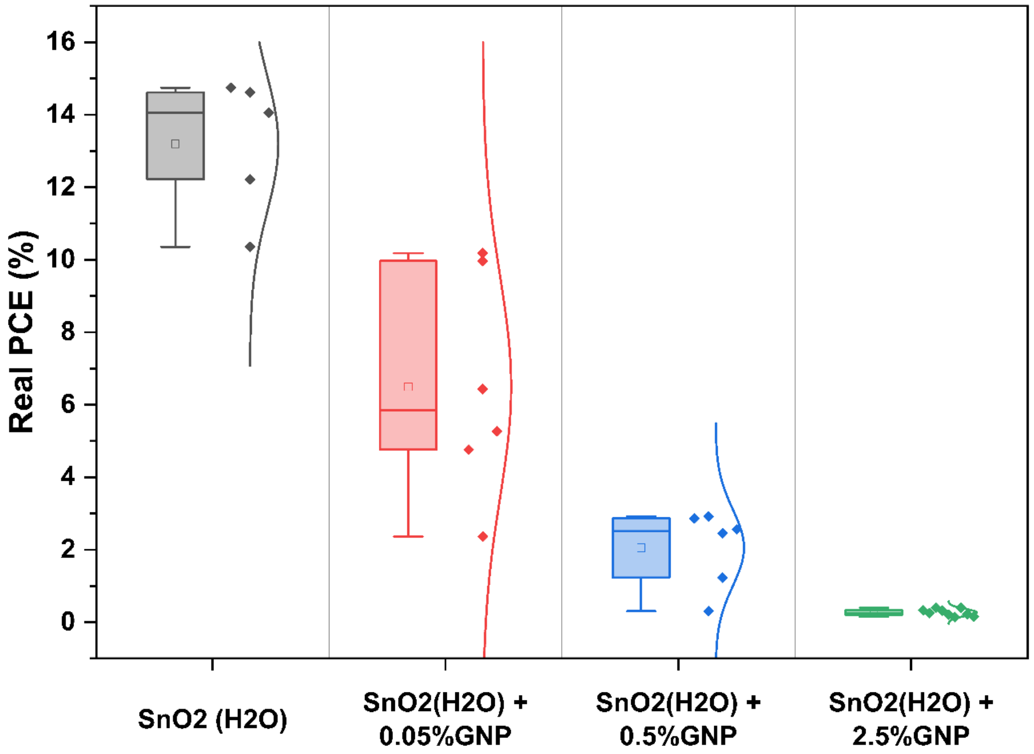

Figure 39: Graphic presentation of real PCE by box plot statistics and distribution curve for experiments of Group 3 with SnO_2 (H_2O) containing different levels of GNP extracted from the JV curves of devices under 1 Sun illumination.

Source: Prepared by the author.

In Figure 40, it is possible to observe that the mean and median values of the hysteresis do not show variation with the increase of the GNP content. The SnO_2 (H_2O)+ 2.5%GNP sample greatly increases data dispersion. The dispersion of graphene at this concentration is probably hampered, which can generate aggregates, increasing heterogeneity and HI.

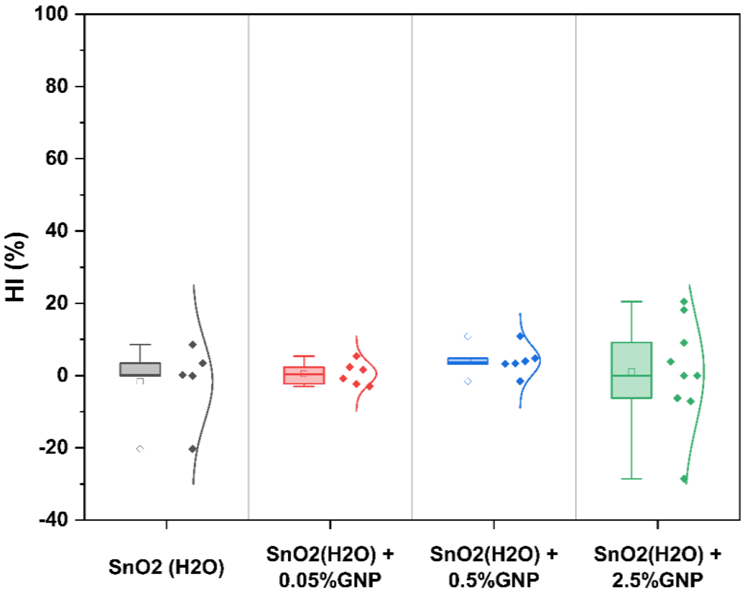

Figure 40: Graphic presentation of HI by box plot statistics and distribution curve for experiments of Group 3 with SnO_2 (H_2O) containing different levels of GNP extracted from the JV curves of devices under 1 Sun illumination.

Source: Prepared by the author.

In Table 12, it can be perceived the results of real PCE and HI. The samples from the precursor SnO_2 (H_2O) and SnO_2 (IPA) display great coincidence in the 99% confidence interval. That is, the data are statistically similar. The most promising nanocomposite among those analyzed up to this section would be SnO_2 (IPA)+ 0.05%GNP. The SnO_2 (IPA)+ 0.05%GNP devices, which obtained 7.2 ± 1.2% (10%*), coincidentally throughout the 99% confidence interval of SnO_2 (H_2O)+ 0.05%GNP, and the best devices also have around 10% efficiency. The big difference would be that the hysteresis of the samples prepared from the colloidal dispersion of SnO_2 nanoparticles was almost zero, in contrast to SnO_2 (IPA)+ 0.05%GNP, which presented hysteresis around 33.7 ± 13.8. They exhibited a statistically similar real PCE but with better performance concerning hysteresis.

Table 12: Real PCE and HI data for experiments of Group 3 with SnO_2 (H_2O) containing different levels of GNP extracted from the JV curves of devices under 1 Sun illumination, represented in terms of [mean ± 99% confidence limit (best)].

	Real PCE (max) [%]	**HI (|min|) [%]**
SnO_2 (H_2O)	13.2 ± 3.0 (14.7)	4 ± 17.7 (0)
SnO_2 (H_2O)+ 0.05%GNP	6.5 ± 4. 2(10.2)	3.1 ± 4.4 (-3)
SnO_2 (H_2O)+ 0.5%GNP	2.1 ± 1.5 (2.9)	5.2 ± 5.5 (-1.6)
SnO_2 (H_2O)+ 2.5%GNP	0.3 ± 0.1 (0.4)	12.9 ± 15.1 (-28.6)

Source: Prepared by the author.

The JV curves in Figure 41 enable observing the curves' similarity concerning the backward and forward scanning directions. Even the hysteresis is corroborated with the similarities in the intercepts on the x and y axes. From 0.5% of GNP, the curves are similar to straight lines, which are short-circuited and inefficient. This effect is more evident in SnO_2 (IPA) samples with 1.0% of GNP. Based on this, it is believed that it is easier to disperse graphenes in solutions of $SnCl_4$ salt in IPA than in colloidal dispersions of nanoparticles.

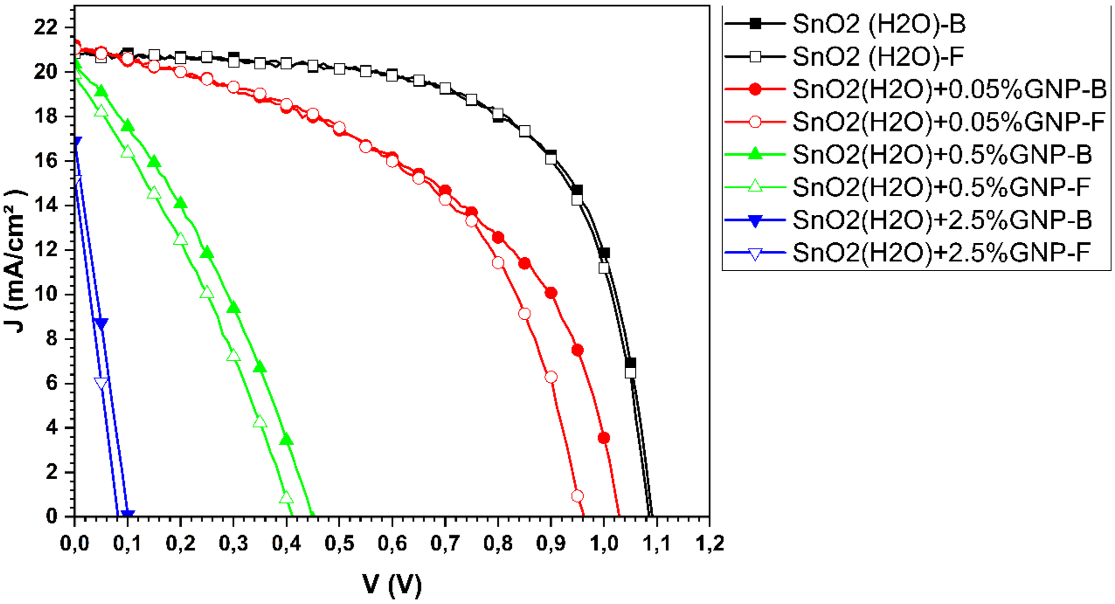

Figure 41: JV curve of the highest real PCE Group 3 devices for experiments with SnO_2 (H_2O) containing different levels of GNP experiments under 1 Sun illumination.

Source: Prepared by the author.

4.4 GROUP 4: DOUBLE LAYER OF SnO_2 (IPA) + GNP

Based on the results of the previous sections, two concentrations of GNP were selected to carry out the double layer (DL) experiments as a proposal for a solution to improve the performance of the devices due to the incorporation of graphene. The content of 0.05% was chosen due to the best results in both Groups 2 and 3, with precursors from $SnCl_4$ and nanoparticles from colloidal SnO_2, respectively. For the preparation of the double layers, the SnO_2 (IPA)-based devices precursor was chosen since it would be the most suitable to obtain better dispersion of graphene nanosheets, even at the highest concentration.

The experiments were organized to make it possible to evaluate the interface of the ETL with the transparent conductive electrode and the ETL with the active layer of perovskite. When preparing the devices with the glass/FTO/compact-ETL1

(SnO_2(IPA))/ETL2(SnO_2(IPA)+GNP)/perovskite/HTL/Au architecture, the nanocomposite is in direct contact with the active layer, and it is possible to evaluate its influence on the perovskite. In the inverted bilayer structure of the glass/FTO/ETL1(SnO_2 (IPA)+GNP)/compact-ETL2(SnO_2 (IPA))/perovskite/HTL/Au, it can be verified that the influence related to the contact of the nanocomposite with the conductive transparent electrode. It is interesting to produce devices that have good interactions in both interfaces. Thus, with these experiments, it can also be suggested which of the two interfaces would be more harmed due to the insertion of the heterogeneities of the graphene nanoplatelets (XIONG *et al.*, 2018).

Experiments were also carried out on the dispersion of solutions containing only graphene in isopropanol over compact ETL of SnO_2 (IPA). This sample represents the extreme situation due to using pure graphene as an interfacial layer between ETL and perovskite. Such an area in the literature is graphene for interface engineering in solar cells. AGRESTI et al., 2016) reported that applying graphene between the charge-carrying layers, ETL or HTL, can improve the stability of the devices. However, this layer can impair the performance of solar modules because graphene is a nanoparticle that tends to agglomerate vertically. Its particles do not coalesce or sinter horizontally, forming continuous homogeneous films, but the re-stacking process occurs. And as in graphene, collapsing nanosheets reduce their optoelectronic properties, making the layer opaque or even electrically insulating.

The formation of interfacial layers of graphene drastically depends on the concentration, processing conditions, morphology of the nanosheets and the generated layer, orientation and dispersion of graphene under the surface, type of graphene, graphene functionalization, energy levels of the HOMO and LUMO orbitals, Fermi level, or, for the metallic behavior, its work function, charge mobility and transparency (AGRESTI *et al.*, 2016; ZHAO, Xiaojuan *et al.*, 2018). The preparation of the graphene layer between the FTO and the ETL will not be presented because, when performing such experiments, the deposition of $SnCl_4$ in isopropanol mostly removed the graphene structure deposited on the FTO. In other words, from the point of view of reproducibility, it was possible to observe that among the prepared films, the total removal of graphene would occur or generate films that differed from each other, which is not interesting for such an application. The same would occur when trying to perform KCl treatment on graphene layers.

The control device used is the SnO_2 (IPA) samples already presented. That is because doubling the concentration would have a similar impact on producing ETLs layers similar in thickness to double layer experiments but would rule out the problem of inserting one more interface between ETL1 and ETL2 of pure SnO_2. As observed in the experiments for SnO_2 (IPA) 0.1M, there is a significant reduction in the efficiency of the devices. This way, the parameter to be mirrored would be the simplest and best-performing device. In addition, it is expected that a compact double layer of pure SnO_2 is not interesting to be tested because it adds an interface. Also, according to the works in the literature, it is known that the optimized thickness of this ETL is around 30 nm, as the procedure is already used for SnO_2 (IPA) devices (CUI *et al.*, 2020; XIONG *et al.*, 2018).

Figure 42 shows the boxplot of V_{oc} data from the double layer experiments. It can be seen that concentrations of 2.5% in both systems generate low open-circuit voltages. In comparison, the compact layer of GNP as an interfacial carbon layer between perovskite and the compact ETL of SnO_2 (IPA) also drastically diminished this property. At concentrations of 0.05% in both systems, it is evident that there is no change in V_{oc} in the forward scan compared to the control. As for the back scan, there is an increase in data dispersion and a slight reduction in the mean and median values, but still a coincidence in the safety intervals between the limits established by 1.5 IQR. That is, statistically, the experiments present very similar or close values to each other when describing V_{oc}.

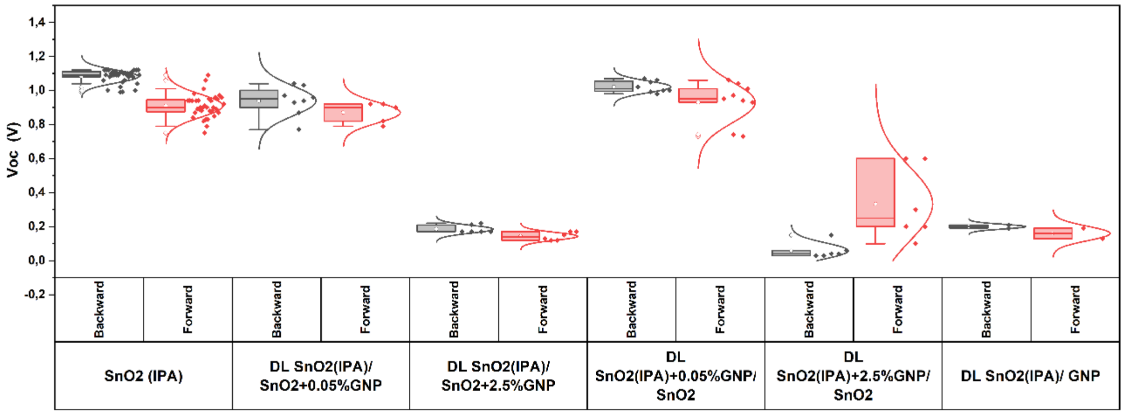

Figure 42: Graphic presentation of V_{oc} by box plot statistics and distribution curve for experiments of Group 4 with the double layer with SnO_2 (IPA) containing different levels of GNP extracted from the JV curves of devices under 1 Sun illumination.

Source: Prepared by the author.

The results of the short-circuit current density in the box plot are shown in Figure 43. The double layer systems with 0.05% GNP did not present significant efficiency variation concerning the control devices. Devices that had the nanocomposite on top of the compact layer showed higher J_{sc} results than the DL SnO_2 (IPA) +2.5%GNP/SnO_2 system. It may indicate that the interface between the FTO is more impaired than the interface with perovskite due to the presence of graphene. On the other hand, the pure graphene system on the compact layer of SnO_2 presented an intersection with the safety intervals of the layer's data with nanocomposite on top. Based on this, it can be suggested that graphene has reduced the devices' properties by disturbing the contact with the transparent conductive electrode. Thus, the electrons may be extracted efficiently from the active layer, but they are captured by the traps on the graphene surface close to the FTO.

BICCARI *et al.* (2017) compared four different combinations of GO, functionalized with lithium or not, as mesoporous titanium dioxide ETLs ($mTiO_2$) and GO-Li as an interfacial layer. The main architectures prepared were: (1) $mTiO_2$, (2) mixing $mTiO_2$ with GO as ETL, (3) $mTiO_2$ with GO on top, and (4) mixing GO and $mTiO_2$ in ETL with GO-Li intercalator. In ETL devices, faster photoluminescence decays by excitation were observed on the FTO side compared to the $MAPbI_3$ perovskite side, which is explained by the efficient removal of electrons from the $MAPbI_3$ layer due to ETL. That is, contact with FTO can be disrupted if there are voids at the electrode interface with the ETL. Such voids can be generated when graphene is spread over the FTO. The nanoplatelets generate free volume because they cannot form compact and continuous thin films due to their behavior as solid particles that do not sinter or coalesce horizontally.

Furthermore, the $MAPbI_3$ layer embedded in GO+$mTiO_2$ plus GO-Li on top of the ETL shows much better crystalline quality than the other samples, including the control device, with a trap density about an order of magnitude lower. Finally, the results show that graphene-based ETLs significantly improve carrier collection and the crystalline quality of the active layer material. It is also worth mentioning that the application of GO in the interfacial layer with perovskite was only possible after its functionalization with lithium, while dispersion with TiO_2 was no longer necessary, although it also improves the efficiency of the device (BICCARI *et al.*, 2017a; HAN *et al.*, 2015). In addition, increasing the graphene concentration also tends to reduce the films' transparency, reducing the incidence of photons in the active layer. Thus, the reduction of J_{sc} may also be related to the lower incidence of photons due to graphene's absorption and scattering of light.

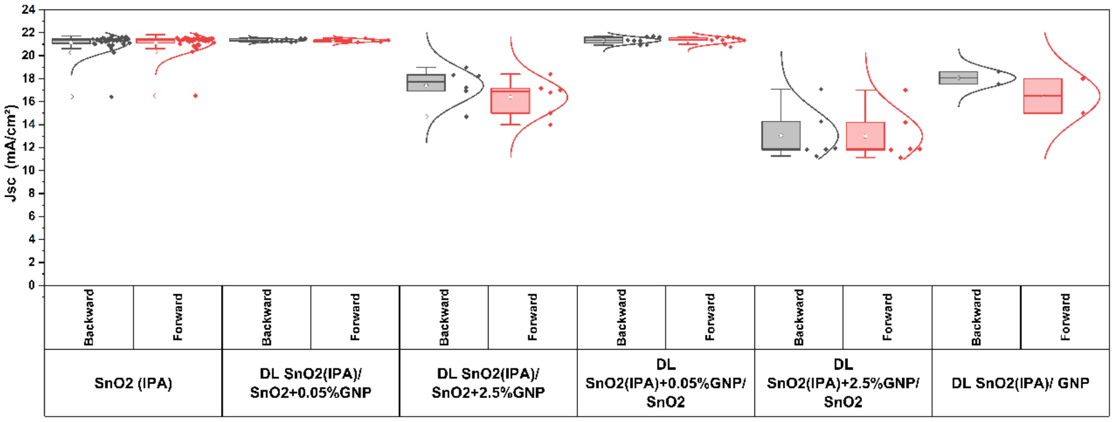

Figure 43: Graphic presentation of J_{sc} by box plot statistics and distribution curve for experiments of Group 4 with the double layer with SnO_2 (IPA) containing different levels of GNP extracted from the JV curves of devices under 1 Sun illumination.

Source: Prepared by the author.

Table 13 displays the data with their respective 99% confidence limits. As mentioned, there is a slight decrease in Voc due to the insertion of 0.05% GNP in both systems. It is worth noting that the nanocomposite under the compact ETL with 0.05% GNP, that is, in contact with the FTO, presented mean and maximum V_{oc} values slightly higher than the DL SnO_2 (IPA)/SnO_2+0.05%GNP system. Furthermore, it is observed that the double layers with this low GNP concentration slightly increased the short-circuit current density concerning the control device. It may suggest that the GNP can also trap the light that passes through the ETL inside the device, redirecting the photons reflected by the active layer itself, thus increasing the photocurrent (LEE, Yoon Ho *et al.*, 2020). Another theory would be that GNP can improve the crystallinity of the CsMAFA perovskite or increase the electrical conductivity of the ETL by increasing the photocurrent extracted from the active layer (BICCARI *et al.*, 2017b). In the 1.5 IQR test, the best V_{oc} (F) for 2.5% of GNP is an outlier; however, this value is not discarded as non-standard since it is also near the central region of the distribution curve and within the 99% confidence limit. It is also worth noting that the devices with 0.05% graphene had a higher average V_{oc} and J_{sc} than those with a similar theoretical thickness (SnO_2 (IPA) 0.1M).

Table 13: V_{oc} and J_{sc} data for experiments of Group 4 with the double layer with SnO_2 (IPA) containing different levels of GNP extracted from the JV curves of devices under 1 Sun illumination, represented in terms of [mean ± 99% confidence limit (best)].

	V_{oc} (max) [V]		**J_{sc} (max) [mA/cm^2]**	
	Backward	**Forward**	**Backward**	**Forward**
SnO_2 (IPA)	1.08 ± 0.02	0.91 ± 0.03	21.14 ± 0.39	21.15 ± 0.39
	(1.12)	(1.09*)	(21.72)	(21.82)
DL SnO_2 (IPA)/ SnO_2+0.05%GNP	0.94 ± 0.1	0.87 ± 0.10	21.35 ± 0.14	21.32 ± 0.23
	(1.04)	(0.92)	(21.51)	(21.53)
DL SnO_2 (IPA)/ SnO_2 +2.5%GNP	0.19 ± 0.03	0.14 ± 0.03	17.4 ± 2.11	16.40 ± 2.21
	(0.22)	(0.17)	(18.97)	(18.40)
DL SnO_2 (IPA) + 0.05%GNP/SnO_2	1.02 ± 0.04	0.93 ± 0.12	21.34 ± 0.33	21.35 ± 0.30
	(1.07)	(1.06)	(21.69)	(21.66)
DL SnO_2 (IPA) +2.5%GNP/SnO_2	0.06 ± 0.06	0.33 ± 0.3	13.04 ± 3.10	12.98 ± 3.09
	(0.15)	(0.6)	(17.09)	(17.02)
DL SnO_2 (IPA)/GNP	0.20 ± 0.07	0.16 ± 0.21	18.07 ± 3.79	16.50 ± 10.53
	(0.21)	(0.19)	(18.61)	(18.00)

Source: Prepared by the author.

In Figure 44, it is possible to observe the box plot plots for the fill factor of the double layer experiments. These results behave similarly to the V_{oc} of these samples. The double layers with 0.05% GNP slightly reduced their open-circuit voltage values, while with 2.5% graphene, it reduced dramatically. The graphene layer on top of the compact SnO_2 (IPA) also generated inefficient devices with a high recombination rate. It is believed that graphene tends to increase recombination processes as it inserts surfaces that act as traps for charge carriers, increasing recombination.

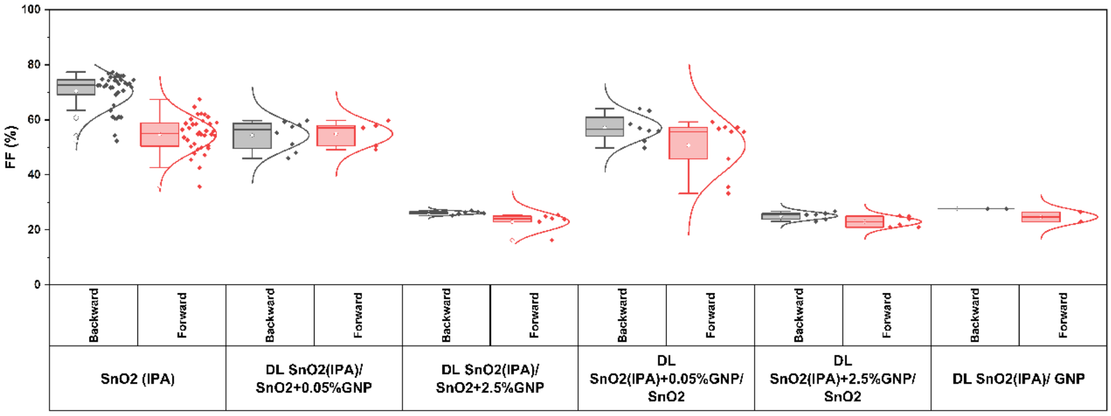

Figure 44: Graphic presentation of FF by box plot statistics and distribution curve for experiments of Group 4 with the double layer with SnO_2 (IPA) containing different levels of GNP extracted from the JV curves of devices under 1 Sun illumination.

Source: Prepared by the author.

The efficiency of the devices shown in Figure 45 demonstrates a high coincidence between the double layer samples with 0.05% graphene, mainly in relation to forward scanning. As with the pure GNP layer over the ETL, high concentrations of graphene generated inefficient devices regardless of the architecture employed. Possibly with high contents of nanoplatelets, there is an increased probability of clusters that also reduce the properties of solar modules. In addition, 2.5% of GNP increases the number of interfaces between SnO_2 and the carbon material, generating more recombination centers.

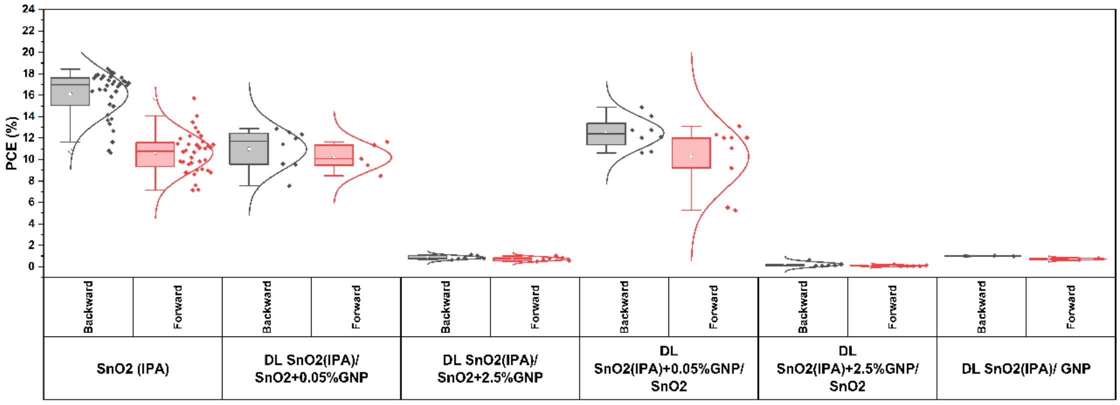

Figure 45: Graphic presentation of PCE by box plot statistics and distribution curve for experiments of Group 4 with the double layer with SnO_2 (IPA) containing different levels of GNP extracted from the JV curves of devices under 1 Sun illumination.

Source: Prepared by the author.

Table 14 shows that the FF significantly reduces the mean values and the 99% confidence interval due to the insertion of graphene. As already mentioned, this may occur due to increased surfaces inside the more perfect crystalline structure of SnO_2. The same occurs with PCE, which decays from approximately 16.1% (reference) to 11.0% (DL SnO_2 (IPA)/SnO_2+0.05%GNP) and 12.5%(DL SnO_2 (IPA) + 0.05%GNP/ SnO_2) in the backward scan. However, it is observed that the difference between the energy conversion efficiency and the FF between forward and reverse scanning is drastically reduced due to the insertion of graphene.

It is worth remembering that SnO_2 (IPA) 0.1M obtained PCE values of 9.4±3 (15.2)% (B) and 8.2±2.2 (12.2)% (F). The double layer strategy is interesting when incorporating 0.05% of GNP, significantly improving the average values in both scans. Furthermore, the incorporation of GNP by direct mixing with the precursor $SnCl_4$, a sample known as SnO_2 (IPA) + 0.05%GNP, resulted in PCE 8.6 ± 1.2% (11.1%) (B) and 5.8 ± 1.5% (8.8%) (F). In other words, applying the double layer is a very attractive solution to improve the PCE due to the incorporation of graphene. This alternative proved superior to the SnO_2 (H_2O) mixtures + 0.05% GNP, reaching efficiencies close to 6.5% in both scanning directions. Still, it is worth mentioning that the DL SnO_2 (IPA) + 0.05%GNP/SnO_2 presented an average performance slightly superior to the nanocomposite layer on top of the compact ETL.

Table 14: FF and PCE data for experiments of Group 4 with the double layer with SnO_2 (IPA) containing different levels of GNP extracted from the JV curves of devices under 1 Sun illumination, represented in terms of [mean ± 99% confidence limit (best)].

	FF (max) [%]		**PCE (max) [%]**	
	Backward	**Forward**	**Backward**	**Forward**
SnO_2 (IPA)	70 ± 3 (77)	55 ± 3 (67*)	16.1 ± 1.0 (18.5)	10.6 ± 0.9 (15.7)
DL SnO_2 (IPA)/ SnO_2+0.05%GNP	54 ± 6 (60)	55 ± 8 (60)	11 ± 2.1 (12.9)	10.2 ± 2.1 (11.7)
DL SnO_2 (IPA)/ SnO_2 +2.5%GNP	26 ± 1 (27)	23 ± 5 (25)	0.9 ± 0.3 (1.1)	0.7 ± 0.3 (1)
DL SnO_2 (IPA) + 0.05%GNP/SnO_2	57 ± 5 (64)	51 ± 10 (59)	12.5 ± 1.6 (14.9)	10.3 ± 3 (13.1)
DL SnO_2 (IPA) +2.5%GNP/SnO_2	25 ± 2 (27)	23 ± 3 (25)	0.2 ± 0.3 (0.7)	0.1 ± 0.1 (0.2)
DL SnO_2 (IPA)/GNP	28 ± 0 (28)	25 ± 12 (27)	1 ± 0.1 (1)	0.7 ± 0.5 (0.8)

* Data presented outside the limit established by the box plot of 1.5 IQR, being considered invalid (outlier).

Source: Prepared by the author.

The real PCE results, shown in Figure 46, demonstrate similar box plot behavior of backward and forward PCE. However, the double layers with 0.05% were closer to the reference value. The dataset validated by the 1.5 IQR withdrawal period of the reference devices almost entirely contains the real PCE dataset of the double layer results with 0.05% GNP. Furthermore, 50% of the data (median and 50% of the data above) of the DL SnO_2 (IPA) + 0.05%GNP/SnO_2 is contained in the 50% range of the reference sample (between the median, which separates the set in the middle, and the lower limit IQR). That is, statistically, these samples present high similarity and can be considered statistically coincident. The DL SnO_2 (IPA)/SnO_2+0.05%GNP sample coincides with at least 25% of its valid real PCE results below Q1.

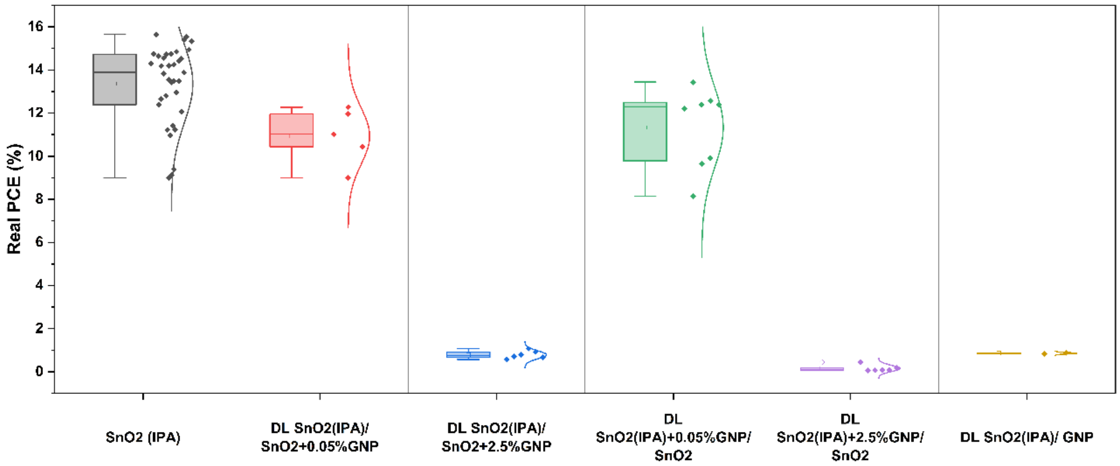

Figure 46: Graphic presentation of Real PCE by box plot statistics and distribution curve for experiments of Group 4 with the double layer with SnO_2 (IPA) containing different levels of GNP extracted from the JV curves of devices under 1 Sun illumination.

Source: Prepared by the author.

As for the hysteresis index, in Figure 47, there is a significant reduction due to the implementation of the double layer as a strategy for incorporating GNP. That is, there is a much smaller difference in the efficiency of the devices concerning the scanning directions. It corroborates the great coincidence between the scan directions and improvement of real PCE with the incorporation of 0.05% of GNP. The results of the nanocomposites between the compact ETL and the perovskite layer exhibited a lower dispersion.

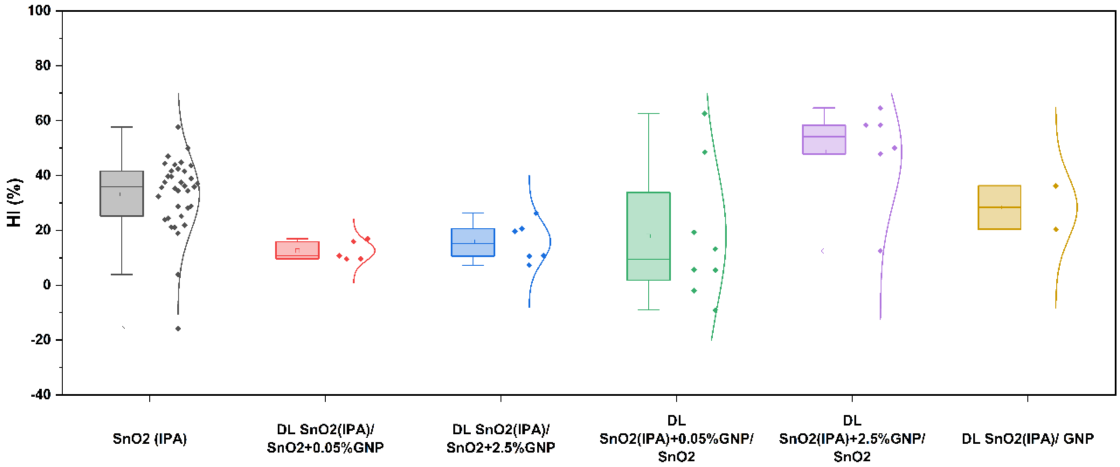

Figure 47: Graphic presentation of HI by box plot statistics and distribution curve for experiments of Group 4 with the double layer with SnO_2 (IPA) containing different levels of GNP extracted from the JV curves of devices under 1 Sun illumination.

Source: Prepared by the author.

Table 15 shows the intersection of the 99% confidence interval of the double layer data with 0.05% GNP with the reference. It confirms that the data are statistically equal. There is a slight reduction in the average of the results due to the insertion of 0.05% of graphene. However, it is believed that such data can be improved with good optimization of the systems and processing conditions. Furthermore, the DL SnO_2 (IPA)/SnO_2+0.05%GNP devices displayed a reduction of approximately 65% of the HI, with similar real PCE. In the 1.5 IQR test, the highest real PCE for DL SnO_2 (IPA) +2.5%GNP/SnO_2 is an outlier; however, this value is not discarded as non-standard since it is also near the central region in the distribution curve and within the 99% confidence limit.

It is worth remembering that the SnO_2 (IPA) 0.1M devices had a real PCE of 8.8±2.6 (13.7)%, proving that implementing the double layer is a very interesting and promising solution. As for the sample, the SnO_2 (IPA) + 0.05%GNP devices obtained 7.2 ± 1.2% (10%*) of real efficiency and HI 3 times higher. In other words, incorporating GNP in the double layer effectively improved the real PCE as the hysteresis is reduced, even in relation to the SnO_2 control device (IPA).

Table 15: Real PCE and HI data for experiments of Group 4 with the double layer with SnO_2 (IPA) containing different levels of GNP extracted from the JV curves of devices under 1 Sun illumination, represented in terms of [mean ± 99% confidence limit (best)].

	Real PCE (max) [%]	**HI (|min|) [%]**
SnO_2 (IPA)	13.4 ± 0.8 (15.7)	35.3 ± 4.6 (-11.1*)
DL SnO_2 (IPA)/ SnO_2+0.05%GNP	10.9 ± 2.1 (12.3)	12.6 ± 5.8 (9.6)
DL SnO_2 (IPA)/ SnO_2 +2.5%GNP	0.8 ± 0.3 (1.1)	15.9 ± 10.2 (7.3)
DL SnO_2 (IPA) + 0.05%GNP/SnO_2	11.3 ± 2.1 (13.4)	25.8 ± 27.7 (-9)
DL SnO_2 (IPA) +2.5%GNP/SnO_2	0.2 ± 0.2 (0.4)	48.6 ± 25.9 (12.5*)
DL SnO_2 (IPA)/GNP	0.9 ± 0.2 (0.9)	28.3 ± 55.7 (20.4)

* Data presented outside the limit established by the box plot of 1.5 IQR, being considered invalid (outlier).

Source: Prepared by the author.

Finally, the JV curves of the devices with the highest real PCE value are revealed in Figure 48. First, it is worth noting that the double layer devices with 2.5% GNP and those with GNP above the compact ETL layer showed straight characteristics of short circuit. The efficiency data is insignificant because the device was in a short circuit. It is probably due to the difficulty of properly forming the ETL layers, which can even get in the way of the active layer due to the high graphene content. As seen in Table 13 and evidenced in the JV curve, there is a significant increase in the J_{sc} intercept of the ordinate axis, demonstrating greater photocurrent generation due to the implementation of the double layer with 0.05% GNP. In addition, there is a significant reduction in the V_{oc} differences between backward (B) and forward (F) scanning, proving lower hysteresis of these devices. These data corroborate that the double layer preparation with 0.05% graphene contents is very promising.

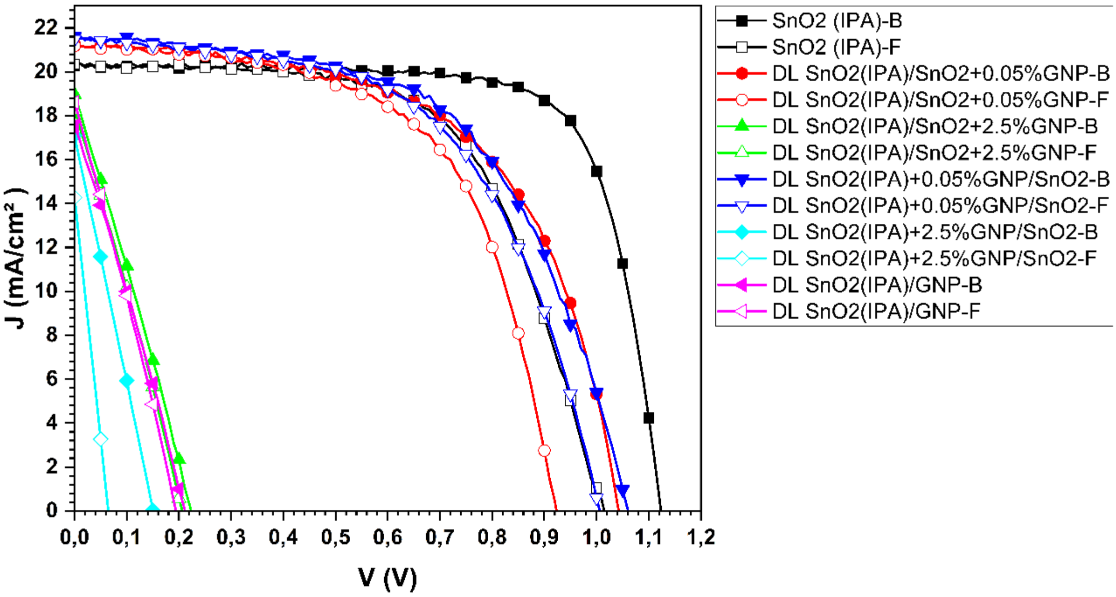

Figure 48: JV curve of the highest real PCE for experiments of Group 4 with the double layer with SnO_2 (IPA) containing different levels of GNP under 1 Sun illumination.

Source: Prepared by the author.

4.5 GROUP 5: SnO_2 (IPA) + DIFFERENT TYPES OF NANOPARTICLES

Based on the results of the previous sections, it can be seen that the concentration of 0.05% of graphene is the most promising for application in the ETL layer of SnO_2. The precursor SnO_2 (IPA) was also the most interesting for graphene dispersion. Thus, to evaluate different types of graphene, the contents of 0.05% and 0.5% of filler were used for mapping. Few-layers graphene produced by a liquid exfoliation method with approximately 55% nonionic surfactant content; graphene oxide (GO) and reduced graphene oxide synthesized from chemical exfoliation of graphite flakes by the improved Hummers method, as well as anatase titanium dioxide nanoparticles (TiO_2) were the nanoparticles select to be tested. As a comparison, the results of the control devices (with SnO_2 (IPA)) and with graphene nanoplatelets (GNP) will be presented.

In Figure 49, the box plot shows the open-circuit voltage results of the manufactured solar module. First, the increase in filler content leads to a significant reduction for the graphenes GNP, FLG, and rGO. As for the GO, the V_{oc} reduction is not very intense. While for TiO_2, there is an increase in this parameter when incorporating 0.5% of nanoparticle, the only material that increased a property with higher filler content. Furthermore, with the increase in the filler content, it can also be observed that the difference in V_{oc} concerning the scanning direction is also minimized. Probably, the low content of nanoparticles generates heterogeneities distant from each other. In contrast, higher content should generate a better layer filling, acting as a better way to minimize the effects of surface polarization.

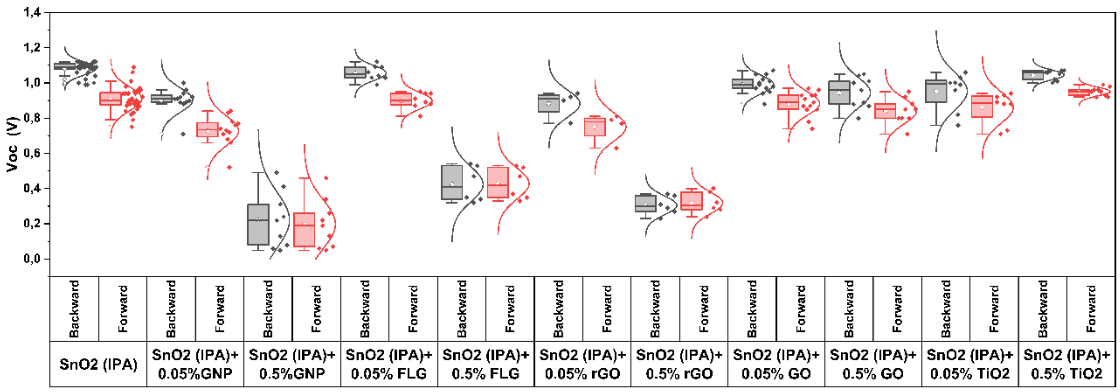

Figure 49: Graphic presentation of V_{oc} by box plot statistics and distribution curve for experiments of Group 5 with SnO_2 (IPA) containing different types and levels of nanoparticles extracted from the JV curves of devices under 1 Sun illumination.

Source: Prepared by the author.

Figure 50 shows the box plot of the short-circuit current density results. In general, increasing filler concentration tends to reduce J_{sc} slightly. Only for GNP, there is a significant reduction due to the increase of graphene to 0.5%. In addition, devices with this type of graphene exhibited inferior J_{sc} performance compared to other nanoparticles. Commercial GNP has a higher number of stacked sheets than other graphene types. rGO and GO have a smaller number of stacked nanosheets than GNP but have a larger lateral size.

Regarding composition, rGO and GNP are similar, with a low concentration of impurities. The GO has a high content of oxygenated groups, which could improve the interaction with oxide. FLG has a high surfactant content making it easier to disperse or interact with FTO or with SnO_2, or even perovskite.

TiO_2, metallic oxide, also tends to show good interaction with SnO_2. In addition, titanium dioxide is a good electron acceptor already used as an ETL in high-efficiency photovoltaic devices. Its problem, in general, is the production of homogeneous films with high transparency and optoelectronic properties compatible with the active layer. It needs heat treatment at high temperatures to achieve high performance. There is no work in the literature, or it is still little explored, the solution of using nanoparticles already with anatase polymorphism to produce nanocomposite for ETL. Another alternative would be to synthesize the TiO_2 nanoparticles, carry out their heat treatment to obtain the anatase phase and then apply it as a nanocomposite in ETL layers. It would reduce the problems related to heat treating the conductive transparent electrode or obtaining homogeneous films.

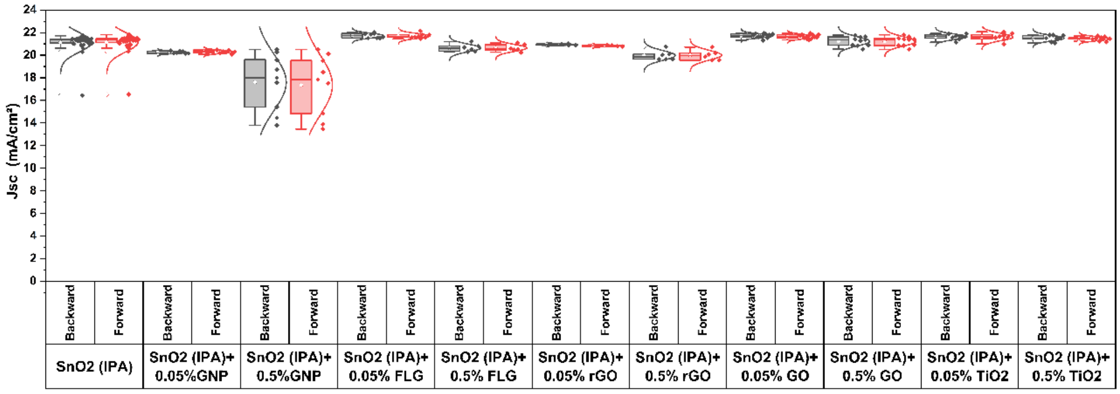

Figure 50: Graphic presentation of J_{sc} by box plot statistics and distribution curve for experiments of Group 5 with SnO_2 (IPA) containing different types and levels of nanoparticles extracted from the JV curves of devices under 1 Sun illumination.

Source: Prepared by the author.

Table 16 presents the data of V_{oc} and J_{sc} concerning their averages, 99% confidence limit, and records. Devices with 0.05% of FLG and GO did not show any differences in relation to the V_{oc} of SnO_2 (IPA). The insertion of 0.05% of TiO_2 also obtained a similar result. Only titanium dioxide maintained this high parameter after inserting 0.5% of filler. However, it is worth noting that the GO obtained a very close V_{oc}, 0.94 ± 0.09 (1.05) V. With the increase in the nanoparticle content, GNP, FLG, and rGO reduced the open-circuit voltage drastically. It is believed that the GO and TiO_2 presented a good interface with the SnO_2 due to the interactions between the oxygenated groups. The FLG at low levels would also mix well with the SnO_2 due to the surfactants, but increasing concentration must have generated many agglomerates.

Regarding the current density, the devices showed similar behavior concerning V_{oc}. However, 0.05% of FLG, GO, and TiO_2 significantly increased compared with the control sample, demonstrating a gain in the property. At 0.5%, TiO_2 and GO maintained J_{sc} above the reference ETL. Such results demonstrate the excellent performance of these materials mentioned, superior to SnO_2 (IPA). The higher content for ETL with GNP, FLG, and rGO drastically reduced the short-circuit current density. Probably, the increase in concentration made the layer darker, absorbing and reflecting more photons, attenuating the light incident on the active layer, and reducing the photocurrent. Finally, it is worth mentioning that the GNP was the sample that presented the lowest performance in relation to V_{oc} and J_{sc}; for example, it was the material with 0.5% that obtained the lowest results for these parameters. Even with 0.5%, the other materials showed a higher J_{sc} than this sample with only 0.05%.

Table 16: V_{oc} and J_{sc} data for experiments of Group 5 with SnO_2 (IPA) containing different types and levels of nanoparticles extracted from the JV curves of devices under 1 Sun illumination, represented in terms of [mean ± 99% confidence limit (best)].

	Voc (max) [V]		**J_{sc} (max) [mA/cm²]**	
	Backward	**Forward**	**Backward**	**Forward**
SnO_2 (IPA)	1.08 ± 0.02 (1.12)	0.91 ± 0.03 (1.09*)	21.14 ± 0.39 (21.72)	21.15 ± 0.39 (21.82)
SnO_2 (IPA)+ 0.05%GNP	0.90 ± 0.06 (1)	0.73 ± 0.07 (0.84)	20.42 ± 0.47 (21.06)	20.44 ± 0.49 (21.05)
SnO_2 (IPA)+ 0.5%GNP	0.22 ± 0.16 (0.49*)	0.2 ± 0.14 (0.46)	17.59 ± 2.56 (20.51)	17.36 ± 2.73 (20.49)
SnO_2 (IPA)+ 0.05%FLG	1.06 ± 0.05 (1.12)	0.9 ± 0.05 (0.95)	21.73 ± 0.24 (22.02)	21.71 ± 0.24 (22.16)
SnO_2 (IPA)+ 0.5%FLG	0.43 ± 0.14 (0.54)	0.43 ± 0.12 (0.53)	20.65 ± 0.47 (21.21)	20.65 ± 0.43 (21.09)
SnO_2 (IPA)+ 0.05%rGO	0.88 ± 0.15 (0.94)	0.75 ± 0.16 (0.81)	20.94 ± 0.13 (21.02)	20.84 ± 0.13 (20.91)
SnO_2 (IPA)+ 0.5%rGO	0.31 ± 0.07 (0.37)	0.32 ± 0.08 (0.4)	19.98 ± 0.61 (20.77)	20 ± 0.61 (20.72)
SnO_2 (IPA)+ 0.05%GO	0.99 ± 0.04 (1.07)	0.88 ± 0.05 (0.97)	21.72 ± 0.14 (21.97)	21.64 ± 0.14 (21.93)
SnO_2 (IPA)+ 0.5%GO	0.94 ± 0.09 (1.05)	0.84 ± 0.07 (0.95)	21.23 ± 0.39 (21.78)	21.23 ± 0.4 (21.8)
SnO_2 (IPA)+ 0.05%TiO_2	0.95 ± 0.12 (1.06)	0.86 ± 0.1 (0.94)	21.63 ± 0.28 (21.92)	21.61 ± 0.37 (22.07)
SnO_2 (IPA)+ 0.5%TiO_2	1.05 ± 0.03 (1.07)	0.95 ± 0.03 (0.99)	21.51 ± 0.25 (21.8)	21.46 ± 0.18 (21.71)

* Data presented outside the limit established by the box plot of 1.5 IQR, being considered invalid (outlier).

Source: Prepared by the author.

The fill factor data in the box plot in Figure 51 demonstrate similar behavior to V_{oc}. Samples with 0.5% of GNP, FLG, rGO, or GO did not show any FF difference in the scanning direction. The increase in the graphene oxide content tended to slightly reduce the FF, while the other types of graphene had a more drastic reduction. On the other hand, the nanocomposites with 0.5% of TiO_2 showed an increase in their property. TiO_2 is also considered a heterogeneity in the volume of SnO_2 films. However, this oxide has excellent properties as ETL. Thus, it is believed that the increase in its concentration tends to improve the FF. The film would have been better filled, creating a certain organization before the mixture that presents good compatibility because both are metallic oxides with good interaction. It corroborates the fact that graphene oxide also did not show a great loss of property since the oxygenated groups display good interaction with tin dioxide. The other materials tend to increase the surface area, and due to the weaker compatibility with SnO_2, it increases the probability of charge recombination and reduces the FF. As the V_{oc} is also reduced, it can be suggested that the charge extraction would not be happening as efficiently or the surface acts as a charge carrier trap.

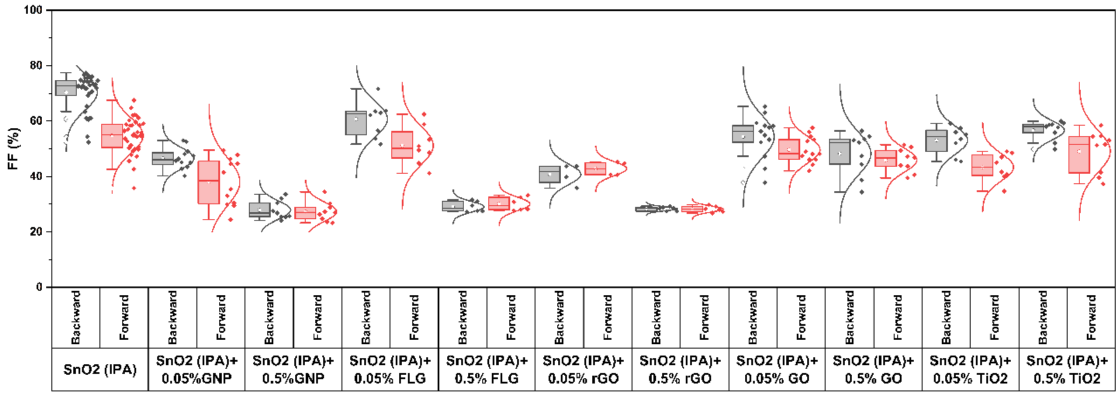

Figure 51: Graphic presentation of FF by box plot statistics and distribution curve 5 for experiments of Group 5 with SnO_2 (IPA) containing different types and levels of nanoparticles extracted from the JV curves of devices under 1 Sun illumination.

Source: Prepared by the author.

In Figure 52, the box plots of the PCE data present an identical behavior to that of the FF, only with a more accentuated reduction of the performances concerning the increase of the filler concentration. Content of 0.5% of GNP, FLG, and rGO generated non-functional devices. Among these three types of graphene, their nanosheets have the same composition. The difference between them is the dimensions of the nanoparticles. rGO is the one with the largest lateral size, while GNP has a greater number of superimposed nanolayers. FLG has 55% surfactant in its composition. This surfactant, together with the smaller nanosheets, facilitates the dispersion generating better quality films. That corroborates the literature, where the graphenes that present better performance when mixed with SnO_2 are the graphene quantum dots. This type of nanoparticle has all two dimensions on the nanometer scale, with a much smaller lateral size than those used in the present work. The main improvements in the insertion of graphene quantum dot (GQD) are the increased electrical conductivity of the SnO_2 films while acting as a good electron acceptor by presenting an intermediate LUMO level between perovskite and SnO_2 (NAGARAJ *et al.*, 2021).

PANG *et al.* (2020) added GQD in a colloidal suspension of SnO_2 from the same source as the present work. They observed that adding GQDs increases the J_{sc} (from 22.2 mA cm^{-2} to 24.0 mA cm^{-2}) and the V_{OC} (1.07 V to about 1.10 V). compared to the reference without GQDs. Such improvements, together with the slight increase in FF, generated devices with an average PCE of 20.7%. In addition, there is an increase in the crystallinity and grain size of MAFA perovskite.

The SnO_2 (IPA)+ 0.05%FLG generated excellent devices, with the results fully contained within the scattering range of the reference device's box plot. The two groups are statistically equal since the population of devices with 0.05% FLG is contained in the sample space of the reference device. There is only a slight drop in the mean and median values of the backward sweep. The SnO_2 (IPA)+ 0.05%GO and SnO_2 (IPA)+ 0.5%TiO_2 devices also showed coincidence in the interval between Q1 and the lower limit of 1.5 IQR of the reference device, presenting at least 25% of compatibility between the data. Thus, such data demonstrate the remarkable similarity between the standard sample.

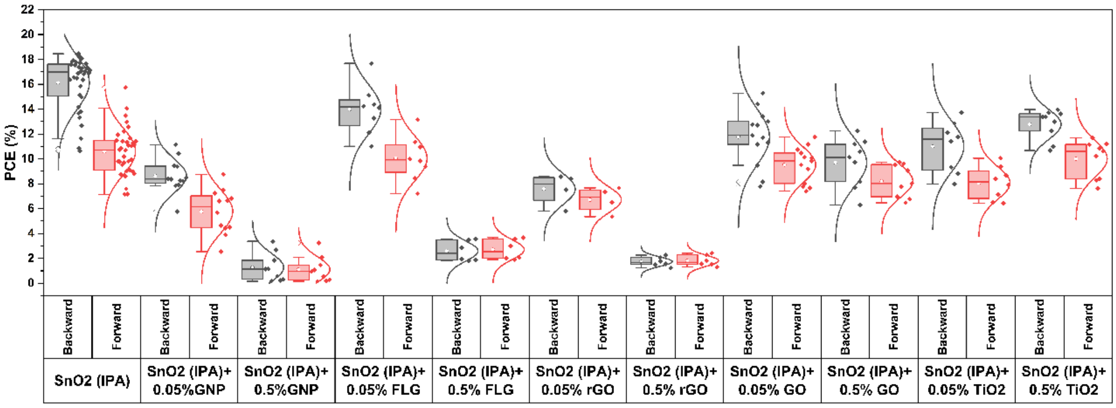

Figure 52: Graphic presentation of PCE by box plot statistics and distribution curve for experiments of Group 5 with SnO_2 (IPA) containing different types and levels of nanoparticles extracted from the JV curves of devices under 1 Sun illumination.

Source: Prepared by the author.

Table 17 exhibits the FF and PCE data with their respective values concerning the 99% confidence limit and the record results. The SnO_2 (IPA)+ 0.05%FLG device was the only one that presented an intersection of the FF in the confidence interval with the standard device; in addition, it had a high record value of 72%. That demonstrates that dispersion and surfactant aid in forming homogeneous layers that likely generate good quality perovskite films, which generates a low probability of recombination with good electron extraction (LU *et al.*, 2021). This composition also generated devices with ECP of 14 ± 2.2% (17.7%), also presenting a significant intersection with the reference sample, above the average value of the population, demonstrating that statistically, the data exhibit some degree of similarity. With the aid of the surfactant, the graphene of a few layers generated the best devices for the present work. But the double layer samples with 0.05% GNP, SnO_2 (IPA)+ 0.05%GO, and TiO_2 with 0.05% and 0.5% also showed high performance, demonstrating that the optimization of these devices in terms of thickness of layer, processing conditions, and even the proportion of nanoparticles could exceed the reference.

Table 17: FF and PCE data for experiments of Group 5 with SnO_2 (IPA) containing different types and levels of nanoparticles extracted from the JV curves of devices under 1 Sun illumination, represented in terms of [mean ± 99% confidence limit (best)].

	FF (max) [%]		**PCE (max) [%]**	
	Backward	**Forward**	**Backward**	**Forward**
SnO_2 (IPA)	70 ± 3 (77)	55 ± 3 (67)	16.1 ± 1.0 (18.5)	10.6 ± 0.9 (15.7*)
SnO_2 (IPA)+ 0.05%GNP	47 ± 3 (53)	38 ± 7 (50)	8.6 ± 1.2 (11.1)	5.8 ± 1.5 (8.8)
SnO_2 (IPA)+ 0.5%GNP	28 ± 3 (34)	27 ± 4 (34)	1.3 ± 1.2 (3.4*)	1.1 ± 1.0 (3.3*)
SnO_2 (IPA)+ 0.05%FLG	61 ± 7 (72)	51 ± 8 (63)	14 ± 2.2 (17.7)	10 ± 2.0 (13.2)
SnO_2 (IPA)+ 0.5%FLG	29 ± 3 (31)	30 ± 3 (33)	2.6 ± 1.1 (3.5)	2.7 ± 1.1 (3.7)
SnO_2 (IPA)+ 0.05%rGO	41 ± 7 (44)	43 ± 5 (45)	7.6 ± 2.5 (8.6)	6.7 ± 2.1 (7.7)
SnO_2 (IPA)+ 0.5%rGO	28 ± 1 (29)	28 ± 2 (30)	1.7 ± 0.5 (2.3)	1.8 ± 0.6 (2.4)
SnO_2 (IPA)+ 0.05%GO	54 ± 6 (65)	50 ± 4 (58)	11.8 ± 1.8 (15.3)	9.5 ± 1.1 (11.8)
SnO_2 (IPA)+ 0.5%GO	48 ± 8 (56)	46 ± 4 (51)	9.7 ± 2.0 (12.2)	8.2 ± 1.3 (9.7)
SnO_2 (IPA)+ 0.05%TiO_2	53 ± 6 (59)	43 ± 5 (49)	11 ± 2.3 (13.7)	8.1 ± 1.5 (10.1)
SnO_2 (IPA)+ 0.5%TiO_2	57 ± 4 (60)	49 ± 8 (59)	12.8 ± 1.2 (14)	10 ± 1.5 (11.7)

* Data presented outside the limit established by the box plot of 1.5 IQR, being considered invalid (outlier).

Source: Prepared by the author.

In Figure 53, the real PCE of the device with 0.05% FLG is fully contained in the dispersion of the reference device data, so statistically, such results are the same, with a slight reduction in the sample mean value. The samples with GO and TiO_2 also intersect with the 1.5 IQR limit, demonstrating similarity in the data. It is worth noting that the SnO_2 (IPA)+ 0.5%TiO_2 and SnO_2 (IPA)+ 0.05%GO data are also fully contained in the withdrawal period, which statistically demonstrates high-performance compatibility between devices.

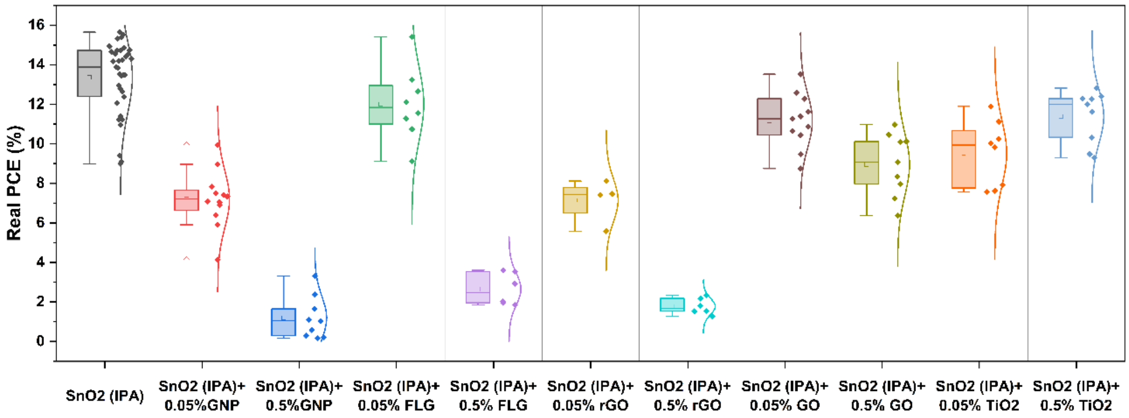

Figure 53: Graphic presentation of real PCE by box plot statistics and distribution curve for experiments of Group 5 with SnO_2 (IPA) containing different types and levels of nanoparticles extracted from the JV curves of devices under 1 Sun illumination.

Source: Prepared by the author.

In Figure 54, it is observed that the nanoparticles significantly reduced hysteresis in general. It is believed that as graphene is an excellent electrical conductor, it increases the conductivity of films and still reduces polarization effects. The GO, FLG, and TiO_2 samples that presented high performance also reduced hysteresis with minimum values, in modulus, close to zero since the minimum valid value for the reference device is near 20%. The 0.5% particle content showed lower hysteresis. However, these devices were the ones that presented inferior performance, except for the sample with 0.5% of TiO_2 that obtained an improvement concerning the low content of nanoparticles.

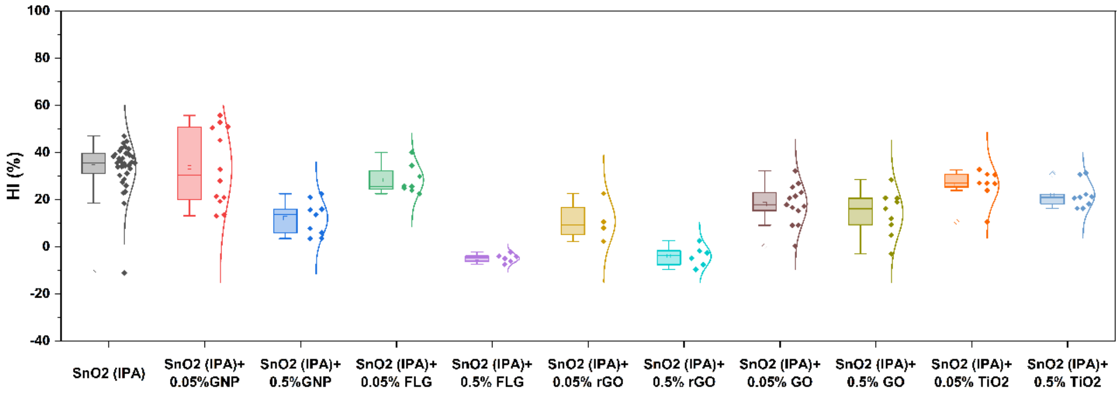

Figure 54: Graphic presentation of HI by box plot statistics and distribution curve for experiments of Group 5 with SnO_2 (IPA) containing different types and levels of nanoparticles extracted from the JV curves of devices under 1 Sun illumination.

Source: Prepared by the author.

In Table 18, the samples SnO_2 (IPA)+ 0.05%FLG, SnO_2 (IPA)+ 0.05%GO and SnO_2 (IPA)+ 0.5%TiO_2 existed an intersection between the confidence interval with the reference sample. It demonstrates that the performance of these devices is statistically similar to the SnO_2 device (IPA), though with lower hysteresis. The HI data of these devices obtained minimum values, in modulus, close to zero. That is, the devices' performance improved by adding these nanoparticles. In addition, it is worth noting that the record for the real efficiency of the SnO_2 (IPA)+ 0.05%FLG device was practically equal to the record of the reference sample. Therefore, based on the data, it is possible to conclude that GO, FLG, and TiO_2 are very promising nanoparticles for preparing devices with high efficiency with improved performance.

Table 18: Real PCE and HI data for experiments of Group 5 with SnO_2 (IPA) containing different types and levels of nanoparticles extracted from the JV curves of devices under 1 Sun illumination, represented in terms of [mean ± 99% confidence limit (best)].

	Real PCE [%]	**HI (|min|) [%]**
SnO_2 (IPA)	13.4 ± 0.8 (15.7)	35.3 ± 4.6 (-11.1*)
SnO_2 (IPA)+ 0.05%GNP	7.2 ± 1.2 (10*)	33.7 ± 13.8 (13.1)
SnO_2 (IPA)+ 0.5%GNP	1.2 ± 1.1 (3.3)	12.2 ± 7.4 (3.4)
SnO_2 (IPA)+ 0.05%FLG	12.0 ± 2.1 (15.4)	28.4 ± 6. 8(22.5)
SnO_2 (IPA)+ 0.5%FLG	2.6 ± 1.1 (3.6)	-4.8 ± 2. 5(-7.4)
SnO_2 (IPA)+ 0.05%rGO	7.1 ± 2.2 (8.1)	10.8 ± 17.1 (2.3)
SnO_2 (IPA)+ 0.5%rGO	1.8 ± 0.6 (2.3)	2.6 ± 6 (-9.6)
SnO_2 (IPA)+ 0.05%GO	11.2 ± 1.2 (13.5)	20.5 ± 5.6 (9.1)
SnO_2 (IPA)+ 0.5%GO	9.0 ± 1.6 (11)	16.4 ± 9.7 (-3.0)
SnO_2 (IPA)+ 0.05%TiO_2	9.5 ± 1.8 (11.9)	26.2 ± 7.6 (10.6)
SnO_2 (IPA)+ 0.5%TiO_2	11.4 ± 1.4 (12.8)	22.0 ± 5.7 (16.3)

* Data presented outside the limit established by the box plot of 1.5 IQR, being considered invalid (outlier).

Source: Prepared by the author.

Figure 55 presents the JV curves of the devices with the highest real PCE concerning the types of nanoparticles combined with SnO2. First, the significant improvement of the intercept on the ordinate axis related to J_{sc}. Such improvement was common for the nanocomposites containing TiO_2, FLG, and GO, which were the ones that showed high energy conversion efficiency. V_{oc} presents a slight reduction depending on the type of nanoparticle used. Finally, the results showed the improvement of the device's performance not only in increasing the current density, which represents a greater generation of photocurrent due to the addition of nanoparticles, but also a superior performance when presenting lower HI while obtaining highly efficient devices, similar to the standard device.

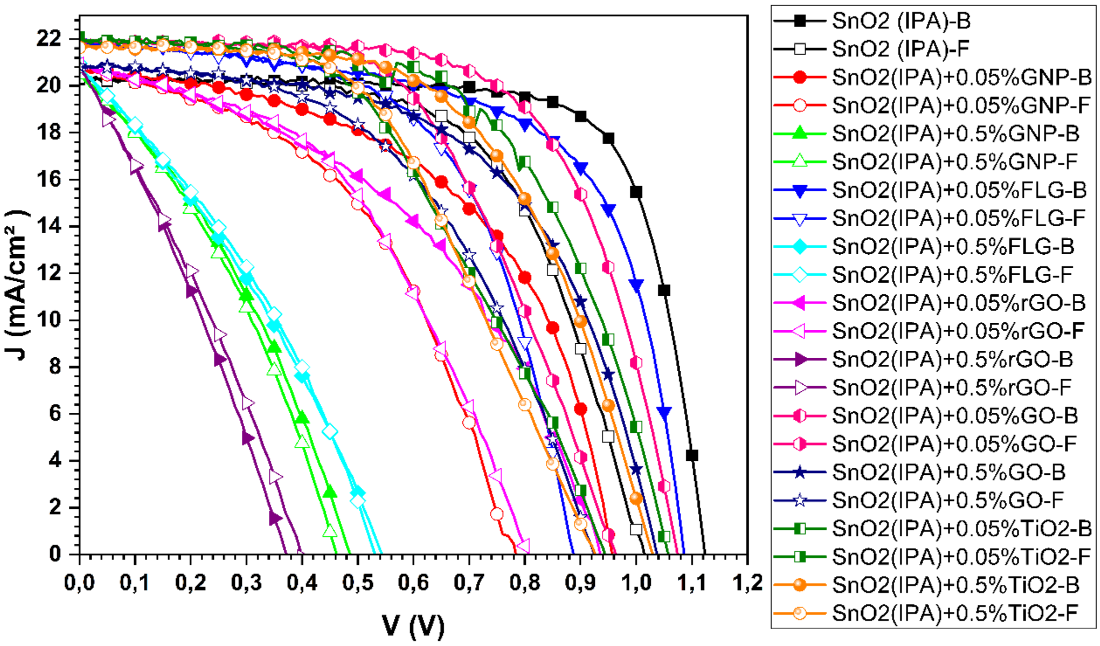

Figure 55: JV curve of the highest real PCE for experiments of Group 5 devices with SnO_2 (IPA) containing different types and levels of nanoparticles under 1 Sun illumination.

Source: Prepared by the author.

5. FINAL CONSIDERATIONS

Initially, in the present work, it was possible to manufacture multi-cation perovskite photovoltaic devices (CsMAFA) with high power conversion efficiency, achieving 16.1 ± 1% (18.5%) in the backward scanning direction and 10.6 ± 0.9 (15.7*) in the forward, with real PCE of 13.4 ± 0.8% (15.7%) and HI of 35.3 ± 4.6. In addition, evaluations with conventional methods showed that the SnO_2 precursor from the salt tin tetrachloride pentahydrate obtained higher PCE. However, the ETL hysteresis produced by this precursor is high. On the other hand, the surface modification methods and the preparation of the ETL layer from colloidal dispersions of SnO_2 nanoparticles showed the lowest hysteresis effect.

The research employing ETL layers with GNP, FLG, rGO, GO, and TiO_2-anatase in different concentrations resulted in excellent efficiency. Concerning Group 2, the mixture SnO_2 (IPA) with GNP at different levels was observed, and the best ETL preparation concentration was with 0.05% filler. In Group 3, it was evaluated that the preparation with the precursor SnO_2 (H_2O) obtained devices with efficiency slightly lower than the previous group, with null hysteresis. The preparation of the double layer showed that it is possible to improve the efficiency of the devices with 0.05% graphene in up to approximately 64% of the real PCE compared to the single layer. The hysteresis was also reduced to one-third compared to the standard device and single-layer nanocomposites. In the experiments of Group 5, it was possible to obtain devices with FLG, GO, and TiO_2-anatase with efficiency similar to the standard device, with the improvement of the short-circuit current density up to 22.07mA/cm^2, the open-circuit voltage of 1.12 V, PCE of 17.7% in the backward scan, real PCE of 15.4%, with reduced hysteresis effect. In addition, the use of non-ionic surfactants and surface functionalization with oxygenated groups, as in graphene oxide, tends to improve the interaction of nanoparticles with SnO_2, improving the fill factor, demonstrating less recombination of charge carriers and still better electron extraction. Devices, in general, had reduced properties with higher contents of graphene. On the other hand, titanium dioxide improved the performance with 0.5% filler.

Finally, it is worth mentioning that the present work can demonstrate excellent and promising results due to the insertion of different nanoparticles in the ETL layer of $SnoO_2$. In addition, it is possible to verify new perspectives for improving this ETL based on the discussion of the results obtained. In this way, various alternatives can still be used to solve the main problems of perovskite solar cells with high energy conversion efficiency to enable their application in the market.

6. SUGGESTIONS FOR FUTURE WORK

Based on the results presented, it is believed that there is still optimization to be carried out. First, optimizing layer deposition can improve device efficiency and reduce hysteresis. That is, to carry out experiments varying the spin coating conditions or even the concentration of the solutions to verify the influence of the thickness of the nanocomposite layers on the performance of photovoltaic devices.

Another optimization could be found by testing the contents of 0.05, 0.1, and 0.5% of FLG, GO, and TiO_2 by applying the double layer and combining the SnO_2 precursor (H_2O) in this technique. It is also believed that by preparing a compact layer from SnO_2 (IPA) and then depositing a layer from the colloidal dispersion of nanoparticles on top, it is possible to obtain double-layer devices combining mesoscopic and compact technology similar to TiO_2 layers as ETL. In addition, it could evaluate the insertion of graphene and TiO_2 in both layers and enhance the devices' performance.

As the TiO_2 devices significantly increased photovoltaic parameters with the increase in their concentration, they could be tested with higher contents to map their efficiency fully. Furthermore, it could also be combined with colloidal SnO_2 nanoparticles. Or even then, use titanium oxide precursors mixed with SnO_2 nanoparticles to verify their properties.

The functionalization of graphene oxide could also be interesting to improve the interface with SnO_2 even more. Or even then, evaluate the preparation of layers with the ternary composition. The quantum dot graphene could also be evaluated in the proposed modifications since it has an impressive performance in the literature.

Surface morphology studies of ETL films on the FTO by AFM or SEM could reveal the dispersion of graphenes or TiO_2 as well as the homogeneity quality of SnO_2 matrix. The same could be done to evaluate the influence of the variation of the ETL above the perovskite films, being able to verify the quality of the active layer and the affinity between the materials. For this, it would be necessary to prepare the Glass/FTO/ETL/Perovskite architecture. The contact angle test using a drop of water, or even other solvents of different polarities, could add information about hydrophilicity and adhesion of thin films. The visualization through the cross section of the complete device by SEM could also reveal interesting information about adhesion, types of defects and homogeneity of the layers. The crystallography of the system could be studied by X-ray diffraction (XRD) and its results could be corroborated with the FTIR spectra to verify the formation of SnO_2, crystallinity and phases present in the films. Furthermore, with the preparation of the Glass/FTO/ETL/Perovskite architecture, it was possible to verify the influence that CsMAFA has on the nucleation processes and grain growth for the formation of films above the ETL. The in situ study would also be very interesting to see if graphene is disrupting the precipitation of the cubic phase of perovskite. Through the UV-Vis analysis, it could verify the transparency of the ETL films and also the absorbance spectrum of the films. The verification of the levels of the occupied and unoccupied orbitals would be interesting to identify if an adequate alignment is taking place for the electron cascade effect. This could be done by combining UV Vis analysis ,to obtain the bandgap, with the unoccupied orbital level by cyclic voltammetry analysis and obtaining the alignment of energy levels in relation to the other layers. The ultraviolet photoelectron spectroscopy (UPS) could also be used to obtain such information in a single characterization. Furthermore, electrical conductivity studies of the ETL samples could be useful to verify whether graphene or TiO_2 actually increases the conductivity of the films. This could also be done by depositing the perovskite layer on top of the ETL and confirming its charge mobility. Photoluminescence could facilitate the understanding of recombination mechanisms and approximately quantify the exciton recombination time. Finally, monitoring the efficiency of the devices over time could describe about the stability and verifying the feasibility of implementing the ETL studied.

7. REFERENCES

ATTIA, S. K.; ELGENDY, A. T.; RIZK, S. A. Efficient green synthesis of antioxidant azacoumarin dye bearing spiro-pyrrolidine for enhancing electro-optical properties of perovskite solar cells. **Journal of Molecular Structure**, vol. 1184, p. 583–592, 15 May 2019. https://doi.org/10.1016/j.molstruc.2019.02.042.

BISQUERT, J.; JUAREZ-PEREZ, E. J. The Causes of Degradation of Perovskite Solar Cells. **Journal of Physical Chemistry Letters**, vol. 10, no. 19, p. 5889–5891, 3 Oct. 2019. https://doi.org/10.1021/acs.jpclett.9b00613.

CASE, C.; BEAUMONT, N.; KIRK, D. Industrial Insights into Perovskite Photovoltaics. **ACS Energy Letters**, vol. 4, no. 11, p. 2760–2762, 8 Nov. 2019. https://doi.org/10.1021/acsenergylett.9b02105.

CHEN, B.; YANG, M.; PRIYA, S.; ZHU, K. Origin of JV Hysteresis in Perovskite Solar Cells. **Journal of Physical Chemistry Letters**, vol. 7, no. 5, p. 905–917, 3 Mar. 2016. https://doi.org/10.1021/acs.jpclett.6b00215.

DENG, K.; CHEN, Q.; SHEN, Y.; LI, L. Improving UV stability of perovskite solar cells without sacrificing efficiency through light trapping regulated spectral modification. **Science Bulletin**, vol. 66, no. 23, p. 2362–2368, 15 Dec. 2021. https://doi.org/10.1016/j.scib.2021.06.022.

DENG, L.; YANG, H.; LIU, Z.; YANG, X.; HUANG, Z.; YU, H.; WANG, K.; LI, J. Effective Phase Control for High-Performance Red-Light-Emitting Quasi-2D Perovskite Solar Cells via MACl Additive. **ACS Applied Energy Materials**, vol. 4, no. 3, p. 2856–2863, 22 Mar. 2021. https://doi.org/10.1021/acsaem.1c00185.

FENG, Y.; ZHANG, J.; DUAN, C.; ZHANG, X.; ZHANG, Y.; DAI, J. Improved inverted MAPbI3 perovskite solar cell with triphenylphosphine oxide passivation layer. **Optical Materials**, vol. 127, 1 May 2022. https://doi.org/10.1016/j.optmat.2022.112264.

GAO, B.; YAO, H.; HOU, J.; YU, R.; HONG, L.; XU, Y.; HOU, J. Multi-component non-fullerene acceptors with tunable bandgap structures for efficient organic solar cells. **Journal of Materials Chemistry A**, vol. 6, no. 46, p. 23644–23649, 2018. https://doi.org/10.1039/C8TA09830A.

GAUTAM, B. R.; YOUNTS, R.; CARPENTER, J.; ADE, H.; GUNDOGDU, K. The Role of FRET in Non-Fullerene Organic Solar Cells: Implications for Molecular Design. **Journal of Physical Chemistry A**, vol. 122, no. 15, p. 3764–3771, 19 Apr. 2018. https://doi.org/10.1021/acs.jpca.7b12807.

HINRICHSEN, T. F.; CHAN, C. C. S.; MA, C.; PALEČEK, D.; GILLETT, A.; CHEN, S.; ZOU, X.; ZHANG, G.; YIP, H. L.; WONG, K. S.; FRIEND, R. H.; YAN, H.; RAO, A.; CHOW, P. C. Y. Long-lived and disorder-free charge transfer states enable endothermic charge separation in efficient non-fullerene organic solar cells. **Nature Communications**, vol. 11, no. 1, 1 Dec. 2020. https://doi.org/10.1038/s41467-020-19332-5.

HOU, M.; XU, Y.; TIAN, Y.; WU, Y.; ZHANG, D.; WANG, G.; LI, B.; REN, H.; LI, Y.; HUANG, Q.; DING, Y.; HOU, G.; ZHAO, Y.; ZHANG, X. Synergistic effect of MACl and DMF towards efficient perovskite solar cells. **Organic Electronics**, vol. 88, 1 Jan. 2021. https://doi.org/10.1016/j.orgel.2020.106005.

HUANG, Y.; LIU, T.; LIANG, C.; XIA, J.; LI, D.; ZHANG, H.; AMINI, A.; XING, G.; CHENG, C. Towards Simplifying the Device Structure of High-Performance Perovskite Solar Cells. **Advanced Functional Materials**, vol. 30, no. 28, 1 Jul. 2020. https://doi.org/10.1002/adfm.202000863.

ICHWANI, R.; KOECH, R.; OYEWOLE, O. K.; HUDA, A.; OYEWOLE, D. O.; CROMWELL, J.; MARTIN, J. L.; GRIMM, R. L.; SOBOYEJO, W. O. Interfacial fracture of hybrid organic–inorganic perovskite solar cells. **Extreme Mechanics Letters**, vol. 50, 1 Jan. 2022. https://doi.org/10.1016/j.eml.2021.101515.

JENA, A. K.; NUMATA, Y.; IKEGAMI, M.; MIYASAKA, T. Role of spiro-OMeTAD in performance deterioration of perovskite solar cells at high temperature and reuse of the perovskite films to avoid Pb-waste. **Journal of Materials Chemistry A**, vol. 6, no. 5, p. 2219–2230, 2018. https://doi.org/10.1039/c7ta07674f.

LIU, G.; TIAN, T.; YANG, J.; ZHONG, J. X.; GULAMOVA, D.; WU, W. Q. Carbon Electrode Endows High-Efficiency Perovskite Photovoltaics Affordable, Fully Printable, and Durable. **Solar RRL**, 1 Jul. 2022. https://doi.org/10.1002/solr.202200258.

LUCEÑO-SÁNCHEZ, J. A.; DÍEZ-PASCUAL, A. M.; CAPILLA, R. P. Materials for photovoltaics: State of art and recent developments. **International Journal of Molecular Sciences**, vol. 20, no. 4, 2 Feb. 2019. https://doi.org/10.3390/ijms20040976.

MAYIMELE, M. A.; FRU, J. N.; NYARIGE, J. S.; DIALE, M. Sequential physical vapor deposited methylammonium lead tri-iodide perovskites on FTO and ITO modified zinc oxide nanorods for perovskite solar cells. **Physica B: Condensed Matter**, vol. 625, 15 Jan. 2022. https://doi.org/10.1016/j.physb.2021.413462.

NAN, G.; ZHANG, X.; LU, G. Self-Healing of Photocurrent Degradation in Perovskite Solar Cells: The Role of Defect-Trapped Excitons. **Journal of Physical Chemistry Letters**, vol. 10, no. 24, p. 7774–7780, 19 Dec. 2019. https://doi.org/10.1021/acs.jpclett.9b03413.

NIU, B.; WU, H.; YIN, J.; WANG, B.; WU, G.; KONG, X.; YAN, B.; YAO, J.; LI, C. Z.; CHEN, H. Mitigating the Lead Leakage of High-Performance Perovskite Solar Cells via in Situ Polymerized Networks. **ACS Energy Letters**, vol. 6, no. 10, p. 3443–3449, 8 Oct. 2021. https://doi.org/10.1021/acsenergylett.1c01487.

RAMAN, R. K.; GURUSAMY THANGAVELU, S. A.; VENKATARAJ, S.; KRISHNAMOORTHY, A. Materials, methods and strategies for encapsulation of perovskite solar cells: From past to present. **Renewable and Sustainable Energy Reviews**, vol. 151, 1 Nov. 2021. https://doi.org/10.1016/j.rser.2021.111608.

RAMAN, V.; JO, J.; KIM, H. K. ITO and graphene-covered Ag grids embedded in PET substrate by thermal roll imprinting for flexible organic solar cells. **Materials Science in Semiconductor Processing**, vol. 120, 1 Dec. 2020. https://doi.org/10.1016/j.mssp.2020.105277.

RÜHLE, S.; SHALOM, M.; ZABAN, A. Quantum-dot-sensitized solar cells. **ChemPhysChem**, vol. 11, no. 11, p. 2290–2304, 2010. https://doi.org/10.1002/cphc.201000069.

SALIBA, M.; CORREA-BAENA, J. P.; WOLFF, C. M.; STOLTERFOHT, M.; PHUNG, N.; ALBRECHT, S.; NEHER, D.; ABATE, A. How to Make over 20% Efficient Perovskite Solar Cells in Regular (n-i-p) and Inverted (p-i-n) Architectures. **Chemistry of Materials**, vol. 30, no. 13, p. 4193–4201, 10 Jul. 2018. https://doi.org/10.1021/acs.chemmater.8b00136.

SHENG, Y.; JI, W.; CHU, Y.; MING, Y.; MEI, A.; HU, Y.; RONG, Y.; HAN, H. Post-Treatment of Mesoporous Scaffolds for Enhanced Photovoltage of Triple-Mesoscopic Perovskite Solar Cells. **Solar RRL**, vol. 4, no. 9, 1 Sep. 2020. https://doi.org/10.1002/solr.202000185.

SHUKLA, S.; KOH, T. M.; PATIDAR, R.; LEW, J. H.; KAJAL, P.; MHAISALKAR, S. G.; MATHEWS, N. Suppressing the δ-Phase and Photoinstability through a Hypophosphorous Acid Additive in Carbon-Based Mixed-Cation Perovskite Solar Cells. **Journal of Physical Chemistry C**, vol. 125, no. 12, p. 6585–6592, 1 Apr. 2021. https://doi.org/10.1021/acs.jpcc.1c00490.

SUZUKI, A.; OKU, T. Electronic Structures of Eu-Doped FAPbI3 Perovskite Crystals Studied by First-Principles Calculation. 26 Apr. 2022. [*S. l.*]: MDPI AG, 26 Apr. 2022. p. 12. https://doi.org/10.3390/iocc_2022-12178.

TAVAKOLI, M. M.; PROCHOWICZ, D.; YADAV, P.; TAVAKOLI, R.; SALIBA, M. Zinc stannate nanorod as an electron transporting layer for highly efficient and hysteresis-less perovskite solar cells. **Engineered Science**, vol. 3, p. 48–53, 2018. https://doi.org/10.30919/es8d749.

TURREN-CRUZ, S. H.; HAGFELDT, A.; SALIBA, M. Methylammonium-free, high-performance, and stable perovskite solar cells on a planar architecture. **Science**, vol. 362, no. 6413, p. 449–453, 26 Oct. 2018. https://doi.org/10.1126/science.aat3583.

TZOGANAKIS, N.; FENG, B.; LOIZOS, M.; KRASSAS, M.; TSIKRITZIS, D.; ZHUANG, X.; KYMAKIS, E. Ultrathin PTAA interlayer in conjunction with azulene derivatives for the fabrication of inverted perovskite solar cells. **Journal of Materials Chemistry C**, vol. 9, no. 41, p. 14709–14719, 7 Nov. 2021. https://doi.org/10.1039/d1tc02726c.

UNGER, E. L.; HOKE, E. T.; BAILIE, C. D.; NGUYEN, W. H.; BOWRING, A. R.; HEUMÜLLER, T.; CHRISTOFORO, M. G.; MCGEHEE, M. D. Hysteresis and transient behavior in current-voltage measurements of hybrid-perovskite absorber solar cells. **Energy and Environmental Science**, vol. 7, no. 11, p. 3690–3698, 1 Nov. 2014. https://doi.org/10.1039/c4ee02465f.

VILLARREAL, C. C.; SANDOVAL, J. I.; RAMNANI, P.; TERSE-THAKOOR, T.; VI, D.; MULCHANDANI, A. Graphene compared to fluorine-doped tin oxide as transparent conductor in ZnO dye-sensitized solar cells. **Journal of Environmental Chemical Engineering**, vol. 10, no. 3, 1 Jun. 2022. https://doi.org/10.1016/j.jece.2022.107551.

WAGNER, L.; MUNDT, L. E.; MATHIAZHAGAN, G.; MUNDUS, M.; SCHUBERT, M. C.; MASTROIANNI, S.; WÜRFEL, U.; HINSCH, A.; GLUNZ, S. W. Distinguishing crystallization stages and their influence on quantum efficiency during perovskite solar cell formation in real-time. **Scientific Reports**, vol. 7, no. 1, 1 Dec. 2017. https://doi.org/10.1038/s41598-017-13855-6.

WANG, H.; CHAN, C. C. S.; CHU, M.; XIE, J.; ZHAO, S.; GUO, X.; MIAO, Q.; WONG, K. S.; YAN, K.; XU, J. Interlayer Cross-Linked 2D Perovskite Solar Cell with Uniform Phase Distribution and Increased Exciton Coupling. **Solar RRL**, vol. 4, no. 4, 1 Apr. 2020. https://doi.org/10.1002/solr.201900578.

WANG, J.; HASSAN, M. S.; ALHARTHI, M.; ARSHED, N.; HANIF, I.; SAEED, M. I. Inspecting non-linear behavior of aggregated and disaggregated renewable and non-renewable energy consumption on GDP per capita in Pakistan. **Energy Strategy Reviews**, vol. 39, 1 Jan. 2022. https://doi.org/10.1016/j.esr.2021.100772.

WANG, L.; YAN, Z.; QIU, J.; WU, J.; ZHEN, C.; TAI, K.; JIANG, X.; YANG, S. Interface regulation enables hysteresis free wide-bandgap perovskite solar cells with low V_{OC} deficit and high stability. **Nano Energy**, vol. 90, 1 Dec. 2021a. https://doi.org/10.1016/j.nanoen.2021.106537.

WANG, L.; YAN, Z.; QIU, J.; WU, J.; ZHEN, C.; TAI, K.; JIANG, X.; YANG, S. Interface regulation enables hysteresis free wide-bandgap perovskite solar cells with low V_{OC} deficit and high stability. **Nano Energy**, vol. 90, 1 Dec. 2021b. https://doi.org/10.1016/j.nanoen.2021.106537.

WU, J.; ZHANG, W.; WANG, Q.; LIU, S.; DU, J.; MEI, A.; RONG, Y.; HU, Y.; HAN, H. A favored crystal orientation for efficient printable mesoscopic perovskite solar cells. **Journal of Materials Chemistry A**, vol. 8, no. 22, p. 11148–11154, 14 Jun. 2020. https://doi.org/10.1039/d0ta04589f.

XIA, Y.; YAN, G.; LIN, J. Review on tailoring PEDOT:PSS layer for improved device stability of perovskite solar cells. **Nanomaterials**, vol. 11, no. 11, 1 Nov. 2021. https://doi.org/10.3390/nano11113119.

XIANG, T.; ZHANG, Y.; WU, H.; LI, J.; YANG, L.; WANG, K.; XIA, J.; DENG, Z.; XIAO, J.; LI, W.; KU, Z.; HUANG, F.; ZHONG, J.; PENG, Y.; CHENG, Y. B. Universal defects elimination for high performance thermally evaporated CsPbBr3 perovskite solar cells. **Solar Energy Materials and Solar Cells**, vol. 206, 1 Mar. 2020. https://doi.org/10.1016/j.solmat.2019.110317.

XIE, H.; WANG, Z.; CHEN, Z.; PEREYRA, C.; POLS, M.; GAŁKOWSKI, K.; ANAYA, M.; FU, S.; JIA, X.; TANG, P.; KUBICKI, D. J.; AGARWALLA, A.; KIM, H. S.; PROCHOWICZ, D.; BORRISÉ, X.; BONN, M.; BAO, C.; SUN, X.; ZAKEERUDDIN, S. M.; … LIRA-CANTU, M. Decoupling the effects of defects on efficiency and stability through phosphonates in stable halide perovskite solar cells. **Joule**, vol. 5, no. 5, p. 1246–1266, 19 May 2021. https://doi.org/10.1016/j.joule.2021.04.003.

YI, Z.; LADI, N. H.; SHAI, X.; LI, H.; SHEN, Y.; WANG, M. Will organic-inorganic hybrid halide lead perovskites be eliminated from optoelectronic applications?

Nanoscale Advances, vol. 1, no. 4, p. 1276–1289, 2019. https://doi.org/10.1039/c8na00416a.

ZHANG, G.; CHEN, X. K.; XIAO, J.; CHOW, P. C. Y.; REN, M.; KUPGAN, G.; JIAO, X.; CHAN, C. C. S.; DU, X.; XIA, R.; CHEN, Z.; YUAN, J.; ZHANG, Y.; ZHANG, S.; LIU, Y.; ZOU, Y.; YAN, H.; WONG, K. S.; COROPCEANU, V.; … CAO, Y. Delocalization of exciton and electron wavefunction in non-fullerene acceptor molecules enables efficient organic solar cells. **Nature Communications**, vol. 11, no. 1, 1 Dec. 2020. https://doi.org/10.1038/s41467-020-17867-1.

ZHANG, Y.; GRANCINI, G.; FENG, Y.; ASIRI, A. M.; NAZEERUDDIN, M. K. Optimization of Stable Quasi-Cubic FAxMA1-xPbI3 Perovskite Structure for Solar Cells with Efficiency beyond 20%. **ACS Energy Letters**, vol. 2, no. 4, p. 802–806, 14 Apr. 2017. https://doi.org/10.1021/acsenergylett.7b00112.

ZHAO, J.; ZHANG, Y.; ZHAO, X.; ZHANG, J.; WANG, H.; ZHU, Z.; LIU, Q. Band Alignment Strategy for Printable Triple Mesoscopic Perovskite Solar Cells with Enhanced Photovoltage. **ACS Applied Energy Materials**, vol. 2, no. 3, p. 2034–2042, 25 Mar. 2019. https://doi.org/10.1021/acsaem.8b02104.

ZHAO, Y.; ZHAO, K.; WAN, L.; TAN, Y.; WANG, Z. S. Black Phase of Inorganic Perovskite Stabilized with Carboxyimidazolium Iodide for Stable and Efficient Inverted Perovskite Solar Cells. **ACS Applied Materials and Interfaces**, vol. 14, no. 5, p. 6906–6915, 9 Feb. 2022. https://doi.org/10.1021/acsami.1c23637.

ZHU, L.; TU, Z.; YI, Y.; WEI, Z. Achieving Small Exciton Binding Energies in Small Molecule Acceptors for Organic Solar Cells: Effect of Molecular Packing. **Journal of Physical Chemistry Letters**, vol. 10, no. 17, p. 4888–4894, 5 Sep. 2019. https://doi.org/10.1021/acs.jpclett.9b02161.

ZIMMERMANN, I.; GRATIA, P.; MARTINEAU, D.; GRANCINI, G.; AUDINOT, J. N.; WIRTZ, T.; NAZEERUDDIN, M. K. Improved efficiency and reduced hysteresis in ultra-stable fully printable mesoscopic perovskite solar cells through incorporation of CuSCN into the perovskite layer. **Journal of Materials Chemistry A**, vol. 7, no. 14, p. 8073–8077, 2019. https://doi.org/10.1039/c9ta00669a.

ABDELHADY, A. L.; SAIDAMINOV, M. I.; MURALI, B.; ADINOLFI, V.; VOZNYY, O.; KATSIEV, K.; ALAROUSU, E.; COMIN, R.; DURSUN, I.; SINATRA, L.; SARGENT, E. H.; MOHAMMED, O. F.; BAKR, O. M. Heterovalent Dopant Incorporation for Bandgap and Type Engineering of Perovskite Crystals. **Journal of**

Physical Chemistry Letters, vol. 7, no. 2, p. 295–301, 21 Jan. 2016. https://doi.org/10.1021/acs.jpclett.5b02681.

AGRESTI, A.; PESCETELLI, S.; TAHERI, B.; DEL RIO CASTILLO, A. E.; CINÀ, L.; BONACCORSO, F.; DI CARLO, A. Graphene–Perovskite Solar Cells Exceed 18 % Efficiency: A Stability Study. **ChemSusChem**, vol. 9, no. 18, p. 2609–2619, 22 Sep. 2016. https://doi.org/10.1002/cssc.201600942.

ATTIA, S. K.; ELGENDY, A. T.; RIZK, S. A. Efficient green synthesis of antioxidant azacoumarin dye bearing spiro-pyrrolidine for enhancing electro-optical properties of perovskite solar cells. **Journal of Molecular Structure**, vol. 1184, p. 583–592, 15 May 2019. https://doi.org/10.1016/j.molstruc.2019.02.042.

AWOSUSI, A. A.; ADEBAYO, T. S.; ALTUNTAŞ, M.; AGYEKUM, E. B.; ZAWBAA, H. M.; KAMEL, S. The dynamic impact of biomass and natural resources on ecological footprint in BRICS economies: A quantile regression evidence. **Energy Reports**, vol. 8, p. 1979–1994, 1 Nov. 2022. https://doi.org/10.1016/j.egyr.2022.01.022.

BICCARI, F.; GABELLONI, F.; BURZI, E.; GURIOLI, M.; PESCETELLI, S.; AGRESTI, A.; DEL RIO CASTILLO, A. E.; ANSALDO, A.; KYMAKIS, E.; BONACCORSO, F.; DI CARLO, A.; VINATTIERI, A. Graphene-Based Electron Transport Layers in Perovskite Solar Cells: A Step-Up for an Efficient Carrier Collection. **Advanced Energy Materials**, vol. 7, no. 22, 22 Nov. 2017a. https://doi.org/10.1002/aenm.201701349.

BICCARI, F.; GABELLONI, F.; BURZI, E.; GURIOLI, M.; PESCETELLI, S.; AGRESTI, A.; DEL RIO CASTILLO, A. E.; ANSALDO, A.; KYMAKIS, E.; BONACCORSO, F.; DI CARLO, A.; VINATTIERI, A. Graphene-Based Electron Transport Layers in Perovskite Solar Cells: A Step-Up for an Efficient Carrier Collection. **Advanced Energy Materials**, vol. 7, no. 22, 22 Nov. 2017b. https://doi.org/10.1002/aenm.201701349.

BISQUERT, J.; JUAREZ-PEREZ, E. J. The Causes of Degradation of Perovskite Solar Cells. **Journal of Physical Chemistry Letters**, vol. 10, no. 19, p. 5889–5891, 3 Oct. 2019. https://doi.org/10.1021/acs.jpclett.9b00613.

BOLOTIN, K. I.; SIKES, K. J.; JIANG, Z.; KLIMA, M.; FUDENBERG, G.; HONE, J.; KIM, P.; STORMER, H. L. Ultrahigh electron mobility in suspended graphene. **Solid State Communications**, vol. 146, no. 9–10, p. 351–355, Jun. 2008. https://doi.org/10.1016/j.ssc.2008.02.024.

BUFFIERE, M.; ALI, K.; FARES, E.; SAMARA, A.; SHETTY, A. R.; AL HASSAN, O.; BELAIDI, A. Inkjet-Printed Compact TiO2 Electron Transport Layer for Perovskite Solar Cells. **Energy Technology**, vol. 8, no. 10, 1 Oct. 2020. https://doi.org/10.1002/ente.202000330.

CASE, C.; BEAUMONT, N.; KIRK, D. Industrial Insights into Perovskite Photovoltaics. **ACS Energy Letters**, vol. 4, no. 11, p. 2760–2762, 8 Nov. 2019. https://doi.org/10.1021/acsenergylett.9b02105.

CASTRO NETO, A. H.; GUINEA, F.; PERES, N. M. R.; NOVOSELOV, K. S.; GEIM, A. K. The electronic properties of graphene. **Reviews of Modern Physics**, vol. 81, no. 1, p. 109–162, 6 Jan. 2009. https://doi.org/10.1103/RevModPhys.81.109.

CHEN, B.; YANG, M.; PRIYA, S.; ZHU, K. Origin of JV Hysteresis in Perovskite Solar Cells. **Journal of Physical Chemistry Letters**, vol. 7, no. 5, p. 905–917, 3 Mar. 2016. https://doi.org/10.1021/acs.jpclett.6b00215.

CHUNG, J.; SHIN, S. S.; HWANG, K.; KIM, G.; KIM, K. W.; LEE, D. S.; KIM, W.; MA, B. S.; KIM, Y. K.; KIM, T. S.; SEO, J. Record-efficiency flexible perovskite solar cell and module enabled by a porous-planar structure as an electron transport layer. **Energy and Environmental Science**, vol. 13, no. 12, p. 4854–4861, 1 Dec. 2020. https://doi.org/10.1039/d0ee02164d.

CUI, Y.; CHEN, C.; LI, C.; CHEN, L.; BISTA, S. S.; LIU, X.; LI, Y.; AWNI, R. A.; SONG, Z.; YAN, Y. Correlating Hysteresis and Stability with Organic Cation Composition in the Two-Step Solution-Processed Perovskite Solar Cells. **ACS Applied Materials and Interfaces**, vol. 12, no. 9, p. 10588–10596, 4 Mar. 2020. https://doi.org/10.1021/acsami.9b23374.

DASH, D. P.; DASH, A. K.; SETHI, N. Designing hydro-energy led economic growth for pollution abatement: evidence from BRICS. **Environmental Science and Pollution Research**, vol. 29, no. 21, p. 31252–31269, 1 May 2022. https://doi.org/10.1007/s11356-021-17890-9.

DENG, K.; CHEN, Q.; LI, L. Modification Engineering in SnO2 Electron Transport Layer toward Perovskite Solar Cells: Efficiency and Stability. **Advanced Functional Materials**, vol. 30, no. 46, 1 Nov. 2020. https://doi.org/10.1002/adfm.202004209.

DENG, K.; CHEN, Q.; SHEN, Y.; LI, L. Improving UV stability of perovskite solar cells without sacrificing efficiency through light trapping regulated spectral modification. **Science Bulletin**, vol. 66, no. 23, p. 2362–2368, 15 Dec. 2021. https://doi.org/10.1016/j.scib.2021.06.022.

DENG, L.; YANG, H.; LIU, Z.; YANG, X.; HUANG, Z.; YU, H.; WANG, K.; LI, J. Effective Phase Control for High-Performance Red-Light-Emitting Quasi-2D Perovskite Solar Cells via MACl Additive. **ACS Applied Energy Materials**, vol. 4, no. 3, p. 2856–2863, 22 Mar. 2021. https://doi.org/10.1021/acsaem.1c00185.

DEWI, H. A.; WANG, H.; LI, J.; THWAY, M.; SRIDHARAN, R.; STANGL, R.; LIN, F.; ABERLE, A. G.; MATHEWS, N.; BRUNO, A.; MHAISALKAR, S. Highly Efficient Semitransparent Perovskite Solar Cells for Four Terminal Perovskite-Silicon Tandems. **ACS Applied Materials and Interfaces**, vol. 11, no. 37, p. 34178–34187, 18 Sep. 2019. https://doi.org/10.1021/acsami.9b13145.

EPERON, G. E.; HÖRANTNER, M. T.; SNAITH, H. J. Metal halide perovskite tandem and multiple-junction photovoltaics. **Nature Reviews Chemistry**, vol. 1, no. 12, Dec. 2017. https://doi.org/10.1038/s41570-017-0095.

FARINA, A.; ANCTIL, A. Material consumption and environmental impact of wind turbines in the USA and globally. **Resources, Conservation and Recycling**, vol. 176, 1 Jan. 2022. https://doi.org/10.1016/j.resconrec.2021.105938.

FENG, Y.; ZHANG, J.; DUAN, C.; ZHANG, X.; ZHANG, Y.; DAI, J. Improved inverted MAPbI3 perovskite solar cell with triphenylphosphine oxide passivation layer. **Optical Materials**, vol. 127, 1 May 2022. https://doi.org/10.1016/j.optmat.2022.112264.

FERGUSON, V.; SILVA, S. R. P.; ZHANG, W. Carbon Materials in Perovskite Solar Cells: Prospects and Future Challenges. **Energy and Environmental Materials**, vol. 2, no. 2, p. 107–118, 1 Jun. 2019. https://doi.org/10.1002/eem2.12035.

GAO, B.; YAO, H.; HOU, J.; YU, R.; HONG, L.; XU, Y.; HOU, J. Multi-component non-fullerene acceptors with tunable bandgap structures for efficient organic solar cells. **Journal of Materials Chemistry A**, vol. 6, no. 46, p. 23644–23649, 2018. https://doi.org/10.1039/C8TA09830A.

GAUTAM, B. R.; YOUNTS, R.; CARPENTER, J.; ADE, H.; GUNDOGDU, K. The Role of FRET in Non-Fullerene Organic Solar Cells: Implications for Molecular Design. **Journal of Physical Chemistry A**, vol. 122, no. 15, p. 3764–3771, 19 Apr. 2018. https://doi.org/10.1021/acs.jpca.7b12807.

GOURVENEC, S.; STURT, F.; REID, E.; TRIGOS, F. Global assessment of historical, current and forecast ocean energy infrastructure: Implications for marine space planning, sustainable design and end-of-engineered-life management. **Renewable and**

Sustainable Energy Reviews, vol. 154, 1 Feb. 2022. https://doi.org/10.1016/j.rser.2021.111794.

HAN, G. S.; SONG, Y. H.; JIN, Y. U.; LEE, J. W.; PARK, N. G.; KANG, B. K.; LEE, J. K.; CHO, I. S.; YOON, D. H.; JUNG, H. S. Reduced Graphene Oxide/Mesoporous TiO2 Nanocomposite Based Perovskite Solar Cells. **ACS Applied Materials and Interfaces**, vol. 7, no. 42, p. 23521–23526, 28 Oct. 2015. https://doi.org/10.1021/acsami.5b06171.

HE, Q.; WORKU, M.; LIU, H.; LOCHNER, E.; ROBB, A. J.; LTEIF, S.; VELLORE WINFRED, J. S. R.; HANSON, K.; SCHLENOFF, J. B.; KIM, B. J.; MA, B. Highly Efficient and Stable Perovskite Solar Cells Enabled by Low-Cost Industrial Organic Pigment Coating. **Angewandte Chemie - International Edition**, vol. 60, no. 5, p. 2485–2492, 1 Feb. 2021. https://doi.org/10.1002/anie.202012095.

HINRICHSEN, T. F.; CHAN, C. C. S.; MA, C.; PALEČEK, D.; GILLETT, A.; CHEN, S.; ZOU, X.; ZHANG, G.; YIP, H. L.; WONG, K. S.; FRIEND, R. H.; YAN, H.; RAO, A.; CHOW, P. C. Y. Long-lived and disorder-free charge transfer states enable endothermic charge separation in efficient non-fullerene organic solar cells. **Nature Communications**, vol. 11, no. 1, 1 Dec. 2020. https://doi.org/10.1038/s41467-020-19332-5.

HOU, M.; XU, Y.; TIAN, Y.; WU, Y.; ZHANG, D.; WANG, G.; LI, B.; REN, H.; LI, Y.; HUANG, Q.; DING, Y.; HOU, G.; ZHAO, Y.; ZHANG, X. Synergistic effect of MACl and DMF towards efficient perovskite solar cells. **Organic Electronics**, vol. 88, 1 Jan. 2021. https://doi.org/10.1016/j.orgel.2020.106005.

HU, Z.; LIN, Z.; SU, J.; ZHANG, J.; CHANG, J.; HAO, Y. A Review on Energy Band-Gap Engineering for Perovskite Photovoltaics. **Solar RRL**, vol. 3, no. 12, 1 Dec. 2019. https://doi.org/10.1002/solr.201900304.

HUANG, S.; LI, P.; WANG, J.; HUANG, J. C. C.; XUE, Q.; FU, N. Modification of SnO2 electron transport Layer: Brilliant strategies to make perovskite solar cells stronger. **Chemical Engineering Journal**, vol. 439, 1 Jul. 2022. https://doi.org/10.1016/j.cej.2022.135687.

HUANG, X.; ZHI, C.; LIN, Y.; BAO, H.; WU, G.; JIANG, P.; MAI, Y. W. Thermal conductivity of graphene-based polymer nanocomposites. **Materials Science and Engineering R: Reports**, vol. 142, 1 Oct. 2020. https://doi.org/10.1016/j.mser.2020.100577.

HUANG, Y.; LIU, T.; LIANG, C.; XIA, J.; LI, D.; ZHANG, H.; AMINI, A.; XING, G.; CHENG, C. Towards Simplifying the Device Structure of High-Performance Perovskite Solar Cells. **Advanced Functional Materials**, vol. 30, no. 28, 1 Jul. 2020. https://doi.org/10.1002/adfm.202000863.

ICHWANI, R.; KOECH, R.; OYEWOLE, O. K.; HUDA, A.; OYEWOLE, D. O.; CROMWELL, J.; MARTIN, J. L.; GRIMM, R. L.; SOBOYEJO, W. O. Interfacial fracture of hybrid organic–inorganic perovskite solar cells. **Extreme Mechanics Letters**, vol. 50, 1 Jan. 2022. https://doi.org/10.1016/j.eml.2021.101515.

InterEmpresas, "Desarrollo de tintas conductivas para la metalización por serigrafía de células solares de perovskita". Canales sectoriales, interempresas: Energías 2016. Available at: < https://www.interempresas.net/Energia/Articulos/162786-Desarrollo-tintas-conductivas-para-metalizacion-serigrafia-celulas-solares-perovskita.html >. Accessed on: August 1, 2022.

JENA, A. K.; NUMATA, Y.; IKEGAMI, M.; MIYASAKA, T. Role of spiro-OMeTAD in performance deterioration of perovskite solar cells at high temperature and reuse of the perovskite films to avoid Pb-waste. **Journal of Materials Chemistry A**, vol. 6, no. 5, p. 2219–2230, 2018. https://doi.org/10.1039/c7ta07674f.

JIANG, Q.; ZHANG, X.; YOU, J. SnO2: A Wonderful Electron Transport Layer for Perovskite Solar Cells. **Small**, vol. 14, no. 31, 2 Aug. 2018. https://doi.org/10.1002/smll.201801154.

JIN, H.; BU, Y.; LI, J.; LIU, J.; FEN, X.; DAI, L.; WANG, J.; LU, J.; WANG, S. Strong Graphene 3D Assemblies with High Elastic Recovery and Hardness. **Advanced Materials**, vol. 30, no. 36, 6 Sep. 2018. https://doi.org/10.1002/adma.201707424.

JIN, J. U.; LEE, D. H.; NAM, K. H.; YU, J.; KIM, Y. K.; GOH, M.; KIM, S. G.; LEE, H. S.; KU, B. C.; YOU, N. H. Methylpiperidine-functionalized graphene oxide for efficient curing acceleration and gas barrier of polymer nanocomposites. **Applied Surface Science**, vol. 464, p. 509–515, 15 Jan. 2019. https://doi.org/10.1016/j.apsusc.2018.09.086.

JOKAR, E.; HUANG, Z. Y.; NARRA, S.; WANG, C. Y.; KATTOOR, V.; CHUNG, C. C.; DIAU, E. W. G. Anomalous Charge-Extraction Behavior for Graphene-Oxide (GO) and Reduced Graphene-Oxide (rGO) Films as Efficient p-Contact Layers for High-Performance Perovskite Solar Cells. **Advanced Energy Materials**, vol. 8, no. 3, 25 Jan. 2018. https://doi.org/10.1002/aenm.201701640.

JUNG, K.; KIM, D. H.; KIM, J.; KO, S.; CHOI, J. W.; KIM, K. C.; LEE, S. G.; LEE, M. J. Influence of a UV-ozone treatment on amorphous SnO2 electron selective layers for highly efficient planar MAPbI3 perovskite solar cells. **Journal of Materials Science and Technology**, vol. 59, p. 195–202, 15 Dec. 2020. https://doi.org/10.1016/j.jmst.2020.04.054.

KAKAVELAKIS, G.; MAKSUDOV, T.; KONIOS, D.; PARADISANOS, I.; KIOSEOGLOU, G.; STRATAKIS, E.; KYMAKIS, E. Efficient and Highly Air Stable Planar Inverted Perovskite Solar Cells with Reduced Graphene Oxide Doped PCBM Electron Transporting Layer. **Advanced Energy Materials**, vol. 7, no. 7, 5 Apr. 2017. https://doi.org/10.1002/aenm.201602120.

KE, W.; FANG, G.; WANG, J.; QIN, P.; TAO, H.; LEI, H.; LIU, Q.; DAI, X.; ZHAO, X. Perovskite solar cell with an efficient TiO2 compact film. **ACS Applied Materials and Interfaces**, vol. 6, no. 18, p. 15959–15965, 24 Sep. 2014. https://doi.org/10.1021/am503728d.

KESKIN, A. v.; GENÇTEN, M.; BOZAR, S.; ARVAS, M. B.; GÜNEŞ, S.; SAHIN, Y. Preparation of anatase form of TiO2 thin film at room temperature by electrochemical method as an alternative electron transport layer for inverted type organic solar cells. **Thin Solid Films**, vol. 706, 31 Jul. 2020. https://doi.org/10.1016/j.tsf.2020.138093.

KHAN, J.; UR RAHMAN, N.; KHAN, W. U.; HAYAT, A.; YANG, Z.; AHMED, G.; AKHTAR, M. N.; TONG, S.; CHI, Z.; WU, M. Multi-dimensional anatase TiO2 materials: Synthesis and their application as efficient charge transporter in perovskite solar cells. **Solar Energy**, vol. 184, p. 323–330, 15 May 2019. https://doi.org/10.1016/j.solener.2019.04.020.

KIM, B. J.; KIM, M. CHEOL; LEE, D. G.; LEE, G.; BANG, G. J.; JEON, J. B.; CHOI, M.; JUNG, H. S. Interface Design of Hybrid Electron Extraction Layer for Relieving Hysteresis and Retarding Charge Recombination in Perovskite Solar Cells. **Advanced Materials Interfaces**, vol. 5, no. 23, 7 Dec. 2018. https://doi.org/10.1002/admi.201800993.

KUMAR, S.; AFTAB, A.; AHMAD, M. I. Compact Titania Films by Spray Pyrolysis for Application as ETL in Perovskite Solar Cells. **Journal of Electronic Materials**, vol. 49, no. 12, p. 7159–7167, 1 Dec. 2020. https://doi.org/10.1007/s11664-020-08464-5.

KUSUMA, J.; BALAKRISHNA, R. G.; PATIL, S.; JYOTHI, M. S.; CHANDAN, H. R.; SHWETHARANI, R. Exploration of graphene oxide nanoribbons as excellent electron conducting network for third generation solar cells. **Solar Energy Materials and Solar Cells**, vol. 183, p. 211–219, 15 Aug. 2018. https://doi.org/10.1016/j.solmat.2018.01.039.

LEE, J.; KIM, J.; KIM, C. S.; JO, S. Compact SnO2 /Mesoporous TiO2 Bilayer Electron Transport Layer for Perovskite Solar Cells Fabricated at Low Process Temperature. **Nanomaterials**, vol. 12, no. 4, 1 Feb. 2022. https://doi.org/10.3390/nano12040718.

LEE, Y. H.; PARK, S.; WON, Y.; MUN, J.; HA, J. H.; LEE, J. H.; LEE, S. H.; PARK, J.; YEOM, J.; RHO, J.; KO, H.; OH, J. H. Flexible high-performance graphene hybrid photodetectors functionalized with gold nanostars and perovskites. **NPG Asia Materials**, vol. 12, no. 1, 1 Dec. 2020. https://doi.org/10.1038/s41427-020-00260-1.

LICHTENEGGER, M. F.; DREWNIOK, J.; BORNSCHLEGL, A.; LAMPE, C.; SINGLDINGER, A.; HENKE, N. A.; URBAN, A. S. Electron-Hole Binding Governs Carrier Transport in Halide Perovskite Nanocrystal Thin Films. **ACS Nano**, vol. 16, no. 4, p. 6317–6324, 26 Apr. 2022. https://doi.org/10.1021/acsnano.2c00369.

LIU, G.; TIAN, T.; YANG, J.; ZHONG, J. X.; GULAMOVA, D.; WU, W. Q. Carbon Electrode Endows High-Efficiency Perovskite Photovoltaics Affordable, Fully Printable, and Durable. **Solar RRL**, 1 Jul. 2022. https://doi.org/10.1002/solr.202200258.

LIU, L.; QING, M.; WANG, Y.; CHEN, S. Defects in Graphene: Generation, Healing, and Their Effects on the Properties of Graphene: A Review. **Journal of Materials Science and Technology**, vol. 31, no. 6, p. 599–606, 1 Jun. 2015. https://doi.org/10.1016/j.jmst.2014.11.019.

LU, C.; ZHANG, W.; JIANG, Z.; ZHANG, Y.; NI, C. Graphene quantum dots doping SnO2 for improving carrier transport of perovskite solar cells. **Ceramics International**, vol. 47, no. 21, p. 29712–29721, 1 Nov. 2021. https://doi.org/10.1016/j.ceramint.2021.07.143.

LUCEÑO-SÁNCHEZ, J. A.; DÍEZ-PASCUAL, A. M.; CAPILLA, R. P. Materials for photovoltaics: State of art and recent developments. **International Journal of Molecular Sciences**, vol. 20, no. 4, 2 Feb. 2019. https://doi.org/10.3390/ijms20040976.

MAHAPATRA, A.; KUMAR, S.; KUMAR, P.; PRADHAN, B. Recent progress in perovskite solar cells: challenges from efficiency to stability. **Materials Today Chemistry**, vol. 23, 1 Mar. 2022. https://doi.org/10.1016/j.mtchem.2021.100686.

MARTÍN-GARCÍA, B.; BI, Y.; PRATO, M.; SPIRITO, D.; KRAHNE, R.; KONSTANTATOS, G.; MOREELS, I. Reduction of moisture sensitivity of PbS quantum dot solar cells by incorporation of reduced graphene oxide. **Solar Energy Materials and Solar Cells**, vol. 183, p. 1–7, 15 Aug. 2018. https://doi.org/10.1016/j.solmat.2018.04.005.

MAYIMELE, M. A.; FRU, J. N.; NYARIGE, J. S.; DIALE, M. Sequential physical vapor deposited methylammonium lead tri-iodide perovskites on FTO and ITO modified zinc oxide nanorods for perovskite solar cells. **Physica B: Condensed Matter**, vol. 625, 15 Jan. 2022. https://doi.org/10.1016/j.physb.2021.413462.

MENG, X.; HO, C. H. Y.; XIAO, S.; BAI, Y.; ZHANG, T.; HU, C.; LIN, H.; YANG, Y.; SO, S. K.; YANG, S. Molecular design enabled reduction of interface trap density affords highly efficient and stable perovskite solar cells with over 83% fill factor. **Nano Energy**, vol. 52, p. 300–306, 1 Oct. 2018. https://doi.org/10.1016/j.nanoen.2018.07.063.

MOHAMAD NOH, M. F.; TEH, C. H.; DAIK, R.; LIM, E. L.; YAP, C. C.; IBRAHIM, M. A.; AHMAD LUDIN, N.; MOHD YUSOFF, A. R. bin; JANG, J.; MAT TERIDI, M. A. The architecture of the electron transport layer for a perovskite solar cell. **Journal of Materials Chemistry C**, vol. 6, no. 4, p. 682–712, 2018. https://doi.org/10.1039/c7tc04649a.

NAGARAJ, G.; MOHAMMED, M. K. A.; SHEKARGOFTAR, M.; SASIKUMAR, P.; SAKTHIVEL, P.; RAVI, G.; DEHGHANIPOUR, M.; AKIN, S.; SHALAN, A. E. High-performance perovskite solar cells using the graphene quantum dot–modified SnO2/ZnO photoelectrode. **Materials Today Energy**, vol. 22, 1 Dec. 2021. https://doi.org/10.1016/j.mtener.2021.100853.

Naghshin, Vahid. “Use Adjusted Box plot for Skewed Distribution”. Artificial Intelligence in Plain English, 2020. Available at: < https://ai.plainenglish.io/use-adjusted-box plot-for-skewed-distribution-d1bc0ec25f6d >. Accessed on: August 9, 2022.

NAN, G.; ZHANG, X.; LU, G. Self-Healing of Photocurrent Degradation in Perovskite Solar Cells: The Role of Defect-Trapped Excitons. **Journal of Physical Chemistry Letters**, vol. 10, no. 24, p. 7774–7780, 19 Dec. 2019. https://doi.org/10.1021/acs.jpclett.9b03413.

National Renewable Energy Laboratory (NREL), “Best Research-Cell Efficiencies: Emerging Photovoltaics”. Photovoltaic Research: Best Research-Cell Efficiency Chart, 2022. Available at: < https://www.nrel.gov/pv/cell-efficiency.html >. Accessed on: August 1, 2022.

NIU, B.; WU, H.; YIN, J.; WANG, B.; WU, G.; KONG, X.; YAN, B.; YAO, J.; LI, C. Z.; CHEN, H. Mitigating the Lead Leakage of High-Performance Perovskite Solar Cells via in Situ Polymerized Networks. **ACS Energy Letters**, vol. 6, no. 10, p. 3443–3449, 8 Oct. 2021. https://doi.org/10.1021/acsenergylett.1c01487.

OOSTINGA, J. B.; HEERSCHE, H. B.; LIU, X.; MORPURGO, A. F.; VANDERSYPEN, L. M. K. Gate-induced insulating state in bilayer graphene devices. **Nature Materials**, vol. 7, no. 2, p. 151–157, 2008. https://doi.org/10.1038/nmat2082.

PANG, S.; ZHANG, C.; ZHANG, H.; DONG, H.; CHEN, D.; ZHU, W.; XI, H.; CHANG, J.; LIN, Z.; ZHANG, J.; HAO, Y. Boosting performance of perovskite solar cells with Graphene quantum dots decorated SnO2 electron transport layers. **Applied Surface Science**, vol. 507, 30 Mar. 2020. https://doi.org/10.1016/j.apsusc.2019.145099.

PROCHOWICZ, D.; TAVAKOLI, M. M.; WOLSKA-PIETKIEWICZ, M.; JĘDRZEJEWSKA, M.; TRIVEDI, S.; KUMAR, M.; ZAKEERUDDIN, S. M.; LEWIŃSKI, J.; GRAETZEL, M.; YADAV, P. Suppressing recombination in perovskite solar cells via surface engineering of TiO2 ETL. **Solar Energy**, vol. 197, p. 50–57, 1 Feb. 2020. https://doi.org/10.1016/j.solener.2019.12.070.

RAHMAN, A.; FARROK, O.; HAQUE, M. M. Environmental impact of renewable energy source based electrical power plants: Solar, wind, hydroelectric, biomass, geothermal, tidal, ocean, and osmotic. **Renewable and Sustainable Energy Reviews**, vol. 161, 1 Jun. 2022. https://doi.org/10.1016/j.rser.2022.112279.

RAMAN, R. K.; GURUSAMY THANGAVELU, S. A.; VENKATARAJ, S.; KRISHNAMOORTHY, A. Materials, methods and strategies for encapsulation of perovskite solar cells: From past to present. **Renewable and Sustainable Energy Reviews**, vol. 151, 1 Nov. 2021. https://doi.org/10.1016/j.rser.2021.111608.

RAMAN, V.; JO, J.; KIM, H. K. ITO and graphene-covered Ag grids embedded in PET substrate by thermal roll imprinting for flexible organic solar cells. **Materials Science in Semiconductor Processing**, vol. 120, 1 Dec. 2020. https://doi.org/10.1016/j.mssp.2020.105277.

RONG, Y.; LIU, L.; MEI, A.; LI, X.; HAN, H. Beyond efficiency: The challenge of stability in mesoscopic perovskite solar cells. **Advanced Energy Materials**, vol. 5, no. 20, 1 Oct. 2015. https://doi.org/10.1002/aenm.201501066.

RÜHLE, S.; SHALOM, M.; ZABAN, A. Quantum-dot-sensitized solar cells. **ChemPhysChem**, vol. 11, no. 11, p. 2290–2304, 2010. https://doi.org/10.1002/cphc.201000069.

RUIZ, A.; DEZANNEAU, G.; ARBIOL, J.; CORNET, A.; MORANTE, J. R. **Study of the influence of Nb content and sintering temperature on TiO 2 sensing films**. [*S. l.*: *s. n.*], 2003.

SALIBA, M.; CORREA-BAENA, J. P.; WOLFF, C. M.; STOLTERFOHT, M.; PHUNG, N.; ALBRECHT, S.; NEHER, D.; ABATE, A. How to Make over 20% Efficient Perovskite Solar Cells in Regular (n-i-p) and Inverted (p-i-n) Architectures. **Chemistry of Materials**, vol. 30, no. 13, p. 4193–4201, 10 Jul. 2018. https://doi.org/10.1021/acs.chemmater.8b00136.

SHAHIDUZZAMAN, M.; KUWAHARA, D.; NAKANO, M.; KARAKAWA, M.; TAKAHASHI, K.; NUNZI, J. M.; TAIMA, T. Low-temperature processed TiOx electron transport layer for efficient planar perovskite solar cells. **Nanomaterials**, vol. 10, no. 9, p. 1–12, 1 Sep. 2020. https://doi.org/10.3390/nano10091676.

SHENG, Y.; JI, W.; CHU, Y.; MING, Y.; MEI, A.; HU, Y.; RONG, Y.; HAN, H. Post-Treatment of Mesoporous Scaffolds for Enhanced Photovoltage of Triple-Mesoscopic Perovskite Solar Cells. **Solar RRL**, vol. 4, no. 9, 1 Sep. 2020. https://doi.org/10.1002/solr.202000185.

SHUKLA, S.; KOH, T. M.; PATIDAR, R.; LEW, J. H.; KAJAL, P.; MHAISALKAR, S. G.; MATHEWS, N. Suppressing the δ-Phase and Photoinstability through a Hypophosphorous Acid Additive in Carbon-Based Mixed-Cation Perovskite Solar Cells. **Journal of Physical Chemistry C**, vol. 125, no. 12, p. 6585–6592, 1 Apr. 2021. https://doi.org/10.1021/acs.jpcc.1c00490.

SIDHIK, S.; PANIKAR, S. S.; PÉREZ, C. R.; LUKE, T. L.; CARRILES, R.; CARRERA, S. C.; DE LA ROSA, E. Interfacial Engineering of TiO2 by Graphene Nanoplatelets for High-Efficiency Hysteresis-free Perovskite Solar Cells. **ACS Sustainable Chemistry and Engineering**, vol. 6, no. 11, p. 15391–15401, 5 Nov. 2018. https://doi.org/10.1021/acssuschemeng.8b03826.

SOLANKI, A.; YADAV, P.; TURREN-CRUZ, S. H.; LIM, S. S.; SALIBA, M.; SUM, T. C. Cation influence on carrier dynamics in perovskite solar cells. **Nano Energy**, vol. 58, p. 604–611, 1 Apr. 2019. https://doi.org/10.1016/j.nanoen.2019.01.060.

SONG, J.; XU, X.; WU, J.; LAN, Z. Low-temperature solution-processing high quality Nb-doped SnO2 nanocrystals-based electron transport layers for efficient planar perovskite solar cells. **Functional Materials Letters**, vol. 12, no. 1, 1 Feb. 2019. https://doi.org/10.1142/S1793604718500911.

SUZUKI, A.; OKU, T. Electronic Structures of Eu-Doped FAPbI3 Perovskite Crystals Studied by First-Principles Calculation. 26 Apr. 2022. [*S. l.*]: MDPI AG, 26 Apr. 2022. p. 12. https://doi.org/10.3390/iocc_2022-12178.

TAHERI-LEDARI, R.; VALADI, K.; MALEKI, A. High-performance HTL-free perovskite solar cell: An efficient composition of ZnO NRs, RGO, and CuInS2 QDs, as electron-transporting layer matrix. **Progress in Photovoltaics: Research and Applications**, vol. 28, no. 9, p. 956–970, 1 Sep. 2020. https://doi.org/10.1002/pip.3306.

TAVAKOLI, M. M.; PROCHOWICZ, D.; YADAV, P.; TAVAKOLI, R.; SALIBA, M. Zinc stannate nanorod as an electron transporting layer for highly efficient and hysteresis-less perovskite solar cells. **Engineered Science**, vol. 3, p. 48–53, 2018. https://doi.org/10.30919/es8d749.

TAVAKOLI, M. M.; YADAV, P.; TAVAKOLI, R.; KONG, J. Surface Engineering of TiO2 ETL for Highly Efficient and Hysteresis-Less Planar Perovskite Solar Cell (21.4%) with Enhanced Open-Circuit Voltage and Stability. **Advanced Energy Materials**, vol. 8, no. 23, 16 Aug. 2018. https://doi.org/10.1002/aenm.201800794.

TIENNE, L. G. P.; CANDIDO, L. da S.; DA CRUZ, B. de S. M.; GONDIM, F. F.; RIBEIRO, M. P.; SIMÃO, R. A.; MARQUES, M. de F. V.; MONTEIRO, S. N. Reduced graphene oxide synthesized by a new modified Hummer's method for enhancing thermal and crystallinity properties of Poly(vinylidene fluoride). **Journal of Materials Research and Technology**, vol. 18, p. 4871–4893, May 2022. https://doi.org/10.1016/j.jmrt.2022.04.092.

TUMEN-ULZII, G.; MATSUSHIMA, T.; KLOTZ, D.; LEYDEN, M. R.; WANG, P.; QIN, C.; LEE, J. W.; LEE, S. J.; YANG, Y.; ADACHI, C. Hysteresis-less and stable perovskite solar cells with a self-assembled monolayer. **Communications Materials**, vol. 1, no. 1, 1 Dec. 2020. https://doi.org/10.1038/s43246-020-0028-z.

TURREN-CRUZ, S. H.; HAGFELDT, A.; SALIBA, M. Methylammonium-free, high-performance, and stable perovskite solar cells on a planar architecture. **Science**, vol. 362, no. 6413, p. 449–453, 26 Oct. 2018. https://doi.org/10.1126/science.aat3583.

TZOGANAKIS, N.; FENG, B.; LOIZOS, M.; KRASSAS, M.; TSIKRITZIS, D.; ZHUANG, X.; KYMAKIS, E. Ultrathin PTAA interlayer in conjunction with azulene derivatives for the fabrication of inverted perovskite solar cells. **Journal of Materials Chemistry C**, vol. 9, no. 41, p. 14709–14719, 7 Nov. 2021. https://doi.org/10.1039/d1tc02726c.

UNGER, E. L.; HOKE, E. T.; BAILIE, C. D.; NGUYEN, W. H.; BOWRING, A. R.; HEUMÜLLER, T.; CHRISTOFORO, M. G.; MCGEHEE, M. D. Hysteresis and transient behavior in current-voltage measurements of hybrid-perovskite absorber solar cells. **Energy and Environmental Science**, vol. 7, no. 11, p. 3690–3698, 1 Nov. 2014. https://doi.org/10.1039/c4ee02465f.

VILLARREAL, C. C.; SANDOVAL, J. I.; RAMNANI, P.; TERSE-THAKOOR, T.; VI, D.; MULCHANDANI, A. Graphene compared to fluorine-doped tin oxide as transparent conductor in ZnO dye-sensitized solar cells. **Journal of Environmental Chemical Engineering**, vol. 10, no. 3, 1 Jun. 2022. https://doi.org/10.1016/j.jece.2022.107551.

WANG, H.; CHAN, C. C. S.; CHU, M.; XIE, J.; ZHAO, S.; GUO, X.; MIAO, Q.; WONG, K. S.; YAN, K.; XU, J. Interlayer Cross-Linked 2D Perovskite Solar Cell with Uniform Phase Distribution and Increased Exciton Coupling. **Solar RRL**, vol. 4, no. 4, 1 Apr. 2020. https://doi.org/10.1002/solr.201900578.

WANG, J.; HASSAN, M. S.; ALHARTHI, M.; ARSHED, N.; HANIF, I.; SAEED, M. I. Inspecting non-linear behavior of aggregated and disaggregated renewable and non-renewable energy consumption on GDP per capita in Pakistan. **Energy Strategy Reviews**, vol. 39, 1 Jan. 2022. https://doi.org/10.1016/j.esr.2021.100772.

WANG, L.; YAN, Z.; QIU, J.; WU, J.; ZHEN, C.; TAI, K.; JIANG, X.; YANG, S. Interface regulation enables hysteresis free wide-bandgap perovskite solar cells with low V_{OC} deficit and high stability. **Nano Energy**, vol. 90, 1 Dec. 2021a. https://doi.org/10.1016/j.nanoen.2021.106537.

WANG, L.; YAN, Z.; QIU, J.; WU, J.; ZHEN, C.; TAI, K.; JIANG, X.; YANG, S. Interface regulation enables hysteresis free wide-bandgap perovskite solar cells with low V_{OC} deficit and high stability. **Nano Energy**, vol. 90, 1 Dec. 2021b. https://doi.org/10.1016/j.nanoen.2021.106537.

WANG, S. P.; GUO, J. G.; ZHOU, L. J. Influence of Stone-Wales defects on elastic properties of graphene nanofilms. **Physica E: Low-Dimensional Systems and Nanostructures**, vol. 48, p. 29–35, 2013. https://doi.org/10.1016/j.physe.2012.11.002.

WANG, Y.; WAN, J.; DING, J.; HU, J.; WANG, D. A Rutile TiO 2 Electron Transport Layer for the Enhancement of Charge Collection for Efficient Perovskite Solar Cells. **Angewandte Chemie**, vol. 131, no. 28, p. 9514–9518, 8 Jul. 2019. https://doi.org/10.1002/ange.201902984.

WU, J.; ZHANG, W.; WANG, Q.; LIU, S.; DU, J.; MEI, A.; RONG, Y.; HU, Y.; HAN, H. A favored crystal orientation for efficient printable mesoscopic perovskite solar cells. **Journal of Materials Chemistry A**, vol. 8, no. 22, p. 11148–11154, 14 Jun. 2020. https://doi.org/10.1039/d0ta04589f.

WU, W. Q.; LIAO, J. F.; ZHONG, J. X.; XU, Y. F.; WANG, L.; HUANG, J. Suppressing Interfacial Charge Recombination in Electron-Transport-Layer-Free Perovskite Solar Cells to Give an Efficiency Exceeding 21 %. **Angewandte Chemie - International Edition**, vol. 59, no. 47, p. 20980–20987, 16 Nov. 2020. https://doi.org/10.1002/anie.202005680.

XIA, Y.; YAN, G.; LIN, J. Review on tailoring pedot:Pss layer for improved device stability of perovskite solar cells. **Nanomaterials**, vol. 11, no. 11, 1 Nov. 2021. https://doi.org/10.3390/nano11113119.

XIANG, T.; ZHANG, Y.; WU, H.; LI, J.; YANG, L.; WANG, K.; XIA, J.; DENG, Z.; XIAO, J.; LI, W.; KU, Z.; HUANG, F.; ZHONG, J.; PENG, Y.; CHENG, Y. B. Universal defects elimination for high performance thermally evaporated CsPbBr3 perovskite solar cells. **Solar Energy Materials and Solar Cells**, vol. 206, 1 Mar. 2020. https://doi.org/10.1016/j.solmat.2019.110317.

XIE, H.; WANG, Z.; CHEN, Z.; PEREYRA, C.; POLS, M.; GAŁKOWSKI, K.; ANAYA, M.; FU, S.; JIA, X.; TANG, P.; KUBICKI, D. J.; AGARWALLA, A.; KIM, H. S.; PROCHOWICZ, D.; BORRISÉ, X.; BONN, M.; BAO, C.; SUN, X.; ZAKEERUDDIN, S. M.; … LIRA-CANTU, M. Decoupling the effects of defects on efficiency and stability through phosphonates in stable halide perovskite solar cells. **Joule**, vol. 5, no. 5, p. 1246–1266, 19 May 2021. https://doi.org/10.1016/j.joule.2021.04.003.

XIONG, L.; GUO, Y.; WEN, J.; LIU, H.; YANG, G.; QIN, P.; FANG, G. Review on the Application of SnO2 in Perovskite Solar Cells. **Advanced Functional Materials**, vol. 28, no. 35, 29 Aug. 2018. https://doi.org/10.1002/adfm.201802757.

YANG, G.; CHEN, C.; YAO, F.; CHEN, Z.; ZHANG, Q.; ZHENG, X.; MA, J.; LEI, H.; QIN, P.; XIONG, L.; KE, W.; LI, G.; YAN, Y.; FANG, G. Effective Carrier-Concentration Tuning of SnO2 Quantum Dot Electron-Selective Layers for High-Performance Planar Perovskite Solar Cells. **Advanced Materials**, vol. 30, no. 14, 5 Apr. 2018. https://doi.org/10.1002/adma.201706023.

YANG, Z.; CHEN, W.; MEI, A.; LI, Q.; LIU, Y. Flexible MAPbI3 perovskite solar cells with the high efficiency of 16.11% by low-temperature synthesis of compact anatase TiO2 film. **Journal of Alloys and Compounds**, vol. 854, 15 Feb. 2021. https://doi.org/10.1016/j.jallcom.2020.155488.

YI, H.; WANG, D.; MAHMUD, M. A.; HAQUE, F.; UPAMA, M. B.; XU, C.; DUAN, L.; UDDIN, A. Bilayer SnO2 as Electron Transport Layer for Highly Efficient Perovskite Solar Cells. **ACS Applied Energy Materials**, vol. 1, no. 11, p. 6027–6039, 26 Nov. 2018. https://doi.org/10.1021/acsaem.8b01076.

YI, Z.; LADI, N. H.; SHAI, X.; LI, H.; SHEN, Y.; WANG, M. Will organic-inorganic hybrid halide lead perovskites be eliminated from optoelectronic applications? **Nanoscale Advances**, vol. 1, no. 4, p. 1276–1289, 2019. https://doi.org/10.1039/c8na00416a.

YILMAZ, F. Development and modeling of the geothermal energy based multigeneration plant for beneficial outputs: Thermo-economic and environmental analysis approach. **Renewable Energy**, vol. 189, p. 1074–1085, 1 Apr. 2022. https://doi.org/10.1016/j.renene.2022.03.042.

YOU, Y.; TIAN, W.; MIN, L.; CAO, F.; DENG, K.; LI, L. TiO2/WO3 Bilayer as Electron Transport Layer for Efficient Planar Perovskite Solar Cell with Efficiency Exceeding 20%. **Advanced Materials Interfaces**, vol. 7, no. 1, 1 Jan. 2020. https://doi.org/10.1002/admi.201901406.

ZENKER, B.; IHLE, D.; BRONOLD, F. X.; FEHSKE, H. Electron-hole pair condensation at the semimetal-semiconductor transition: A BCS-BEC crossover scenario. **Physical Review B - Condensed Matter and Materials Physics**, vol. 85, no. 12, 9 Mar. 2012. https://doi.org/10.1103/PhysRevB.85.121102.

ZHANG, G.; CHEN, X. K.; XIAO, J.; CHOW, P. C. Y.; REN, M.; KUPGAN, G.; JIAO, X.; CHAN, C. C. S.; DU, X.; XIA, R.; CHEN, Z.; YUAN, J.; ZHANG, Y.; ZHANG, S.; LIU, Y.; ZOU, Y.; YAN, H.; WONG, K. S.; COROPCEANU, V.; … CAO, Y. Delocalization of exciton and electron wavefunction in non-fullerene acceptor molecules enables efficient organic solar cells. **Nature Communications**, vol. 11, no. 1, 1 Dec. 2020. https://doi.org/10.1038/s41467-020-17867-1.

ZHANG, M.; HU, W.; SHANG, Y.; ZHOU, W.; ZHANG, W.; YANG, S. Surface Passivation of Perovskite Film by Sodium Toluenesulfonate for Highly Efficient Solar Cells. **Solar RRL**, vol. 4, no. 6, 1 Jun. 2020a. https://doi.org/10.1002/solr.202000113.

ZHANG, M.; HU, W.; SHANG, Y.; ZHOU, W.; ZHANG, W.; YANG, S. Surface Passivation of Perovskite Film by Sodium Toluenesulfonate for Highly Efficient Solar Cells. **Solar RRL**, vol. 4, no. 6, 1 Jun. 2020b. https://doi.org/10.1002/solr.202000113.

ZHANG, Y.; GRANCINI, G.; FENG, Y.; ASIRI, A. M.; NAZEERUDDIN, M. K. Optimization of Stable Quasi-Cubic FAxMA1-xPbI3 Perovskite Structure for Solar Cells with Efficiency beyond 20%. **ACS Energy Letters**, vol. 2, no. 4, p. 802–806, 14 Apr. 2017. https://doi.org/10.1021/acsenergylett.7b00112.

ZHAO, J.; ZHANG, Y.; ZHAO, X.; ZHANG, J.; WANG, H.; ZHU, Z.; LIU, Q. Band Alignment Strategy for Printable Triple Mesoscopic Perovskite Solar Cells with Enhanced Photovoltage. **ACS Applied Energy Materials**, vol. 2, no. 3, p. 2034–2042, 25 Mar. 2019. https://doi.org/10.1021/acsaem.8b02104.

ZHAO, X.; TAO, L.; LI, H.; HUANG, W.; SUN, P.; LIU, J.; LIU, S.; SUN, Q.; CUI, Z.; SUN, L.; SHEN, Y.; YANG, Y.; WANG, M. Efficient Planar Perovskite Solar Cells with Improved Fill Factor via Interface Engineering with Graphene. **Nano Letters**, vol. 18, no. 4, p. 2442–2449, 11 Apr. 2018. https://doi.org/10.1021/acs.nanolett.8b00025.

ZHAO, Y.; ZHAO, K.; WAN, L.; TAN, Y.; WANG, Z. S. Black Phase of Inorganic Perovskite Stabilized with Carboxyimidazolium Iodide for Stable and Efficient Inverted Perovskite Solar Cells. **ACS Applied Materials and Interfaces**, vol. 14, no. 5, p. 6906–6915, 9 Feb. 2022. https://doi.org/10.1021/acsami.1c23637.

ZHU, L.; TU, Z.; YI, Y.; WEI, Z. Achieving Small Exciton Binding Energies in Small Molecule Acceptors for Organic Solar Cells: Effect of Molecular Packing. **Journal of Physical Chemistry Letters**, vol. 10, no. 17, p. 4888–4894, 5 Sep. 2019. https://doi.org/10.1021/acs.jpclett.9b02161.

ZHU, P.; GU, S.; LUO, X.; GAO, Y.; LI, S.; ZHU, J.; TAN, H. Simultaneous Contact and Grain-Boundary Passivation in Planar Perovskite Solar Cells Using SnO2-KCl Composite Electron Transport Layer. **Advanced Energy Materials**, vol. 10, no. 3, 1 Jan. 2020. https://doi.org/10.1002/aenm.201903083.

ZIMMERMANN, I.; GRATIA, P.; MARTINEAU, D.; GRANCINI, G.; AUDINOT, J. N.; WIRTZ, T.; NAZEERUDDIN, M. K. Improved efficiency and reduced hysteresis in ultra-stable fully printable mesoscopic perovskite solar cells through incorporation of CuSCN into the perovskite layer. **Journal of Materials Chemistry A**, vol. 7, no. 14, p. 8073–8077, 2019. https://doi.org/10.1039/c9ta00669a.